LBL-14677 c.2

Lawrence Berkeley Laboratory
UNIVERSITY OF CALIFORNIA

RECEIVED
LAWRENCE
BERKELEY LABORATORY
AUG 18 1982
LIBRARY AND
DOCUMENTS SECTION

A (p,2p) STUDY OF HIGH MOMENTUM COMPONENTS AT 2.1 GeV

Robert Neil Treuhaft
(Ph.D. thesis)

July 1982

TWO-WEEK LOAN COPY
This is a Library Circulating Copy which may be borrowed for two weeks. For a personal retention copy, call Tech. Info. Division, Ext. 6782.

NUCLEAR SCIENCE DIVISION

LBL-14677 c.2

Prepared for the U.S. Department of Energy under Contract DE-AC03-76SF00098

DISCLAIMER

This document was prepared as an account of work sponsored by the United States Government. While this document is believed to contain correct information, neither the United States Government nor any agency thereof, nor the Regents of the University of California, nor any of their employees, makes any warranty, express or implied, or assumes any legal responsibility for the accuracy, completeness, or usefulness of any information, apparatus, product, or process disclosed, or represents that its use would not infringe privately owned rights. Reference herein to any specific commercial product, process, or service by its trade name, trademark, manufacturer, or otherwise, does not necessarily constitute or imply its endorsement, recommendation, or favoring by the United States Government or any agency thereof, or the Regents of the University of California. The views and opinions of authors expressed herein do not necessarily state or reflect those of the United States Government or any agency thereof or the Regents of the University of California.

LBL-14677

A (p,2p) STUDY OF HIGH MOMENTUM COMPONENTS AT 2.1 GeV

Robert Neil Treuhaft

Ph.D. Thesis

July 1982

Nuclear Sciences Division
Lawrence Berkeley Laboratory
University of California
Berkeley, CA 94720

This work was supported by the Director, Office of Energy Research, Division of Nuclear Physics of the Office of High Energy and Nuclear Physics of the U.S. Department of Energy under Contract Number DE-AC03-76SF00098.

Acknowledgments

It is commonly supposed that experimental work is sustained only by an impersonal, objective desire to accurately describe physical phenomena. In practice there are many personalities who help to maintain the stamina needed to complete the work. The people who professionally and personally kept me going are gratefully acknowledged below.

I would like to thank my advisor Dr. Lee Schroeder for providing the intellectual atmosphere and practical support necessary to produce the work that follows. A few words of thanks to Prof. Guy Roche scarcely reflect his enormous contribution to the ideas expressed in this thesis. His ability and willingness to insightfully discuss mathematical and experimental matters are greatly appreciated. Thanks also go to Dr. Jorge Geaga who was a prime mover in the initial stages of the research. I had many fruitful discussions with Prof. Paul Kirk who helped define and maintain a standard of excellence for the project. I also thank Dr. John Harris for his time and ideas, and I thank the rest of the TASS collaboration and all the helpful people at Lawrence Berkeley Laboratory for contributing their expertise.

The limitless personal reassurance I received from family and friends is happily acknowledged. First, I would like to thank my mother Elaine, grandmother Leonore, sister Laurie, aunt Pearl, and

all other members of my family in New Jersey, both human and canine, for their constant long distance support. Their help in seeing me through the ups and downs, and their unswerving policy of being on my side have always been important to me and have contributed immeasurably to the completion of this dissertation. I thank Christen Hyde for kind encouragement and discussions which helped me maintain perspective and scientific integrity. Cousin Marian Chertow is gratefully acknowledged for bringing her professional talents and familial concern to the Bay Area. Finally, thank you to my close friends in California, Colorado, Illinois, Washington D.C., and New York-New Jersey for damping some anxiety and enhancing my happiness.

This work was supported by the Director, Office of Energy Research, Division of Nuclear Physics of the Office of High Energy and Nuclear Physics of the U.S. Department of Energy under Contract Number DE-AC03-76SF00098.

Table of Contents

1. Introduction 1

2. Observing a Correlated Pair 5

3. Kinematics 10

4. TASS: Description, Data Acquisition, and Specifications 16

5. TASS: Methods of Analysis and Calibration 33

6. Phase Space 47

7. Results and Discussion 55

8. Conclusions 73

Appendix A: General TASS Kinematics 76

Appendix B: The Analytic Acceptance Calculation 78

Appendix C: Schematic Model Calculations 80

References 84

List of Figures 86

Figures 90

A (p,2p) Study of High Momentum Components at 2.1 GeV

By

Robert Neil Treuhaft

Abstract

A (p,2p) experiment designed to isolate interactions with small numbers of fast nuclear constituents is described. Special attention is paid to the experimental manifestation and description of a correlated pair of nucleons in the nucleus. Phase space calculations are presented for the proton-pair three-body final state and for final states with larger numbers of particles. The Two Armed Spectrometer System (TASS) is described in detail. The data suggest the possibility of isolating an interaction with one or two nucleons in the nucleus which may have momenta far in excess of those described in a Fermi gas model.

CHAPTER 1

Introduction

A projectile incident on a nucleus may interact with only a few of the nuclear constituents. In that event, the four-momenta of a small number of final state particles can be used to kinematically infer the momenta of the objects struck. Electron scattering[1] and (p,2p) reactions[2] have been used to learn about the copious low momentum component of the nucleon wave function in the nucleus. This (p,2p) experiment, done at the Berkeley Bevalac under the number E444H, focuses on the high momentum component of the nuclear wave function by searching for a correlated pair of nucleons in the nucleus.

The existence of the correlated pair was hypothesized to explain the yield of backward going inclusive protons, produced with momenta far beyond the Fermi momentum, in proton-nucleus collisions.[3] Figure 1 shows the momentum density of protons produced at backward angles by protons of different incident energies on light nuclei. One obvious feature of the spectra is the observable cross section at momenta well above a typical Fermi momentum distribution width of 100 MeV/c. Since backward going nucleons are kinematically forbidden in free nucleon-nucleon scattering, it was thought that the large momenta observed in this and other singles experiments[4] reflected the high momentum component of a nucleon in the nuclear wave function. Quantum mechanically, a high nucleon momentum component can

arise from a strong spatial dependence of the nucleon's wave function on some other object in the nucleus. The simplest assumption is that the other object is another nucleon.

An alternative to the correlated pair hypothesis of the energetic backward protons is Quasi-Two-Body-Scaling, (QTBS), first suggested by Frankel[5] and recently resurrected by Gurvitz.[6] For a nucleus with A nucleons, QTBS describes the incident proton as scattering from one fast, backward going nucleon which is correlated to the other A-1 nucleons; the A-1 nucleons recoil coherently. As will be discussed in chapter 6, QTBS produces results slightly different from the correlated pair hypothesis when two particles are observed in the final state. The high momentum backward proton yield could also result from a series of scatterings on more than two nucleons in the nucleus. The many-body final state resulting from this mechanism has a phase space configuration which, for a (p,2p) experiment, is very different from that resulting from either a correlated pair or QTBS mechanism. Relying on final state kinematic signatures, the purpose of the experiment was to determine to what extent the pair or few-body signal can be distinguished from the many-body interaction.

The coincidence experiment which is the subject of this thesis was designed around the kinematic signal for scattering from a pair of nucleons in the nucleus. 2.1 GeV protons were scattered from carbon, and we detected a forward going and a backward going proton in coincidence. All events were taken essentially in a plane using the

Two Armed Spectrometer System, (TASS), built with the aim of constraining the anticipated three-body final state kinematics. The signature for scattering from a pair of nucleons, which are either correlated or uncorrelated, is an enhancement in the coincidence cross section near the phase space available to free proton-deuteron kinematics. This point will be demonstrated in chapter 2. Throughout this paper, the labels proton-deuteron and proton-pair refer to the same kinematic reaction and are therefore equivalent. Fixing the backward momentum vector and the forward angular coordinates, the signal for scattering from a nuclear pair, or observing free p-d kinematics, is one or two peaks in the forward going momentum spectrum, as will be detailed in chapter 6 on phase space calculations. The kinematic range of the magnetic spectrometer was set to encompass the three-body final state signal with wide forward momentum sweeps. Finding these enhancements is the first step in probing the dynamics of the nuclear deuteron. Although the original motivation for the experiment was to account for the backward singles spectra, the characteristics of the nuclear deuteron are of interest regardless of the magnitude of the contribution to the backward singles data. If identifiable, a description of the correlated pair, when compared to that of the free deuteron, could reveal how the nucleon pair interaction is modified by the nuclear field, providing, as is hoped, final state interactions can be taken care of. In fact, it would be interesting to demonstrate that any fraction of the backward proton spectrum results from an interaction with a small number of fast nucleons, rather than a large number of slow nucleons with

ordinary Fermi momentum. Such a demonstration would require a new description of how the subset of interacting nucleons acquired their high internal or center-of-mass momentum.

The plan of the paper is as follows: Chapter 2 describes the relationship between the correlated pair signal and free p-d kinematics. Chapter 3 outlines the kinematic regime associated with the free p-d reaction and the regime covered in this experiment. Since TASS was designed and built for this experiment, and its conception and implementation were a large part of the thesis work, chapters 4 and 5 describe the hardware of TASS, and the calibration, data acquisition, and data analysis techniques employed. Chapter 6 discusses the p-d kinematics with Fermi momentum of the deuteron center-of-mass. In chapter 6, the phase space associated with the other mechanisms mentioned above is also described. Chapter 7 contains the data and interpretations relative to the phase space considerations of chapter 6. The manifestations of high momentum components in the data are also discussed in chapter 7 and appendix C. The conclusions in chapter 8 discuss the relationship of these data to the observation of the correlated pair and the high momentum nuclear component. Other coincidence data are also mentioned along with suggestions for future experiments.

CHAPTER 2

Observing A Correlated Pair

The relationship between scattering from a correlated pair and the observation of free proton-deuteron kinematics is the basis for the plan of the experiment. Consider the kinematic signal for scattering from a nuclear pair. A nuclear pair is defined as two nucleons in the nucleus which may or may not have interdependent wave functions. To relate scattering from a nuclear pair to the proton-deuteron kinematics, one assumes that for a nucleus of A nucleons, the A-2 nucleons not in the pair suffer no momentum change in the collision process p + nucleus → 3 nucleons + A-2 spectators. In fact, in this impulse approximation it is assumed that the nuclear pair and the A-2 spectators are not bound to each other at all. For now, particle production is not considered.

The situation is shown in figure 2 where the incident proton interacts only with a nuclear pair leaving the A-2 residual nucleus as a spectator. The general kinematic equations relating the initial state to the final state are:

$$\vec{P}_{inc} = \sum_{p=1}^{3} \vec{P}_p + \vec{P}_{A-2}$$
$$E_{inc} + M_A = \sum_{p=1}^{3} E_p + E_{A-2} \qquad (2.1)$$

where $(E_{inc}, \vec{P}_{inc})$ is the incident proton's four-momentum, and M_A is the mass of the nucleus. $(E_p, \vec{P}_p)$ are the final state four-momenta of

the participant nucleons, which are the incident proton and the nuclear pair. $(E_{A-2},\vec{P}_{A-2})$ is the four-momentum of the spectator group either before or after the collision.

Let $(E_{pair},\vec{P}_{pair})$ be the four-momentum of the nuclear pair before the collision. The fact that the initial nucleus is at rest in the lab is expressed by

$$\begin{aligned} \vec{0} &= \vec{P}_{pair} + \vec{P}_{A-2} \\ M_A &= E_{pair} + E_{A-2} \end{aligned} \tag{2.2}$$

One derives from eqs. (2.1) and (2.2)

$$\begin{aligned} \vec{P}_{inc} + \vec{P}_{pair} &= \sum_{p=1}^{3} \vec{P}_p \\ E_{inc} + E_{pair} &= \sum_{p=1}^{3} E_p \end{aligned} \tag{2.3}$$

Eq. (2.3) has the form of the reaction $p + d \rightarrow p + p + n$ where the mass of the deuteron-like pair is given by $m_{pair} = (E^2_{pair} - |\vec{P}_{pair}|^2)^{1/2}$ and the proton-neutron mass difference is ignored. There is some ambiguity concerning the value of m_{pair}. If one takes $E_{A-2} = (|\vec{P}_{A-2}|^2 + M^2_{A-2})^{1/2}$ where M_{A-2} is the on-shell mass of the residual nucleus, then from eq. 2.2 and the definition of m_{pair}, m_{pair} will be less than the deuteron mass. For example, with A=12 and a high value of the pair momentum $|\vec{P}_{pair}| = 300$ MeV/c, m_{pair} is .9% lower than the on-shell deuteron mass. In all the kinematics that follow, this ambiguity is negligible.

The experiment was therefore designed around the kinematic situation where m_{pair} equals the on-shell deuteron mass. A continuum

of excitation energies of the nuclear pair would broaden the p-d kinematic solutions. If there were discreet excited states of the correlated pair, discreet phase space enhancements would appear for each m_{pair}. As will be seen in the discussion of the kinematics, large sweeps in phase space were taken about the p-d kinematics to allow for the possibility of different values of m_{pair}.

If one observes a nuclear pair by the kinematic signal described above, how does one know whether or not it is a correlated pair? A correlated pair is here defined as a nuclear pair for which the spatial wave function of each of the constituents is dependent upon the coordinates of the other. This can be illustrated with the quantum mechanical Fourier transform by letting $\Psi(\vec{r}_1,\vec{r}_2)$ be the wave function of the two nucleons with radius vectors $\vec{r}_1$ and $\vec{r}_2$ in the pair. With $\vec{k}_1$ and $\vec{k}_2$ the momenta of the two nucleons, the momentum space wave function is

$$\Phi(\vec{k}_1,\vec{k}_2) = \int d^3r_1\, d^3r_2\, \Psi(\vec{r}_1,\vec{r}_2)\, e^{-i\vec{k}_1\cdot\vec{r}_1}\, e^{-i\vec{k}_2\cdot\vec{r}_2} \qquad (2.4)$$

apart from proportionality constants. Transforming to the center of mass and relative position coordinates defined as

$$\vec{R} \equiv \frac{\vec{r}_1 + \vec{r}_2}{2} \quad \text{and} \quad \vec{r} \equiv \vec{r}_1 - \vec{r}_2$$

immediately gives

$$\Phi(\vec{K},\vec{q}) = \int d^3R\, e^{-i\vec{K}\cdot\vec{R}} \int d^3r\, e^{-i\vec{q}\cdot\vec{r}}\, \Psi(\vec{R},\vec{r})$$

where $\vec{K} \equiv \vec{k}_1 + \vec{k}_2$ and $\vec{q} \equiv \frac{\vec{k}_1 - \vec{k}_2}{2}$. Thus if $\nabla_r \Psi(\vec{R},\vec{r})$ is large, high

relative momentum of the nucleons will be an important part of the two particle wave function. Therefore a spatial correlation between the pair nucleons induces high relative momentum.

It would seem that the qualitative difference between a nuclear pair and a correlated pair lies in the determination of the relative momentum of the pair. But the above discussion applies to trivial as well as dynamic correlations. A dynamic correlation is one which is induced by an interaction Hamiltonian between the two nucleons; a trivial correlation is not induced by an interaction Hamiltonian. An example of a trivially correlated pair would be two independent plane waves with equal and opposite momenta. In this case one could have a high relative momentum between two particles which were really independent.

To get a feel for what constitutes a trivial correlation or relative momentum distribution for two nucleons in the nucleus, consider the single-nucleon momentum distribution given by Goldhaber for nuclear fragmentation:[7]

$$W(\vec{p}) = (2\pi\,\sigma^2)^{-3/2}\, e^{-p^2/2\sigma^2} \quad \text{with} \quad \sigma \simeq 90 \text{ MeV/c}$$

where $\vec{p}$ is the momentum of the single nucleon. The relative momentum density induced between two particles by this simple independent particle picture is:

$$W_{rel}(\vec{p}_r) = (2\pi\sigma^2)^{-3} \int e^{-k_1^2/2\sigma^2}\, e^{-k_2^2/2\sigma^2}\, \delta^3(\vec{p}_r - (\vec{k}_1 - \vec{k}_2))\, d^3k_1\, d^3k_2$$

where $\vec{p}_r$ is the relative momentum of the two particles defined as the

difference of their momentum vectors. Doing the integral yields

$$W_{rel}(\vec{p}_r) = (4\pi\ \sigma^2)^{-3/2}\ e^{-p_r^2/4\sigma^2} \tag{2.5}$$

Figure 3 shows this relative momentum density arising from a trivial correlation along with $W(\vec{P})$ for reference. The abscissa refers to $|\vec{p}|$ for $W(\vec{p})$ and to $|\vec{p}_r|$ for $W_{rel}(\vec{p}_r)$. In the figure $W(\vec{0})$ is set to 1, and all other points on both curves are normalized correctly relative to $W(\vec{0})$. This qualitative calculation shows a relative momentum spectrum which might be associated with a trivial correlation.

It is, of course, the dynamically correlated pair which is of interest, since its description could reveal details of the nucleon-nucleon interaction inside the nucleus, if final state interactions can be quantified or neglected. Again, the first step in finding the dynamically correlated pair is finding the kinematic signature of eq. (2.3). One must then impose dynamical assumptions which reproduce the data to see if some function of the observed momenta can be associated with the relative momentum of the pair. In other words, if the final state is consistent with an initial deuteron target with reasonable Fermi momentum, then scattering on a deuteron or nuclear pair will have been observed. But, to determine the internal momentum distribution of that deuteron would require an additional dynamical assumption. For example, one might assume that the backward-going nucleon was purely a spectator.

CHAPTER 3

Kinematics

To search for the signal for scattering from a correlated pair of nucleons in the nucleus, the reaction 2.1 GeV p + nucleus→p(backward) + p(forward) + X was studied at the Berkeley Bevatron. We looked for final state protons which satisfied the kinematics of the reaction 2.1 GeV p+d→p+p+n. What follows is a description of the kinematics of this reaction with the center-of-mass of the deuteron at rest. The most general kinematics appropriate to the apparatus, with Fermi momentum of the target included, is completely described in appendix A. Effects of Fermi momentum will be treated in the phase space calculation.

Initially, it is assumed that all three bodies in the final state are nucleons. The proton-neutron mass difference is ignored throughout. With the three momenta of the final state nucleons completely describing the system, there are nine degrees of freedom. There are four kinematic equations of constraint:

$$\begin{aligned} E_{inc}+m_d &= E_b+E_f+E_u \\ \vec{P}_{inc} &= \vec{P}_b+\vec{P}_f+\vec{P}_u \end{aligned} \tag{3.1}$$

where E_{inc} and $\vec{P}_{inc}$ are the total incident proton energy and momentum. m_d is the deuteron mass. The subscripts b,f, and u refer to the backward going proton, the forward going proton, and the unobserved neutron, respectively. If the nuclear pair were two protons

instead of a nuclear deuteron, the unobserved particle would also be a proton.

Figure 4 shows a schematic, planar picture of the situation. In the coordinate system used, the $\vec{P}_{inc}$ vector defines the polar z-axis. As drawn, the vector $\vec{P}_f$ is on the azimuthal $\phi=0^o$ side of $\vec{P}_{inc}$, and $\vec{P}_b$ and $\vec{P}_u$ have the azimuthal coordinate $\phi=180^o$.

With the four equations of constraint, eq. (3.1), five input parameters are necessary to uniquely restrict the problem. It is most convenient for TASS to specify as input constraints the three components of the backward momentum $\vec{P}_b$ and the angular coordinates θ_f and ϕ_f of the forward going proton. The azimuthal coordinates are as described above, and all data were taken with the rear polar angle $\theta_b=120^o$. With these three angular coordinates specified, each combination of $|\vec{P}_b|$ and θ_f provides the five inputs necessary to completely determine the front momentum magnitude $|\vec{P}_f|$ and the unobserved nucleon momentum vector $\vec{P}_u$. The solutions for $P_f \equiv |\vec{P}_f|$ and hence for $\vec{P}_u$ are often double valued.

Figure 5 shows the three-body final state kinematics. The contours are of constant $P_b \equiv |\vec{P}_b|$. For θ_f, θ_b, and ϕ_b as above, a solution for P_b, is obtained by finding θ_f on the x-axis, going up to the desired P_b contour , and across to the value on the y-axis. Because of energy conservation, if we observe, for example, the lower momentum root proton going forward, the unobserved nucleon is fast, and observing the high momentum root means the unobserved nucleon is slow. The point in the center of the plot represents the condition

when the unobserved nucleon and the forward going proton go off together and thus represents elastic p-d kinematics.

Table 1 shows the values of P_b, P_f, and θ_f spanned in the experiment. All the parameters mentioned below were run with a carbon target. Copper was also used for a small number of the configurations. P_{cb} and P_{cf} are the rear and front central momentum values which are defined in chapter 4. All momenta in table 1 are given in MeV/c, and all angles in degrees.

Table 1: Run Parameters

P_{cb}	P_b Range	P_{cf}	P_f Range	θ_f
566	400-850	622	400-900	10.4
566	400-850	1222	800-1800	10.4
566	400-850	2151	1500-3200	10.4
417	290-625	426	300-640	45.0
417	290-625	922	600-1400	45.0
417	290-625	424	300-640	60.0

Front momentum sweeps were taken along two different vertical lines of constant forward angle at 10.4^o and 45°. A small amount of data were also taken at $\theta_f = 60^o$ which is outside of the free proton-pair kinematics. The 10.4^o angle was chosen in part because it goes through the p-d elastic singularity, which was explored by Komarov et. al. at 600 MeV incident energy.[8] Thus if we restricted ourselves to the backward momentum range $600 \leq |\vec{P}_b| \leq 700$ MeV/c, and if proton-pair scattering were a dominant contribution to the coincidence signal, we should detect an enhancement in the cross section as a function of forward momentum in the mid-momentum region. Since we covered a wide backward momentum range, cutting the 10.4^o data

off-line on lower backward momenta should produce two separate peaks in forward momentum, one for each root in figure 5. In contrast, the $\theta_f=45^o$ front momentum sweep should yield two very close roots for a narrow, low backward momentum range. The two forward angles, one passing through the center of the egg-shaped contours and one at the edge, represent extremum of the p-d breakup kinematics and were thus thought to be good choices in the initial search for the correlated pair in the nucleus.

Since the nucleon-nucleon cross section is roughly half inelastic at this energy, particle production must be considered. The missing or unobserved mass is defined as

$$M=((E_{inc}+m_d-E_b-E_f)^2-(\vec{P}_{inc}-\vec{P}_b-\vec{P}_f)^2)^{1/2} \qquad (3.2)$$

With the three nucleon final state, the missing mass should be the nucleon mass. However, if a particle is produced in the interaction, the missing mass is greater than that of the nucleon. Figure 6 shows the $|\vec{P}_b|=400$ MeV/c contour as it is normally, in the absence of particle production, with the solid line. The dotted line shows what happens to the contour if M=1078 MeV, which corresponds to an unobserved nucleon and pion going off together. To further demonstrate the trend, the dashed contour corresponds to a missing delta resonance mass of M=1232 MeV. The contours contract with increasing missing mass. Depending on the actual missing mass spectrum and the effect of Fermi momentum, the contours of figure 5 could be distinguished from or broadened by the higher missing mass contours. These possibilities will be considered in the phase space

calculation.

It is worthwhile to mention the proton-pair dynamic possibilities associated with the kinematic regions investigated. Figure 7a shows two different ways to interpret the three nucleon final state in a single scattering picture. The bottom two horizontal lines represent two interacting nucleons in the nucleus, while the top line represents the incident proton. The wavy line indicates a fundamental nucleon-nucleon interaction, while the solid, double line signifies the target nuclear pair correlation, usually assumed to be close to the deuteron internal interaction. The labels on the right side of the figure refer to the outgoing particles where P_1 is always detected going forward. In the case labeled without parentheses, the backward going proton P_b participates in the nucleon-nucleon scattering. For the case denoted with parentheses, the backward going proton is a spectator and thus presumably reflects the proton momentum before the interaction. Kinematics does not distinguish between these two possibilities, therefore for each root solution of the kinematics, there is an ambiguity as to how to interpret the backward going particle's momentum: Does it arise primarily from the target wave function, or is it also due to the interaction with the incident proton? Only a dynamical assumption can distinguish between the two cases. Of course, the proton-pair kinematics also permits a multiple scattering on two nucleons which are either correlated or uncorrelated. Figure 7b shows the multiple scattering situation with two fundamental nucleon-nucleon interactions. The solid, double line

would of course be absent in the uncorrelated pair scattering. Thus the mere observation of the appropriate three-body final state kinematic enhancements does not uniquely determine the internal momentum distribution of the target pair, nor does it guarantee that the pair nucleons were correlated at all. One must relate the enhancements to one or more of the diagrams in figure 7 to extract the strength of the correlation.

CHAPTER 4

TASS: Description, Data Acquisition, and Specifications

The Two Armed Spectrometer System, which was designed and built for this experiment, consists of two independently rotatable magnetic spectrometer systems. This chapter describes the hardware parameters and methods of data acquisition of TASS at the time of E444H. Chronologically, most of the ideas mentioned here were implemented before any beam from the accelerator was sent to the apparatus. The three sections which follow describe the layout and coordinate system of TASS, the data acquisition via the computer software and hardware, and the physical and mathematical properties of the magnet-counter system including its resolution and acceptance specifications.

1. Spectrometer Apparatus and Coordinate System

As indicated in figure 8, the two arms of TASS each have identical magnets but different counter configurations. The rear arm consists of one three-element scintillator hodoscope, R1, and two scintillator gating counters, R2 and R3. In addition, there are two wire chambers labeled WC1 and WC2 each with 2 millimeter wire spacing. R1, WC1, and WC2 are used for ray tracing through the magnetic field. The acceptance of the rear arm is defined by R1 and R3. In the front arm, there are two sixteen element scintillator hodoscopes, F1 and F2. There are also two gating counters, F0 and F3. Upstream of the target is an ion chamber (IC) for monitoring absolute beam intensity.

Two telescopes not shown in figure 8, consisting of two scintillators each, were pointed at the ion chamber from above and from the side to monitor relative beam intensity. We attempted to use the multiplicity array (MA) shown in figure 8 but the high beam intensities rendered the array useless for the coincidence running. Labeled by BC, is a Morgado beam chamber which is used to determine the beam location near the target. This chamber and its associated hardware integrate the charge deposited from a one second beam spill on each of 64 wires, 32 horizontal and 32 vertical. The wire spacing is two millimeters. The integrated charge for each of the wires is converted to a number and sent to the computer. For the front arm, momentum determination is made by using the target position as determined by the beam chamber and the F1 and F2 hodoscopes. All counter positions and dimensions are given in inches in table 2.

Table 2: Counter Dimensions

Counter	Distance	Width	Height	Thickness
R1	24.00	1.50	2.75	.094
R2	90.94	8.25	6.00	.125
WC1	102.60	12.75	10.00	-
R3	132.47	12.75	10.00	.250
WC2	142.88	15.00	13.85	-
F0	32.50	4.00	2.00	.125
F1	94.17	8.00	4.00	.125
F2	135.09	8.00	6.00	.125
F3	145.54	8.00	6.00	.250

The second column in table 2 gives the distance of the counters from the pivot center of TASS. Not mentioned above are the distances from the target to the magnet pole tip and the length of the magnets. These are 42 inches and 36 inches respectively for both arms.

The coordinate system is similar to that used by Enge,[9] and is the same for both arms. The magnetic field in the dipoles is pointing downward, so positively charged particles starting from the target get bent to the left as they traverse the field. Looking from above one arm, figure 9 shows the various angles associated with the coordinate system used. A central ray is defined by the solid lines entering and exiting the magnet in figure 9. α_o and β_o are called the entrance and exit angles and are the angles that the central ray makes with the normal to the entrance and exit of the magnet respectively. For the rear and front arms α_o was 7.6^o and 7.2^o. The sum of the exit and entrance angles is the central bend angle, θ_o, which was set to 15° for both arms. The central momentum P_c, which is a function of the magnetic field, is defined as that momentum which produces a trajectory along the central ray for a charge +1 particle. All particles are assumed to have charge +1 throughout this paper.

All position and direction coordinates are given relative to the central ray either before or after the magnet. The x-z plane is defined for each arm to be normal to the central ray. The positive y direction points from the target along the central ray. The positive z direction is up, or out of the plane of the paper in figure 9, and the positive x direction points to the right looking from the target, or away from the direction of curvature. A particle's local trajectory is completely described by x, y, z, θ_x, and θ_z; where θ_x is the arcsine $\frac{P_x}{|\vec{P}|}$ and θ_z = arcsine $\frac{P_z}{|\vec{P}|}$ for a particle of momentum $\vec{P}$. The momentum of a particle is usually expressed by its fractional

deviation from the central momentum, δ, defined as $\delta \equiv \frac{|\vec{P}| - P_c}{P_c}$.

The spectrometer system of either arm determines the momentum of a particle by relating the x, z, θ_x, and θ_z coordinates before the magnetic field to those after the field. For a central momentum particle directed along the central ray, the coordinates would all be equal to zero before and after the magnet. In general the magnetic field can be regarded as a one to one transformation of the entrance coordinates, $(x_{en}, z_{en}, \theta_{x\ en}, \theta_{z\ en})$, to the exit coordinates, $(x_{ex}, z_{ex}, \theta_{x\ ex}, \theta_{z\ ex})$. Calling $M(\delta)$ the mathematical coordinate transformation induced for momentum fraction δ by the magnet,

$$(x_{ex}, z_{ex}, \theta_{x\ ex}, \theta_{z\ ex}) = M(\delta)\ (x_{en}, z_{en}, \theta_{x\ en}, \theta_{z\ en}) \qquad (4.1)$$

where it is understood that the y coordinate is the magnet entrance and exit coordinate for the right and left sides of eq. 4.1 respectively.

Using the rear arm as an example, the measured positions will be called (x_1, z_1) at R1, (x_2, z_2) at WC1, and (x_3, z_3) at WC2. These positions are given by the locations of scintillator elements and wires which show signals. Knowing the distance between WC1 and WC2 gives $(x_{ex}, z_{ex}, \theta_{x\ ex}, \theta_{z\ ex})$ at the magnet exit. Then

$$(x_{en}, z_{en}, \theta_{x\ en}, \theta_{z\ en}) = M(\delta)^{-1}(x_{ex}, z_{ex}, \theta_{x\ ex}, \theta_{z\ ex}) \qquad (4.2)$$

If d is the distance between the boundary of the magnetic field and R1,

$$(x_{en}, z_{en}) = (x_1, z_1) + d\ \tan(\theta_{x\ en}, \theta_{z\ en}) \qquad (4.3)$$

The problem is to find the δ which produces a spatial coordinate $(x_{en}, z_{en}, \theta_{x\ en}, \theta_{z\ en})$ which satisfies eqs. 4.2 and 4.3 given the exit coordinates inferred from the wire chamber hits. As will be seen in section 3 of this chapter, the field is well approximated by a homogeneous field in the negative z direction, and the solution of eqs. 4.2 and 4.3 are found iteratively. Note that in the process of determining δ, $\theta_{x\ en}$, and x_{en}, the target angle and position of the ray are also determined. For the front arm, the target position plays the role of the R1 scintillator position in the rear arm. The wire positions are replaced by F1 and F2 hodoscope element positions.

2. Data Acquisition

In addition to the position data needed for eqs. 4.2 and 4.3, many other parameters such as the mass and beam intensity must be inferred from the raw data taken. The system used for data acquisition is outlined in the flow chart of figure 10.

Initially all signals from the scintillator counters are sent to the trigger logic electronics. A rear arm trigger is defined as R: R1·R2·R3. Figure 11 shows the logic diagram which defines real coincidences. The philosophy behind the trigger timing in either arm is to accept particles between $\beta = 1$ and $\beta = .26$, where β is the ratio of the particle's speed to the speed of light. These limits for β correspond to the fastest possible particle and the lowest momentum proton which would not be stopped by the apparatus, which is about

250 MeV/c. Below the R trigger in figure 11 is the front arm trigger F: F0·F1·F2·F3, where F1 and F2 each require at least one signal from any of the 16 elements. The R·F coincidence logic is is also shown. Again the philosophy in the time intervals for signals entering the R·F AND unit is to allow coincidences between the fastest observed particles in one arm with the slowest in the other. This consideration produced an R·F gate width of about 60 nsec. Naturally, the narrower the gate widths, the less possibility of random events in either or both arms. The spectrometer system could be run in any combination of trigger modes, R, F, or R·F, depending on the switch settings of a majority logic unit.

Referring back to figure 10, the next step in the decision to accept an event is performed by the slow logic. It is outlined in figure 12 and makes decisions on three logic levels: RUN, RUN·SPILL, and RUN·SPILL·$\overline{\text{BUSY}}$. RUN means the computer is on but there may or may not be a beam spill. RUN·SPILL means the computer is on and the spill is present. RUN·SPILL·$\overline{\text{BUSY}}$ means RUN·SPILL is true and the computer is not busy processing any other event. Any coincidence event, called event type 1, is gated by RUN·SPILL·$\overline{\text{BUSY}}$. In addition, scalers gated by these three levels assess the dead time of the system. The time needed to process an event type 1 is about 600 μs without writing to tape, and a plot of events accepted in the live time of the computer versus events fed to the computer is shown in figure 13. The dashed curve was generated from the response of the system to a pulser input with the frequency of the points on the

abscissa. The random noise generated curve, however, was measured from the response of photo tube noise. It is seen that a reasonable live time of 80% can be attained with a real trigger rate of about 150/spill. Since neither curve was generated from the accelerator beam, this live time should be regarded as an upper limit of the system for a given real event rate, as high frequency structure in the beam can greatly reduce the live time. Live time as measured by the ratio of RUN•SPILL•$\overline{\text{BUSY}}$ and RUN•SPILL gated scalers must be folded into the normalization of all cross sections. For the (p,2p) running on carbon at back angles, the live time was always greater than 90%.

After an event satisfies the fast logic timing and slow logic selection, all the signals to be recorded are sent to the two CAMAC crates. The CAMAC modules were read using a Multi Branch Driver (MBD) which gets data from CAMAC and puts it into a buffer in the memory of a PDP 11/34 computer. When the buffer is full, the data are written to tape. Table 3a lists on the next page the signals recorded for any coincidence event type 1. The symbols T1...T8 and B1...B8 refer to the multiplicity array elements. The first five data words refer to the event length and identification. Any label preceded by a "d", such as DTDC or dlatch, refers to a coincidence R•F circuit deliberately out of time to simulate random events. This circuit was not used in the analysis; it was not needed because random signals were measured by methods described in chapter 5.

At the end of the spill, scalers and the beam chamber and other modules were read. The end of spill was called event type 8, and the

quantities read are listed in table 3b on page 24. Unless otherwise specified, the symbols in table 3b refer to RUN·SPILL gated scalers.

Table 3a: Event Type 1 Data Words

Number	Contents	Number	Contents	Number	Contents
1	length	26	B3 TDC	51	B4 ADC
2	ID	27	B4 TDC	52	rear latch
3	run #	28	B5 TDC	53	F1 latch
4	seq #	29	B6 TDC	54	F2 latch
5	seq carry	30	B7 TDC	55	front latch
6	R1A TDC	31	B8 TDC	56	F0 DTDC
7	R1B TDC	32	F0 ADC	57	F3A DTDC
8	R1C TDC	33	F3A ADC	58	F3B DTDC
9	R2A TDC	34	F3B ADC	59	F1 dlatch
10	R2B TDC	35	T2 ADC	60	F2 dlatch
11	R3A TDC	36	T3 ADC	61	F0 DADC
12	R3B TDC	37	T4 ADC	62	F3A DADC
13	F0 TDC	38	T5 ADC	63	F3B DADC
14	F3A TDC	39	T7 ADC	64	F1 FTDC
15	F3B TDC	40	R1A ADC	65	F2 FTDC
16	T1 TDC	41	R1B ADC	66	F3A FTDC
17	T2 TDC	42	R1C ADC	67	F3B FTDC
18	T3 TDC	43	R2A ADC	68 & 69	R SCALER
19	T4 TDC	44	R2B ADC	70 & 71	F SCALER
20	T5 TDC	45	R3A ADC	72 & 73	R·F SCALER
21	T6 TDC	46	R3B ADC	74 & 75	MU SCALER
22	T7 TDC	47	T8 ADC	76 & 77	MD SCALER
23	T8 TDC	48	B1 ADC	78 & 79	EMPTY
24	B1 TDC	49	B2 ADC	80	1st WC word
25	B2 TDC	50	B3 ADC	--	--

MU and MD in table 3b refer to the relative intensity monitors mentioned in section 1 of this chapter. IC refers to the ion chamber and BC refers to the beam chamber. Figure 14 shows a flow chart of the subroutines specifically written for this experiment. The main program, written by Everett Harvey, is called QDA1.[10] All words read by the data acquisition program into the PDP 11/34 were 16 bits long.

Table 3b: Event Type 8 Data Words

Number	Contents	Number	Contents	Number	Contents
1	length	44 & 45	F2-1	92 & 93	R1-OR
2	ID	46 & 47	F2-2	94 & 95	IC
3	run #	48 & 49	F2-3	96 & 97	MU (R)
4	seq #	50 & 51	F2-4	98 & 99	MD (R)
5	seq carry	52 & 53	F2-5	100 & 101	EMPTY
6 & 7	R	54 & 55	F2-6	102	R $(R \cdot S \cdot \overline{B})$
8 & 9	F	56 & 57	F2-7	103	F $(R \cdot S \cdot \overline{B})$
10 & 11	$R \cdot F$	58 & 59	F2-8	104	$R \cdot F$ $(R \cdot S \cdot \overline{B})$
12 & 13	F1-1	60 & 61	F2-9	105	D-$R \cdot F$ $(R \cdot S \cdot \overline{B})$
14 & 15	F1-2	62 & 63	F2-10	106 & 107	R1A
16 & 17	F1-3	64 & 65	F2-11	108 & 109	R1B
18 & 19	F1-4	66 & 67	F2-12	110 & 111	R1C
20 & 21	F1-5	68 & 69	F2-13	112 & 113	R2A
22 & 23	F1-6	70 & 71	F2-14	114 & 115	R2B
24 & 25	F1-7	72 & 73	F2-15	116 & 117	R3A
26 & 27	F1-8	74 & 75	F2-16	118 & 119	R3B
28 & 29	F1-9	76 & 77	D-$R \cdot F$	120 & 121	F0
30 & 31	F1-10	78 & 79	MU	122 & 123	F1 OR
32 & 33	F1-11	80 & 81	MD	124 & 125	F2 OR
34 & 35	F1-12	82 & 83	F3A	126 & 127	WC1
36 & 37	F1-13	84 & 85	F3B	128 & 129	WC2
38 & 39	F1-14	86 & 87	MU $(R \cdot S \cdot \overline{B})$	130 - 133	MAG DVM
40 & 41	F1-15	88 & 89	MD $(R \cdot S \cdot \overline{B})$	134 - 197	BC
42 & 43	F1-16	90 & 91	DR $(R \cdot S \cdot \overline{B})$	--	--

3. Physical and Mathematical Characteristics of TASS

To interpret the raw data, the magnetic field and its mathematical transformation between counter hits and particle momenta must be understood. Field measurements and the method for calculating momenta are discussed in section 3.1 below. Two important characteristics of the spectrometers which depend on the field-counter configuration are the three-momentum resolution and efficiency of the system; they are described in section 3.2.

3.1. The Magnetic Field

The field was measured by means of a wire orbit technique. A current running through a wire under tension is set to simulate a given momentum, and the trajectory of the wire through the system determines the field. The accuracy of the wire orbit technique including effects of the mass of the wire, was determined empirically to be about $\pm 1\%$. We found that the field in each magnet was well approximated by a homogeneous field covering the entire x-z plane for $-.3 \leq \delta \leq .5$. For the y direction, the homogeneous field was considered to span an effective length which was equal to the real length of the magnet plus half the magnet gap height. With the magnets 36" long by 16" wide by 8" high, the effective length (EFL) was taken to be 40.94" for both magnets. The choice of EFL was prompted by mapping measurements done on the rear magnet[11] and standard fringe field theory.[12] The final results, which are actually rather insensitive to the choice of EFL, are shown in figures 15a and 15b. These two figures show for one central momentum each the deviation of the wire orbit measurement from the square field model. The abscissa is the percent deviation of the momentum as determined by the wire trajectory through a square field, from the momentum as determined by the current in the wire. Wire momenta were determined by the current in the wire to better than .1%. In the wire orbit process, many central momenta or central fields were taken spanning the central momentum range $300 \leq P_c \leq 2200$ MeV/c. The conclusion is that for the small region of the magnet gap used, the magnetic field could be considered square

to 1.5%. In the front arm, the systematic trend of figure 15b to overestimate low momenta and underestimate high momenta was folded into the square field model as a correction for momentum determination. From the wire orbit data, it was found that the square field model reconstructs the angle of a ray at the target to 0.1^{o}.

The details of the square field model lead to the method for calculating momenta in either arm. All z coordinates are unaffected by the field and are thus transported through the magnet as through free space. We wish to solve a simplified version of eqs. 4.2 and 4.3 for x_{en}, $\theta_{x\ en}$, and δ:

$$(x_{en},\theta_{x\ en}) = M^{-1}(\delta)\ (x_{ex},\theta_{x\ ex}) \tag{4.4}$$

$$x_{en} = x_1 + d\ \tan\theta_{x\ en} \tag{4.5}$$

From the wire orbit procedure, we know that a given magnet current corresponds to a given central momentum. The central momentum is related to the effective central field magnitude B_o by

$$P_c = .3R_cB_o \tag{4.6}$$

where R_c is the radius in centimeters of the circular arc traced through the field by a central momentum particle. B_o is in kgauss and P_c is in MeV/c.

One can consider the trajectory of any general ray through the magnet by replacing the dashed line inside the magnet in figure 9 with a circular trajectory joining the entrance and exit rays. One must also imagine the solid lines of figure 9 to describe an arbitrary trajectory and not necessarily the central ray. For a general

ray of momentum P

$$EFL = R(\sin\alpha + \sin\beta)$$
$$P = .3RB_o \tag{4.7}$$

where α and β are the magnet entrance and exit angles of the particle and R is the radius of curvature for the trajectory through the field B_o. The entrance and exit angles are related to the central angles by

$$\alpha = \alpha_o + \theta_{x\ en}$$
$$\beta = \beta_o - \theta_{x\ ex}$$

From eqs. 4.6, and 4.7

$$\frac{P}{P_c} = \frac{\sin\alpha_o + \sin\beta_o}{\sin\alpha + \sin\beta}$$

In terms of δ defined above

$$\delta = \frac{\sin\alpha_o + \sin\beta_o}{\sin\alpha + \sin\beta} - 1 \tag{4.8}$$

For any general circular arc in the magnet,

$$X_{en} - X_{ex} = R(\cos\alpha - \cos\beta)$$
$$= EFL\,\frac{(\cos\alpha - \cos\beta)}{(\sin\alpha + \sin\beta)} \tag{4.9}$$

where $X_{en} = \frac{x_{en}\cos\theta_{x\ en}}{\cos\alpha}$ and $X_{ex} = \frac{x_{ex}\cos\theta_{x\ ex}}{\cos\beta}$. As mentioned in section 1, the angle β, or equivalently $\theta_{x\ ex}$, and x_{ex} are found directly from the wire hits in WC1 and WC2. Thus for the three unknowns x_{en}, α, and δ we have eqs. 4.5, 4.8, and 4.9. These equations are solved iteratively for each trajectory with Newton's method.

3.2. Resolution and Acceptance

Given the essentially square field, one can numerically calculate the resolution of each arm by the following method. One selects the momentum fraction, δ_s, at which the resolution is desired and traces a ray from the target through the system for any initial angle. For the rear arm, for example, one then obtains x positions at R1, WC1, and WC2. The homogeneous field model includes z coordinate independence of the momentum. With the x position on each ray-determining device, x positions are randomly chosen that are within $\pm.5$ the element size from the initial ray position. This means doing a Monte Carlo over $\pm.25''$ for R1 and $\pm 0.039''$ for the two wire chambers. One then calculates the deviation of each δ_i calculated from the ith randomly thrown event from δ_s, the selected momentum fraction. The resolution is then calculated as

$$\sigma_\delta = \sqrt{\frac{\sum_{i=1}^{N} (\delta_i - \delta_s)^2}{N} - \left[\frac{\sum_{i=1}^{N} (\delta_i - \delta_s)}{N}\right]^2} \qquad (4.10)$$

where N is the number of randomly thrown counter position combinations. For large N the second term under the square root sign is 0. The resolutions as a function of δ_s for each arm are given in figures 16a and 16b.

With the square field geometry, one can also calculate the acceptance of the system. Ignoring energy loss and multiple scattering, the acceptance of the system describes the system's efficiency

for detecting a particle as a function of the three-momentum $\vec{P}$. If, for each momentum magnitude $|\vec{P}| \equiv P$, various elements of solid angle Ω had transmission or efficiency $T(P,\Omega)$, then for each P, an average solid angle would be given by

$$\overline{\Delta\Omega}(P) = \int_{4\pi} d\Omega\ T(P,\Omega) \tag{4.11}$$

P and Ω are coupled in a magnetic system because slower particles must enter the field at larger angles in order to suffer a large bend and still hit the counters behind the field.

Considering each arm separately for now, solid angle averaged over a momentum region between P_1 and P_2 is expressed as

$$\overline{\Delta\Omega}_{P_1,P_2} = \frac{\int_{P_1}^{P_2}\int_{4\pi} d\Omega\ T(P,\Omega)\ dP}{\int_{P_1}^{P_2} dP} \tag{4.12}$$

where $T(P,\Omega)$ is the efficiency for transmitting a particle with momentum between P and P+dP and solid angle between Ω and $\Omega+d\Omega$. This function $T(P,\Omega)$ contains the complete description of the spectrometer acceptance. To get a momentum spectrum, one tries to make $\Delta P \equiv P_2-P_1$ as small as possible and still achieve good statistics for a cross section. The most useful expression of acceptance is then

$$\Delta P\overline{\Delta\Omega}_{P_1,P_2} \equiv \Delta P\Delta\Omega = \int_{P_1}^{P_2}\int_{4\pi} T(P,\Omega)\ d\Omega dP \tag{4.13}$$

To calculate $\Delta P\Delta\Omega$, one obtains $\overline{\Delta\Omega}(P)$ from eq. 4.11 and integrates over the desired momentum range. Figures 17a and 17b show $\overline{\Delta\Omega}(P)$ for

each arm for a typical beam spot size. The deviations in fractional acceptance from 100% show that the anglular acceptance decreases at large deviations from the central momentum. Appendix B describes the analytic method for calculating $\overline{\Delta\Omega}(P)$ and the function $T(P,\Omega)$.

We must now consider both arms operating together via the quantity $[(\Delta P\Delta\Omega)_b\ (\Delta P\Delta\Omega)_f]$, where b and f refer to the rear and front arms. Eq. 4.11 generalizes to

$$\overline{\Delta\Omega_b}\overline{\Delta\Omega_f}(P_b,P_f) = \int d\Omega_b\ d\Omega_f\ T(P_b,\Omega_b,P_f,\Omega_f) \tag{4.14}$$

where $T(P_b,\Omega_b,P_f,\Omega_f)$ is now the efficiency for detecting two particles of momentum $\vec{P}_b$ and $\vec{P}_f$ simultaneously. The calculation for the transmission function T is the same as in appendix B, but the fraction of the beam seen by both arms must be considered as a function of the front-back momentum combination. Because the time and money spent computing the coincidence acceptance is staggering, I will show that for small beam spots, the coincidence acceptance is the product of the singles acceptances as calculated in appendix B. That is

$$[\overline{\Delta\Omega_b}\overline{\Delta\Omega_f}](P_b,P_f) = \overline{\Delta\Omega_b}(P_b)\overline{\Delta\Omega_f}(P_f) \tag{4.15}$$

which reduces the problem to the calculation of eq. 4.11 twice.

As implied by the calculation of the single-arm transmission in appendix B, T is either 0 or 1 for each $(\vec{P}_b,\vec{P}_f)$ combination for a point beam. In particular, the coincidence T is 0 if either arm cannot transmit its particle and 1 if they both can. So

$$T(P_b,\Omega_b,P_f,\Omega_f) = T(P_b,\Omega_b)\ T(P_f,\Omega_f) \tag{4.16}$$

Once T is thus decomposed, the integral in eq. 4.14 immediately gives

eq. 4.15. Quantitatively, the beam must be small relative to the size of the acceptance defining counters. If so, the beam would either be completely seen or completely missed for most momentum vectors. To be sure that eq. 4.15 and 4.16 hold, the coincidence and the product of the single-arm analytic acceptances were compared for a typical beam spot. It was found that the two arms could in fact be decoupled and the single-arm acceptances multiplied.

In addition to the analytic calculation, the acceptance of the system was also calculated using a Monte Carlo simulation method. In this method events are randomly thrown from the target to see if they clear the apparatus. The fraction that successfully hit all counters is related to the T quantities as functions of the momentum vectors. The Monte Carlo method includes multiple scattering and energy loss in the system. It was found that multiple scattering has a negligible effect on the acceptance for most of the (p,2p) coincidence running. There is a considerable effect due to multiple scattering for the proton-proton elastic scattering calibration runs which will be discussed in detail in chapter 5. The effect of energy loss is to shift the momentum scale of either arm by about 3% in the momentum region $300 \leq P \leq 600$ MeV/c. At higher momenta, energy loss can also be ignored.

The Monte Carlo method also reconstructs the momenta of trajectories as seen by the spectrometer. Biases introduced by momentum reconstruction were important for some of the running. These biases occur because each arm of TASS has a discreet number of measurable

momentum values since the hodoscope elements and wire chambers give discreet spatial coordinates for trajectories. Fractional reconstruction biases on the order of 1/N occur when the momentum bin chosen for cross sections includes N measurable momenta. For the rear bins in the proton-proton elastic scattering and for the front bins at high momenta, the reconstruction biases were on the order of 10-25%. The Monte Carlo calculation was used to correct for these biases whenever they were higher than 5%.

CHAPTER 5

TASS: Methods of Analysis and Calibration

The coincidence cross section for (p,2p) reactions is very small and is characterized by a low count rate per beam spill. For example, for a typical beam spill of 10^9 protons incident on carbon, of the 10^4 single triggers in the rear arm and 10^6 triggers in the front arm, 5 triggers would be coincidence. This low count rate necessitates on-line momentum and mass determination and real to random separation, so that a good estimate of the real proton-proton coincidences per momentum bin can be made while running. Section 1 below describes the on-line and off-line momentum and mass assignment techniques, while section 2 outlines the method of separating the real and random events. Section 3 describes the calibration of the system using known kinematics and previously measured cross sections.

1. Momentum and Mass Determination

The momentum is determined from a knowledge of P_c the central momentum and three x positions of the trajectories as described in chapter 4. All wire chambers, scintillator hodoscopes, and gating counters were surveyed with transits to an accuracy of ± 1 millimeter. For the rear arm, one hodoscope element of the R1 counter must be hit along with one x-wire from each wire chamber. In the front arm, the beam chamber distribution must be known along with a signal from one element in F1 and one in F2. The analysis code, which was introduced

as subroutines into the Fermi Lab Multi program,[13] first had to decide if the required counters were each hit just once per coincidence trigger. Double hits on any hodoscope or wire chamber, or misses in the wire chambers none of which were in the trigger, had to be considered unanalyzable; these events contributed to the inefficiency of the system at the level of 10-45%, depending on the run mode, beam intensity, and spectrometer position. Double hits in hodoscopes and wire chamber were the largest source of unanalyzable events. A double hit in a counter was usually caused by a real event going completely through the system plus a stray particle hitting just that counter.

In the rear arm, a second analyzable convention was adopted. An R1 hit plus one x hit from either wire chamber was considered analyzable, as opposed to requiring an x hit from each chamber as mentioned in the previous paragraph. This second convention was adopted off-line and used in conjunction with the target position given by the beam chamber. The convention was used to gather more statistics at the expense of momentum resolution. For the two conventions, the average rear arm momentum resolution was about 7%. Since rear momentum bins of 100 MeV/c were eventually taken, the increase in resolution width over that of figure 15a was not a problem.

To obtain mass information, the time-to-digital converters (TDC's) must be used to infer a speed and thus a mass M via

$$M = \frac{P}{\beta\gamma} \tag{5.1}$$

where β and γ are the standard Lorentz factors for a particle of

momentum P. In both arms, clocks were started with a hit at R1. TDC clocks were stopped at R2, R3, F0, and F3. Time in the arms was computed using the quantities

$$t_r \equiv \frac{R3A + R3B}{2}$$
$$t_f \equiv \frac{F3A + F3B}{2} - F0$$

where R3A and R3B indicate the raw TDC counts from the two photo tubes on either end of the R3 scintillator, F3A and F3B are the raw counts from the two tubes of F3. Note that t_f is independent of the rear arm since the dependence on the R1 start time is subtracted out.

To relate t_r to the actual time it takes for a particle to travel from R1 to R3, use was made of the proton-proton elastic scattering and 120° proton singles runs discussed in detail in section 3. In the p-p elastic and singles run, the proton peaks were easily discernible on a momentum versus time of flight scatter plot. Figure 18 shows a scatter plot of rear momentum versus t_r for a typical coincidence run of 2.1 GeV p + carbon $\rightarrow$ p + p + X. The ellipse shows where the p-p elastic run populates the scatter plot. Deuterons can also be seen in the figure. In order to convert these raw TDC counts to real time, the actual time in nanoseconds was calculated for the path length between R1 and R3 for various rear momentum cuts. This real time was found to be linear in t_r, and the equation which relates t_r to the real time in nanoseconds T_r is

$$T_r = .048\ t_r - 2.0 \qquad (5.2)$$

Depending on which of the R1 hodoscope elements started the TDC, the

intercept in eq. 5.2 can vary by 2 nanoseconds. Eq. 5.2 is for R1A starts.

Figure 19 shows a scatter plot of front momentum versus t_f for a low forward momentum coincidence run. The proton and positive pion lines are evident. Real times were also calculated for front arm events using momentum, mass, and the path length between F0 and F3. Again a linear function was found relating the real time in nanoseconds T_f to the raw TDC counts t_f:

$$T_f = .053\ t_f - 4.45 \tag{5.3}$$

The real time thus extracted agrees well with the real time-of-flight of the front arm protons in the elastic scattering run when the p-p elastic t_f is substituted into eq. 5.3.

Using eqs. 5.2 and 5.3, β and γ can be calculated from raw TDC counts and inserted into eq. 5.1. The resulting mass distributions are shown for the front and rear arm simultaneously in figure 20, which is a scatter plot of front arm calculated mass versus rear arm calculated mass. This type of plot was used on-line and off-line to identify the coincidence events in which a proton was scattered into each arm. The widths of the proton, deuteron, and pion masses in the figure are due to finite momentum and time resolution. The contributions of each type of resolution can be found by taking the partial derivatives of eq. 5.1 with respect to time and momentum. Using standard error analysis, [14]

$$\sigma_m^{\,2} = \sigma_\delta^{\,2} m^2 + \sigma_t^{\,2} \left[\frac{pc}{d\gamma}\right]^2 (1 + \gamma^2\beta^2)^2 \qquad (5.4)$$

where σ_m is the instrumental mass width, m is the actual mass, σ_δ is the fractional momentum resolution as defined in eq. 4.10, σ_t is the real time resolution, p is the momentum, c is the speed of light, d is the path length, and γ and β are the Lorentz factors. From eq. 5.4, the known momentum resolution, and the widths of the proton peaks in the mass plot made from the p-p elastic data, one finds that $\sigma_t \simeq 0.6$ nsec. Note that for a given particle of exact mass m, the first term in eq. 5.4 is a constant while the second term grows with increasing momentum. Therefore at high momenta, the large widths of mass distributions are primarily associated with the uncertainty in the measurement of time. The uncertainty in the measurement of time is mainly responsible for the spread in mass measurement. It was found that the proton mass peak becomes very wide and extends below the pion mass for momenta greater than 1350 MeV/c in the front arm. In fact, one must include in the data particles with apparent $\beta>1$. When the proton mass width becomes so large that it encompasses masses of other particles, contamination to the front arm proton spectra from pions and deuterons must be considered. The effect of this contamination will be presented with the data in chapter 7.

2. Real and Random Coincidences

Random, analyzable coincidences arise primarily from real particles in each arm which did not originate from the same beam particle, but which satisfied the 40 nsec R·F timing gate. To separate the

real from the random signal, one must trace time back to the target to ensure that both particles originated simultaneously.

The following scheme was developed for on-line and off-line analysis: Let $t_{a,b} \equiv t_b - t_a$ where t_a is the real time inferred from the TDC which is stopped when a signal is present at location a. t_b is defined similarly. Also let $d_{a,b}$ be the distance between points a and b. If the particle loses negligible energy in the system,

$$\frac{t_{R1,R3}}{d_{R1,R3}} = \frac{t_{tgt,R1}}{d_{tgt,R1}} \tag{5.5}$$

where tgt refers to the target location. Similarly for the front arm

$$\frac{t_{F0,F3}}{d_{F0,F3}} = \frac{t'_{tgt,F0}}{d_{tgt,F0}} \tag{5.6}$$

where it is allowed that for a random coincidence t'_{tgt} of eq. 5.6 may not be equal to t_{tgt} contained in eq. 5.5. With the above two equations, the quantity $\delta t \equiv t'_{tgt,F0} - t_{tgt,R1}$ can be calculated using the experimentally inferred real times T_r and T_f described in the last section. To correlate the rear and front arm in time, recall that the F0 TDC was started by an R1 hit. After calibration, this TDC gives $t_{F0} - t_{R1} \equiv \delta t_{exp}$. Note that

$$\begin{aligned} t_{a,b} &= -t_{b,a} \\ t_{a,b} + t_{b,c} &= t_{a,c} \end{aligned} \tag{5.7}$$

If the particle in the rear arm originated at the target at the same time as the particle in the front arm then $t_{tgt} = t'_{tgt}$ and there is a real coincidence. From equations 5.5, 5.6, and 5.7, one finds that the condition for a real coincidence can be expressed as $\delta t_{exp} = \delta t$.

The quantity TDIF $\equiv \delta t_{exp} - \delta t$ was histogramed on-line, and a spectrum from one of the proton-proton elastic scattering runs is shown in figure 21a. There is an obvious real peak at TDIF $\simeq 0$ of half width 2 nanoseconds, and there is very little background outside of the peak. In contrast, figure 21b shows a TDIF spectrum from one of the (p,2p) data taking runs at high momentum transfer listed in table 1 of chapter 3. This spectrum also shows a 2 nanosecond wide peak near zero, but, because the real signal is so much weaker than that of the elastic scattering case, there is a sizable background. For all calculated coincidence cross sections, a cut was made on the real peak, and the random contribution to the cross section was subtacted off. The real peak to random background ratio varied from 10:1 to 6:1.

3. Calibrations

The proton-proton elastic cross section was measured at 1.05 GeV incident energy to calibrate TASS with respect to counter positions, magnetic field, and normalization. Coincidence measurements were taken at three values of momentum transfer, and a singles measurement using the front arm only was taken for one value of momentum transfer. The elastic signal measured in the coincidence mode is the most stringent test of the accuracy and efficiency of TASS. For a given angle of one arm, planar elastic kinematics completely determines the momentum of the particle in that arm and the complete momentum vector of the particle in the other arm. The first step in

analyzing the coincidence elastic data was to note from the survey that the angular placements of both arms were correct to 0.2°. Central momentum corrections on the order of +2% were then made to the wire orbit values using elastic scattering kinematics.

Cross sections were calculated by first considering a momentum bite in the rear arm. The acceptance ΔP_r for proton-proton elastic scattering follows from an equation similar to eq. 4.14:

$$\Delta P_b = \int_{bite} dP_b \; T(P_b, \Omega_b(P_b), P_f(P_b), \Omega_f(P_b)) \tag{5.8}$$

where the rear solid angle Ω_b, the front solid angle Ω_f, and the front momentum magnitude P_f are explicitly written as functions of the rear arm momentum P_b. The functional relationship is given by solving the elastic kinematic equations

$$\begin{aligned} \vec{P}_{inc} &= \vec{P}_b + \vec{P}_f \\ E_{inc} + m_p &= E_b + E_f \end{aligned} \tag{5.9}$$

where $(E_{inc}, \vec{P}_{inc})$ is the incident proton's four-momentum, m_p is the proton mass, E_b is the rear proton's energy, and E_f is the forward proton's energy. In principle one could use the T functions calculated as in appendix B to do the integral of eq. 5.8. It was found, however, that a Monte Carlo procedure is more convenient because it easily introduces the effects of finite resolution, multiple coulomb scattering, and energy loss to the resolution and the acceptance.

These effects are important corrections to the analytic acceptance calculation for elastic scattering because the actual momentum range spanned by the proton yield in the rear arm is a small number

of resolution widths. Because of the kinematic constraints for proton-proton elastic scattering and the geometry of TASS, the actual yield of backward protons in the rear arm can be shown by computer simulation to span a range of about 40 MeV/c. The effect of finite resolution due to the discreet geometry of the counters of TASS is to smear the apparent yield as measured by the spectrometer over a range wider than 40 MeV/c. Thus for a given measured backward momentum cut, one must calculate the fraction of events that were smeared out of the experimental bite. If the yield smoothly spanned a larger momentum range, as is the case for all other spectra measured, then the events smeared out of neighboring momentum bins into the bite considered would compensate for those events lost from the momentum cut of interest. Since multiple scattering broadens the finite resolution by changing a particle's trajectory from what it would be in vacuum, it must also be considered. The corrections to the analytic acceptance imposed by multiple scattering and geometrical finite resolution were about 50%, 10% of which arose from the finite geometrical resolution effect alone.

Once ΔP_r is calculated, one can compute $\frac{d\sigma}{dP_b}$ for the spectrometer by normalizing to the target density and the ion chamber, which is weighted by the computer live time as described in chapter 4. This cross section must be multiplied by 2π divided by the azimuthal angular bite of the spectrometer. Then $\frac{d\sigma}{d\Omega_{cm}}$ can be calculated where Ω_{cm} is the center-of-mass solid angle. One must use the fact that

$$\frac{E_b}{2m_p P_b} \frac{d\sigma}{dP_b} = \frac{\pi}{P_{cm}^2} \frac{d\sigma}{d\Omega_{cm}} \tag{5.10}$$

where P_{cm} is the center-of-mass momentum. A CH_2 target was used for the coincidence as well as the singles running, and a carbon target was used for subtraction. The carbon subtraction was important only for the singles run.

Figure 22 shows the elastic cross sections as a function of center-of-mass solid angle. The coincidence cross sections are the three circles, and the singles data point is the triangle. The filled circles are the data of Dowell et. al. [15] and the open circles are data of Ryan et. al. [16] Acceptance calculations for the front arm singles elastic cross section were identical to those for the coincidence run, if one substitutes a forward momentum bite for the rear bite of equations 5.8 and 5.10. The error bars shown in figure 22 for this experiment are statistical only. Of the two trigger modes, systematic errors are much larger for the coincidence runs since the effect of the over constrained coincidence kinematics coupled with the acceptance makes the yield of the coincidence mode vary more quickly with counter location and angular spectrometer placement than that of the singles mode. For the coincidence runs the systematic errors due to angular magnet placement were about 13%, and those due to individual counter positions were about 10%. Thus the total systematic error due to spectrometer geometry and placement was about $\pm$16%. The total systematic error for the front arm singles cross section was $\pm$5%.

There are three other sources of systematic error applicable to all cross sections. The most important one arises from the normalization of the ion chamber to calibrate the beam intensity. This calibration was done using the ^{11}C activation technique.[17] The overall accuracy of this method was determined by comparing successive calibration measurements done with the same ion chamber and beam conditions. This procedure gave a systematic error of $\pm 8\%$ due to ion chamber calibration. Target densities were measured to $\pm 1\%$, and nuclear absorption introduced an additional error of $\pm 1.5\%$ for singles measurements and $\pm 3\%$ for coincidence measurements. Thus the total systematic error which would affect the three E444H coincidence points of figure 22 in the same way is $\pm 18\%$. For the singles point, the systematic error is $\pm 10\%$. The calibration data from this experiment agree reasonably well with the other elastic scattering data of figure 22, but calibrations of reactions with less restrictive kinematics would be useful for TASS.

In addition to elastic scattering which tests the complete coincidence system, rear arm singles spectra were taken at 120°. The reaction 2.1 GeV $p + {}^{12}C \rightarrow p(120^{o}) + X$ was measured with TASS in the rear trigger mode. Cross sections were calculated with the analytic acceptance as described in chapter 4. Multiple scattering and finite resolution were not important. Energy loss had the effect mentioned in chapter 4, that being to shift the momentum scales by 2-3% at low momenta.

Rear singles are important to test our understanding of all the factors which go into the acceptance calculation, because central momenta were chosen for the singles running so that the acceptance of different runs would overlap. Figure 23a shows a rear singles spectrum composed of three different magnet central momentum settings, as labeled in the upper right corner. The acceptance function for each setting was taken to be a curve like that of figure 17a, which was calculated with the beam and counter positions as determined by a survey. The discontinuities at the overlap points of the runs are as high as 30%. To find the source of the discontinuities, errors in the following quantities were considered: 1) the magnet central momentum, 2) the spatial shape of the magnetic field, 3) the position of counters relative to each other, and 4) the position of the beam spot relative to the rear arm coordinate system. The elastic scattering and wire orbit data seem to rule out the first and second possibilities. Of the last two possibilities, the second is preferable because the carbon target used was at 60° to the beam and a small error in the relative horizontal position of the beam chamber and target is multiplied by $1/\cos 60^{\circ} = 2$. Actually one can combine possibilities 3 and 4 above by attributing the discontinuities in the momentum spectrum to an error in the relative position of the beam spot on the target and the R1 counter.

Figure 23b shows what happens to the momentum spectrum if the beam chamber location--and thus the beam spot location--is shifted by 2.5mm to the left looking downstream. Since all surveying was

assumed to be accurate to 1mm, the justification for this procedure is questionable. Nonetheless, the different runs match up reasonably well in figure 23b. The 90° and 110° data for 2.1 GeV p + $^{12}C \rightarrow p + X$ of Tanihata et. al. [18] was extrapolated to 120° to compare with our results and is shown on the same figure. The shape and normalization of our data are consistent with the the Tanihata points thus extrapolated.

The effect of this sort of correction to the 2.1 GeV coincidence data to be discussed in chapter 7 is to contribute to the systematic uncertainty. For that data set only one rear magnetic field setting was used per forward angle setting. The discrepancies in figure 23a affected only the low momentum part of the rear arm acceptance. Therefore in taking low backward momentum cuts for the forward coincidence spectra of chapter 7, a beam chamber position was used half way between that which produced figure 23a and that which produced figure 23b. The fractional systematic uncertainty due to the beam-counter relative position was taken to be one half the fractional difference between the cross sections of figure 23a and 23b. This gives a contribution to the systematic error of $\pm 15\%$ for low backward momenta, that is for momenta with $-.30 \leq \delta \leq -.15$ with δ as defined in chapter 4.

It is worth noting that the main conclusion of the coincidence and singles calibration runs is that the uncertainty in the positions of counters and the beam is the dominant contribution to systematic errors. When the fringes of the coincidence or singles acceptances

are being considered, a part of the beam only two to three millimeters wide is being used. For the 2.1 GeV run, the entire beam was only 3mm wide to insure the best possible resolution in the front arm. Therefore, to avoid these systematic errors, one must either measure positions to much better than one millimeter, or only use parts of the acceptance for which most of the beam is seen.

CHAPTER 6

Phase Space

As mentioned in chapters 2 and 3, this experiment was a kinematic search for the final states appropriate to proton-deuteron breakup reactions. In this chapter, the effects of phase space and Fermi momentum of the nuclear pair on the kinematics are discussed. The general methods for calculating many-body phase space distributions for targets with Fermi momentum are also discussed to facilitate the understanding of the experimental results of chapter 7.

The essential question of this type of research is: How many target particles participated in the reaction? It is assumed that kinematic considerations alone can largely answer this question. It was in this spirit that Komarov applied phase space considerations to his data of reference [8]. Of course the pure phase space model, which ignores dynamics imposed on reactions by the forces of nature, was first suggested by Fermi.[19] For the (p,2p) experiment, phase space simulations outline the kinematic regions which are populated by the final state appropriate to a nuclear pair interaction. More importantly, phase space considerations can demarcate the kinematic regions populated by processes other than the correlated pair interaction--processes which might involve particle production or large numbers of target, participant nucleons.

The phase space calculation is done by the Monte Carlo method in which one randomly chooses a set of numbers for the input parameters which comprise one event. Physically, an event consists of a proton of given four-momentum incident on a moving target, which produces a given number of final state particles. Each phase space event generated has three ingredients: 1) The kinematics of the reaction, 2) the statistical or phase space weight, and 3) the probability of finding a target within the nucleus of a given Fermi momentum. This calculation is a generalization of the three-body phase space work of Ruiz et. al. [20] in that it accommodates many-body final states and target Fermi momentum. The calculation discussed here is also different from that of reference [20] in that all computations are done in the lab frame to easily extract experimental observables.

First consider only three-body final state kinematics for each Monte Carlo'd event. In the calculation of the proton-target kinematics of chapter 3, there were five input parameters $\vec{P}_b$, Θ_f, and ϕ_f. If the target is moving with four-momentum $(E_{fe},\vec{P}_{fe})$ as in appendix A, the three-momentum $\vec{P}_{fe}$ constitutes three more parameters. Since one would eventually like to calculate differential spectra with respect to P_f, the forward going proton's momentum magnitude, it is not considered as a quantity to be solved for as in appendix A, but rather it is thought of as an input parameter. To completely specify the kinematics with a moving target, two more input parameters are needed and are chosen to be Θ_{fe} and ϕ_{fe}, the angular coordinates of the target Fermi momentum. One could have equivalently

chosen one angular coordinate of the Fermi momentum and the Fermi momentum magnitude as the remaining two input parameters. To summarize, there are eight input parameters which we choose as $(\vec{P}_b, \vec{P}_f, \theta_{fe}, \phi_{fe})$. Doing algebraic manipulations similar to those of appendix A, $\vec{P}_u$, the unobserved nucleon's momentum, and P_{fe} are solved for and the kinematics for each event are determined.

The total phase space $R_3(\underline{P}, \underline{P}_{fe})$ of the three-body final state can be written as[21]

$$R_3(\underline{P}, \underline{P}_{fe}) = \int \frac{d^3P_b}{2E_b} \frac{d^3P_f}{2E_f} \frac{d^3P_u}{2E_u} \; \delta^4(\underline{P} + \underline{P}_{fe} - \underline{P}_f - \underline{P}_b - \underline{P}_u) \tag{6.1}$$

where the line underneath a symbol indicates a four-vector. $\underline{P}$ is the incident proton's four-momentum, $\underline{P}_{fe}$ is the four-momentum of the participating part of the nucleus, and all other symbols are as in appendix A. The weight functions are the standard phase space weights $d^4P_i \; \delta(P_i^{\,2} - m_i^{\,2})$ for a particle of four-momentum $\underline{P}_i$ and mass m_i.

The next step is to add the Fermi momentum probabilities. The probability density for finding a fragment in the nucleus with momentum $\vec{P}_{fe}$ is taken to be that described by Goldhaber in reference [7] in his analysis of fragmentation data.[22] This density is given as in chapter 2 by

$$\begin{aligned} W(\vec{P}_{fe}) &\propto e^{-(P_{fe}^2/2\sigma_{fe}^2)} \\ \sigma_{fe}^{\;2} &= \frac{F(A - F)\sigma_0^{\;2}}{A - 1} \end{aligned} \tag{6.2}$$

where A is the atomic number of the nucleus, and F is the number of nucleons in the participating target fragment. As in chapter 2, σ_0 = 90 MeV/c. With Fermi momentum, eq. 6.1 generalizes to

$$R_3(\underline{P})=\int\frac{d^3P_b}{2E_b}\frac{d^3P_f}{2E_f}\frac{d^3P_u}{2E_u}e^{-(P_{fe}^2/2\sigma_{fe}^2)}d^3P_{fe}\,\delta^4(\underline{P}+\underline{P}_{fe}-\underline{P}_b-\underline{P}_f-\underline{P}_u) \quad (6.3a)$$

One could alternatively arrive at eq. 6.3a by considering the actual four-body final state resulting from the interaction of figure 2. This final state consists of three nucleons and the residual A-2 nucleus in its ground state. Labeling the four-body phase space with a prime,

$$R'_4(\underline{P}) = \int \frac{d^3P_b}{2E_b}\frac{d^3P_f}{2E_f}\frac{d^3P_u}{2E_u}\frac{d^3P_{A-2}}{2E_{A-2}}e^{-(P_{A-2}{}^2/2\sigma_{fe}{}^2)}\,\delta^4(\underline{P}+\underline{P}_A-\underline{P}_f-\underline{P}_b-\underline{P}_u-\underline{P}_{A-2})$$

where $\underline{P}_A$ and $\underline{P}_{A-2}$ are the four-vectors of the A-nucleon target nucleus and the A-2 nucleon spectator. The subscript of a primed phase space refers to the number of particles in the final state including the A-2 residual nucleus, whereas the subscript on an unprimed phase space refers to only the three final state particles in the proton-pair interaction. The non-invariant exponential is the probability that the A-2 residual and the pair center of mass have relative momentum $\vec{P}_{A-2}$. From eq. 2.2 $\underline{P}_A = \underline{P}_{fe} + \underline{P}_{A-2}$ as they are defined in this chapter. Similarly, apart from a sign, $d^3P_{A-2} = d^3P_{fe}$. The four-body phase space becomes,

$$R'_4(\underline{P})=\int \frac{d^3P_b}{2E_b}\frac{d^3P_f}{2E_f}\frac{d^3P_u}{2E_u}\frac{d^3P_{fe}}{2E_{A-2}}e^{-(P_{fe}^2/2\sigma_{fe}^2)}\,\delta^4(\underline{P}+\underline{P}_{fe}-\underline{P}_f-\underline{P}_b-\underline{P}_u) \quad (6.3b)$$

Apart from the factor of E_{A-2} in the denominator, eq. 6.3a and 6.3b

are equivalent. However, the difference between E_{A-2} and the mass M_{A-2} is very small. For the case where A=12 and P_{fe} = 400 MeV/c, the difference between the energy and mass of the A-2 nucleus is less than .1%. Thus eqs. 6.3a and 6.3b are different by only a constant factor and the small error in using the on-shell deuteron mass as discussed in chapter 2; therefore equations of the form of 6.3a will be used from here on.

To get eq. 6.3a into a useful form for the Monte Carlo procedure, first solve for $\vec{P}_u$ using the three-momentum part of the four dimensional delta function as follows

$$R_3(\underline{P}) = \int \frac{d^3P_b}{2E_b} \frac{d^3P_f}{2E_f} e^{-(P_{fe}^2/2\sigma_{fe}^2)} \frac{d^3P_{fe}}{2E_u^*} \delta(E + E_{fe} - E_b - E_f - E_u^*) \quad (6.4)$$

where a quantity with the star superscript means that it has been solved with the kinematic delta function, and is implicitly a function of all other unstarred quantities. As indicated above, we now solve for P_{fe} with the remaining delta function and find

$$R_3(\underline{P}) = \int \frac{d^3P_b}{2E_b} \frac{d^3P_f}{2E_f} P_{fe}^2 \frac{e^{-(P_{fe}^{*\,2}/2\sigma_{fe}^2)}}{2E_u^*} d\Omega_{fe} \; | D_3 | \quad (6.5)$$

where

$$D_3 = \left[\frac{P_{fe}^*}{E_{fe}^*} - \frac{P_{fe}^*}{E_u^*} - \frac{P\cos\theta_{fe}}{E_u^*} + \frac{P_f\cos\theta_{fe,f}}{E_u^*} + \frac{P_b\cos\theta_{fe,b}}{E_u^*} \right]^{-1}$$

where $\cos\theta_{a,b}$ is as in appendix A. The term D_3 results from using the delta function in E_{fe} of eq. 6.4 to solve for P_{fe} in the

integral.

The most convenient differential phase space form for comparing to experimental cross sections is

$$\frac{dR_3(\underline{P})}{dP_b d\underline{\Omega}_b \; dP_f d\underline{\Omega}_f} = \frac{(P_b P_f)^2}{8E_b E_f} \int \frac{P_{fe}^{*\,2}}{E_u^*} e^{-(P_{fe}^{*\,2}/2\sigma_{fe}^2)} \, d\underline{\Omega}_{fe} \, |D_3| \qquad (6.6)$$

Figure 24 is a plot of the differential phase space of eq. 6.6 versus front momentum for one set of experimental running conditions with $\theta_b = 120^o$, $\theta_f = 10.4^o$, and three selected ranges of backward momentum as noted. The value of σ_{fe} used was 120 MeV/c, which was calculated from eq. 6.2 using A=12 and F=2. The normalization for each backward momentum range is set so that the peak in the graph will be close to 1. One notices that, given the double root solutions of chapter 3, the high momentum root is favored. This is the result of the (P_f^2/E_f) term of eq. 6.6. Figure 24b shows with the solid lines what happens as $\sigma_{fe} \rightarrow 0$, and the double root solutions of figure 5 are recovered. The error bars on the phase space curves represent the statistics of the Monte Carlo process. The arrows on the figure correspond to QTBS kinematics and will be discussed in chapter 7.

Eq. 6.6 can be generalized to the situation where, either through particle production or the participation of large numbers of target nucleons, there is an N-body final state. As in appendix A, let

$$\vec{P}_u = \vec{P}_1 + \vec{P}_{u-1}$$
$$= \sum_{i=1}^{N-2} \vec{P}_i$$

where the sum is over all unobserved particles. The general phase space formula then becomes

$$\frac{dR_N(P)}{dP_b d\Omega_b \; dP_f d\Omega_f} = \frac{(P_b P_f)^2}{8E_b E_f} \int \frac{P_{fe}^{*\,2} \; e^{-(P_{fe}^{*\,2}/2\sigma_{fe}^2)}}{E_1^*} d\Omega_{fe} \prod_{i=2}^{N-2} \frac{d^3P_i}{2E_i} \; |D_N| \tag{6.7}$$

where

$$D_N = \left(\frac{P_{fe}^*}{E_{fe}^*} - \frac{P_{fe}^*}{E_1^*} - \frac{P\cos\theta_{fe}}{E_1^*} + \frac{P_f \cos\theta_{fe,f}}{E_1^*} + \frac{P_b \cos\theta_{fe,b}}{E_1^*} + \sum_{i=2}^{N-2} \frac{P_i \cos\theta_{fe,i}}{E_1^*} \right)^{-1}$$

and where the momentum of the particle labeled with subscript 1 is solved with the delta function. The three-momenta of the additional N-3 particles become additional input parameters in eq. 6.7. Thus for the general N-body final state, there are 3N-1 input parameters to the kinematics, because there are 3 degrees of freedom for each final state particle, plus 3 input parameters for the target with Fermi momentum, minus 4 kinematic equations of constraint. Operationally, one throws randomly over the input parameters which are not differentiated out of the integral and stores the weights given by the integrand of eq. 6.7 in the appropriate $(P_b, \Omega_b, P_f, \Omega_f)$ bin.

Figure 25 shows the differential phase space function of eq. 6.7 versus front momentum for final states with greater than three particles. The reaction simulated in figure 25a is 2.1 GeV $p+d \rightarrow p+p+n+\pi$

where the two protons are detected in TASS. The Fermi momentum of the deuteron is as in figure 24, and the rear momentum bite is $400 \leq P_b \leq 500$MeV/c. In figure 25b, the differential phase space function for the reaction 2.1 GeV $p+d \rightarrow p+p+n+\pi+\pi$ is plotted versus forward momentum. Normalization was again set to make the peak of each plot 1. Note that when pions are added to the final state, the populated phase space moves further away from high forward momentum. In figure 25c, the four-body final state for the reaction 2.1 GeV $p+t \rightarrow p+p+n+n$ is shown versus front momentum for the same backward momentum cut as in the figures 25a and 25b. The standard deviation of the Fermi momentum distribution of the triton inside the nucleus was taken as σ_{fe} = 120MeV/c. The phase space momentum distribution for the forward going proton is very broad in this case and overlaps the distributions of figures 25a and 25b. These illustrations will be useful in interpreting the data, but here they are only meant to show the trends of the front momentum spectra as backward momentum, final state particle number, and target nucleon number are varied.

CHAPTER 7

Results and Discussion

The goal of this experiment is to confirm or deny the possibility of interacting with a nuclear pair or small number of nucleons in a (p,2p) reaction at high momentum transfer. In this chapter, the data are presented and interpreted. The data taken at $\theta_f = 10.4^o$ seem to relate more to the above goal than the data taken at other forward angles, and they will be presented first, along with kinematic interpretations and the data's relationship to lower energy (p,2p) experiments. The data at $\theta_f = 45^o$ and the small amount of data taken at $\theta_f = 60^o$ will then be presented and discussed in section 2. Section 3 describes the atomic number dependence of the data as it was extracted from the copper running.

1. The (p,2p) Reaction at 10.4 Degrees

In this section the $\theta_f = 10.4^o$ data are discussed. The systematics of the forward momentum spectra are first outlined in section 1.1, and they are compared with the simulated response of TASS to various real spectra associated with the proton-carbon kinematic limit. The data are then compared to the proton-pair phase space and quasi-elastic kinematics in section 1.2. Section 1.2 also describes other (p,2p) experiments at lower energies.

1.1. Systematics of the Data and the Response of TASS

Figure 26 shows the six-fold differential cross section versus front momentum for the rear momentum cut $400 \leq P_b \leq 550$MeV/c. The backward angle is, as always, $\theta_b = 120^o$. This spectrum is subject to the $\pm 17\%$ systematic error for low backward momentum cuts due to the effects mentioned in chapter 5. As noted in section 1 of chapter 5, pions and deuterons can contaminate the proton sample in the front arm for momenta above 1350 MeV/c. To estimate the contamination to the (p,2p) signal from other forward going particles, the coincidence cross sections for protons backward and either pions or deuterons forward were calculated from the E444H data for forward momenta less than 1350 MeV/c. Extrapolating the data to higher forward momenta showed that the combined contamination from pions and deuterons at high forward momentum was less than 5% for all the data presented in this chapter.

The forward momentum spectrum for the 10.4 degree coincidence data is largely flat, or perhaps slightly falling from an average value of about 3.5 mb/(GeV/c-sr)^2 at 500 MeV/c to an average value of 2.8 mb/(GeV/c-sr)^2 at 1800 MeV/c. There is a possibly significant dip at about 2300 MeV/c followed by a few points at 3 mb/(GeV/c-sr)^2 and then an abrupt falloff at 2800 MeV/c.

Since the resolution of the front arm is as given in figure 16b, and the central momentum used for the high momentum part of the spectrum was 2151 MeV/c, it is worthwhile to discuss the response of the system to spectra which change abruptly with front momentum. In

particular, consider the kinematic limit in forward momentum for the reaction 2.1 GeV $p + {}^{12}C \rightarrow p + p + {}^{11}B$ for the average backward momentum represented in figure 26, P_b = 475MeV/c. The front momentum kinematic limit is found by solving equation A1 of appendix A with $\vec{P}_{fe} = 0$, E_{fe} = mass of the carbon nucleus, and $(E_u, \vec{P}_u)$ the four momentum vector of a recoiling boron nucleus in its ground state. The kinematic limit is found to be P_f = 2779 MeV/c.

One might argue that, ignoring the dip at 2300 MeV/c, the spectrum of figure 26 is consistent with being flat until abruptly falling off at the kinematic limit. Figure 27 shows the response of TASS to such a flat spectrum which falls at the forward momentum corresponding to the proton-carbon kinematic limit for a backward momentum of 475 MeV/c. The figure shows on the left the spectrum thrown at the apparatus in a Monte Carlo simulation. The flat part of the thrown points was normalized to an average value of the data of figure 26 between 1600 MeV/c and 2800 MeV/c. On the right figure 27 shows the cross sections which would be measured in the front arm of TASS with its finite resolution given the thrown distribution. Also on the right are the last few data points of figure 26 for reference. The solid line guides the eye through the Monte Carlo reconstructed points, and the dashed line guides the eye through the data. Note that the reconstructed spectrum on the right side of figure 27 falls off at about 2600 MeV/c, or about 180 MeV/c sooner than the flat spectrum thrown at the device. The reconstructed falloff is earlier because a given momentum bin is fed by momenta of roughly one

resolution's width on either side of the center of the bin. Thus the momentum bin at 2250 MeV/c, for example, is fed equally by low and high momenta within the resolution width. But a bin at 2600 MeV/c is fed less from high momenta since there is a sharp high momentum cut-off in the thrown yield.

We can now test the hypothesis that the spectrum of figure 26 represents a flat distribution up to the kinematic limit. The real data in figure 27 fall off at about 2800 MeV/c, 200 MeV/c higher than the reconstructed spectrum. If the systematic front momentum error were zero, the persistence of the high momentum part of figure 26 would imply that there must be an enhancement at high forward momentum to feed the momentum bins beyond the 2600 MeV/c cutoff of figure 27. A conservative estimate of the systematic front momentum error is $\pm 2\%$, gotten from the proton-proton elastic scattering calibration data. With this estimate, the real data of figure 27 still show significant rate in excess of the reconstructed cutoff. If the real spectrum fell off gradually toward the kinematic limit rather than abruptly as simulated, the reconstructed yield would start to decrease even sooner. Thus the reconstructed cross section of figure 27 represents an upper limit for the falloff point of the spectrum in the absence of a peak at the high momentum end. We can therefore conclude that the data are not consistent with a flat spectrum out to the kinematic limit. In fact, this analysis suggests that the dip at 2300 MeV/c and the subsequent rise and decrease of the spectrum of figure 26 could signify a peak at high forward momentum which may be

obscured by poor statistics and inadequate resolution.

Figure 28 shows the forward momentum spectrum with a higher backward momentum cut, $550 \leq P_b \leq 700$ MeV/c. The systematic error in cross section magnitude is $\pm 9.5\%$. The spectrum is perhaps level or slightly falling in the low forward momentum end. It levels off or rises slightly in the high momentum end and falls abruptly at about 2550 MeV/c. Again, one could say that the spectrum at the high end is essentially flat until it falls off at the kinematic limit of 2691 MeV/c, which corresponds to a backward momentum of 625 MeV/c. Figure 29 is the analog of figure 27 for the high rear momentum cut. Here the falloff point of the data and the reconstructed events are almost identical, implying that the real spectrum being fed to the forward arm of TASS in the experiment could be flat with an abrupt drop at the kinematic limit.

According to the "falloff point" analysis, one may draw the following conclusions: Whereas the forward momentum spectrum cut on high backward momentum is consistent with a flat spectrum up to the kinematic limit, the low momentum backward cut spectrum is not; in fact it seems to represent a peak at the high forward momentum end. If the systematic front momentum determination were for unknown reasons higher than 2%, one could still draw the weaker conclusion that the two spectra of figures 26 and 28 cannot both be consistent with flat cross sections out to their respective kinematic limits.

1.2. Interpretation of the 10.4 Degree Data

Assuming there is a peak at the high forward momentum end of the real cross section represented by figure 26, of what interest is it? Note from figure 24a and 24b that the proton-pair phase space exhibits a peak at high forward momentum. According to QTBS or the quasi-elastic picture, the incident proton interacts with one fast, backward going nucleon, and this model also predicts a peak in the forward momentum spectrum near the kinematic limit. The QTBS peak is near the kinematic limit because the incident nucleon is assumed to interact only with one target nucleon, leaving the residual nucleus in tact and close to its ground state. The arrows in figure 24 denote the kinematic limits for the midpoint of each backward momentum range shown. From figure 25, note that when pions are produced in an interaction with a two nucleon target, the populated phase space moves away from the high momentum end. Although not shown, this statement is also true when pions are produced in an interaction with a single-nucleon target. Also, when a nuclear target larger than two nucleons is struck and is broken up, as in figure 25c, the available phase space does not show a peak at the high forward momentum end. We are lead to the conclusion that only an interaction of the incident proton with one or two nucleons, in the absence of pion production, can produce a kinematic peak in the high forward momentum region, above 2500 MeV/c.

Is there a way to tell from the data whether the suggested high momentum peak in figure 26 corresponds to an interaction with one or

two nucleons? Given the closeness of the kinematic solutions for proton-pair and proton-nucleon interactions for low backward momentum as demonstrated in figure 26, it would be purely speculative to say which mechanism we observed, if one grants the existence of the high momentum peak at all. In addition, one could make plausible modifications to the proton-pair and QTBS pictures to make the two models' kinematic solutions even closer. For example, one could allow for an excited nuclear pair in the former, moving the proton-pair phase space toward higher forward momentum. In the latter, one could allow the residual nucleus to be excited, moving the kinematic limit solution toward lower forward momentum. Therefore, experimental momentum resolution is not the only problem in separating the kinematic signature for the two pictures.

Indeed, Frankel et. al. [23] recently performed a (p,2p) measurement at 800 MeV incident energy on lithium, with a very good resolution of 1.4% in their forward arm. They looked for an enhancement near the kinematic limit to test QTBS. Their results for the reaction 800MeV p + ^{6}Li $\rightarrow$ p(105°) + p(12.28^o) + X are plotted in figure 30. The backward momentum is 350 MeV/c. The dashed line represents the proton-pair phase space calculation of chapter 6 normalized to the Frankel data peak, with P_{fe} = 120 MeV/c. The arrow denotes the kinematic limit. Frankel's data are consistent with the kinematics of a single scattering, leaving the residual nucleus with a mean excitation energy of 18-20 MeV. Note however that there is a substantial overlap of the proton-pair kinematic solutions with his data

even with the excellent resolution of the spectrometer used.

Considering phase space shapes only, it seems impossible to experimentally separate QTBS from the pair mechanism near the kinematic limit, but an enhancement near that point is of interest regardless of the model invoked. Consider figure 7a of chapter 3 and the proton-pair interaction. To say that the phase space for the proton-pair interaction is enhanced at the high momentum end is equivalent to saying that pure phase space favors low momentum transfer to the unobserved nucleon. This strongly suggests the single scattering picture of figure 7a as opposed to the multiple scattering of figure 7b. If one allows that the mechanism of figure 7a contributes to a high momentum peak in the spectrum measured in figure 26, there is the ambiguity as to whether the backward nucleon was the participant--labeled without parentheses--or the spectator--labeled with parentheses. But the interest in this research is to find a very high momentum component in the nucleus. If the backward nucleon were the participant, then it is plausible that the momentum of the unobserved spectator largely represents the momentum of the nucleon in the nucleus before the interaction. One can calculate the unobserved nucleon's momentum to be about 570 MeV/c for the kinematic situation of figure 26. If the backward nucleon was the spectator, then the observed backward proton's average momentum of 475 MeV/c represents the high relative momentum component of the nuclear pair. It is because the spectator process gives a lower relative momentum for the pair that Yukawa and Furui[24] argue that the spectator pro-

cess must dominate the pair interaction.

The same arguments apply if the quasi-elastic model is considered. In that case, one can view the incident bottom line of figure 7a as the residual nucleus, part of which is somehow correlated via the solid line to the single, struck nucleon. If the participant is observed backward, one can calculate the A-1 spectator momentum, assumed to be the participant momentum before it was struck, to be 404 MeV/c for the kinematics of figure 26. If a spectator from the A-1 nucleons was ejected backward, we arrive again at a nuclear momentum of 475 MeV/c. Thus whether one uses the participant or spectator picture in either model, one arrives at a nuclear momentum above 400 MeV/c which is far beyond a typical Fermi momentum. The conclusion is that if the suggested enhancement in figure 26 can be shown to be statistically significant, model calculations, such as those outlined in appendix C, must assign probabilities for finding high relative or single nucleon momenta in the nucleus.

The certainty of this conclusion must be tempered by considering final state interactions in the single scattering process. Whether it is called distortion, as in the reference of Jacob and Maris,[25] or final state interactions, as in a recent theoretical treatment by Amado and Woloshyn,[26] the interacting particles of figure 7a when the bottom incident line is the A-1 residual nucleons negate the quasi-elastic interpretation of the last paragraph. With a final state interaction, one cannot kinematically reconstruct the momentum of the nucleon in the nucleus before the collision. Frankel

correctly states in reference [23] that the final state interaction of the primarily interacting nucleons with the A-1 residual nucleons must be coherent in order to preserve the appearance of quasi-elastic kinematics. In other words, the final state interaction or distortion must not breakup the A-1 nucleons, otherwise the resulting many-body phase space would no longer produce a peak at high forward momenta in the (p,2p) experiment. But since the mean free path of the initial and final state nucleons observed is on the order of the nuclear radius, there is a possibility that some fraction of the quasi-elastic events do emerge with information on the nuclear wave function. Of course, final state interactions can similarly distort the dynamics of the proton-pair interaction.

Certainly the magnitude of the "peak" in figure 26 of about 3 mb/(GeV/c-sr)^2 is a lower limit for the real magnitude of this enhancement. To demonstrate this fact, figure 31 shows the response of TASS to a flat peak in front momentum between the front momentum kinematic limits corresponding to the backward momentum cut of figure 26. These limits are $2738 \leq P_f \leq 2815$ MeV/c. To get an observed peak of 3 mb/(GeV/c-sr)^2, a real peak of 17 mb/(GeV/c-sr)^2 must be thrown at the apparatus. Frankel quotes 21.64 mb/(GeV/c-sr)^2 for the value of his peak shown in figure 30. Therefore, at the higher energy of E444H, there could be a peak of comparable magnitude.

Figure 28, the high backward momentum cut, is more difficult to interpret. One of the original motivations for this experiment was Komarov's observation of proton-deuteron kinematics at lower energies

from reference [8]. Whereas he observed a peak at the kinematics of proton-deuteron elastic scattering, corresponding to the midpoint of the contours of figure 5, we expect at the higher energies to observe proton-deuteron breakup kinematics, because the free elastic proton-deuteron cross section is down by at least an order of magnitude from the lower energy of 600 MeV,[27] and the deuteron breakup is therefore favored. For the high backward momentum cut of figure 28, the proton-pair and the quasi-elastic kinematics are well separated. Perhaps with improved statistics we could confirm the slightly rising trend of figure 28 toward the high momentum end. This would correspond to the proton-pair phase space of figures 24b and 24c. The problem, of course, is that the phase space for the configurations of figure 25a and 25c also contribute to the high momentum spectrum around 2300 MeV/c and then fall abruptly. An essential problem of the high energy (p,2p) experiment is that pion production and other mechanisms occupy similar kinematic regimes as the proton-pair mechanism when one moves away from the kinematic limit. Perhaps improved statistics and a model calculation which involved more than kinematic considerations could verify the contribution of the pair mechanism to figure 28.

It is useful to compare the coincidence front momentum spectrum to the singles spectrum at the same forward angle. The singles spectrum at 10° was measured by Tanihata et. al. [18] and is shown in figure 32. At the high momentum end, singles data taken from E444H are superimposed on the Tanihata spectrum to supplement the high

momentum end not measured by Tanihata. The singles data of E444H, labeled with triangles, are normalized to the Tanihata data, as the E444H data were taken during a recent run under conditions of poor beam location stability and thus is difficult to independently normalize. Note that the singles spectrum rises in the low momentum region as opposed to the coincidence spectrum. This argues against a thermal picture where the shape of the front coincidence spectrum is the same as that of the front singles spectrum; that is, the forward going proton is unaffected by triggering on a backward going proton. On the other hand, the shapes of figures 26 and 28 are similar up to the kinematic limit, suggesting that the mechanisms for the coincidence in the low front momentum region is insensitive to the range of backward momenta chosen. The 10.4^{o} singles data taken on TASS clearly show a quasi-elastic peak, which is expected at P_f = 2760 MeV/c from free proton-proton kinematics. If the possible coincidence peak of figure 26 is of the same width and relative strength as the singles quasi-elastic peak, then TASS in its present configuration is only in need of statistics to identify the existence, but not trace the shape, of the coincidence quasi-elastic peak.

Before leaving the 10.4^{o} data, I show in figure 33 the backward momentum spectra for the reaction 2.1 GeV p + $^{12}C \rightarrow$ $p(120^{o})$ + $p(10.4^{o})$ + X cut on the forward momentum ranges indicated. The striking feature is that the magnitudes and shapes of all forward momenta are roughly the same, except for the high momentum cut. This

again implies that for most of the coincidence spectrum, the momentum of the particle in the rear arm does not depend strongly on the momentum of the particle in the front arm. The inverted triangles in figure 33, which are the singles data of figure 23b normalized at the arrow to the coincidence data, further support this conclusion. The difference in magnitude and shape for the high momentum cut is certainly due in part to encountering the proton-carbon kinematic limit. Without knowing the precise shape of the high momentum forward spectrum, it is difficult to say whether the fast falloff of the high forward momentum cut is interesting beyond showing that TASS is sensitive to the trivial proton-carbon kinematic limit and is indeed capable of doing coincidence measurements. If, however, one considers that the spectrum of figure 33 is at least representative of the backward spectrum cut on the quasi-elastic peak, then one can assign a standard deviation for the Fermi momentum distribution needed to produce the shape of the high forward momentum cut of figure 33. This is done in appendix C.

The salient conclusions of the 10.4° data are: 1) The low backward momentum cut on the forward momentum spectrum suggests the presence of a peak near the kinematic limit. Whether this peak is due to proton-pair or proton-nucleon interactions, it would certainly result from an interaction with a small number of nucleons and indicates the possibility of measuring high momentum components with a (p,2p) experiment. 2) The high backward momentum cut on the forward momentum spectrum yields a result consistent with hitting the proton-

carbon kinematic limit, given our understanding of the systematic front momentum error. 3) Most of the forward or backward coincidence spectrum is insensitive to the momentum cut in the backward or forward arms respectively, showing that final state interactions or mechanisms with overlapping kinematic regimes make conclusions difficult away from the kinematic limit.

2. The (p,2p) Reaction at 45 and 60 Degrees

The coincidence cross section measured at $\theta_f = 45^o$ and at $\theta_f = 60^o$ cover front momenta very far from the kinematic limit. Therefore extracting information about interactions with small numbers of nucleons is perhaps plagued by some of the problems mentioned in the conclusions of the last section. Figure 34 shows the coincidence cross section for the reaction 2.1 GeV p + carbon $\rightarrow$ p(120°) + p(45°) + X for the two backward momentum cuts shown. The label "low field" means that the data were taken at a forward central momentum of 422 MeV/c, while the "high field" data were taken at a central momentum of 922 MeV/c. The low backward momentum cut spectrum is subject to 15% systematic error, and the high backward cut spectrum is subject to 9% systematic error.

The two backward momentum cuts of figure 34 show no statistically significant difference in shape, being flat or slightly rising up to about 500 MeV/c and then falling toward higher front momentum. For the various front momentum points in figure 28, the ratio of the cross sections of the lower backward momentum cut to those of the

high backward momentum cut is consistent with being a constant of about 1.75 ± 0.20. Plotted in figure 35 is the singles cross section from the Tanihata reference [18]. Both backward momentum cuts exhibit the same qualitative shape as the singles data, which suggests that because of multi particle cascades or final state interactions, their is little correlation between the forward and backward going proton.

The $\theta_f = 45^\circ$ point was chosen because it is at the edge of the egg-shaped contours of figure 5. Figures 36a and 36b show the effect of Fermi momentum and phase space weighting on the proton-pair kinematics of figure 5 for the conditions of each backward momentum cut of figure 34. There is no obvious similarity between the proton-pair phase space and the data of figure 34. Figure 36c shows the low backward momentum cut of figure 36a in the proton-pair interaction when one pion is added to the final state, but the peak in the phase space configuration is still too high in front momentum to correspond to the data of figure 34. Whereas the addition of a pion for the case $\theta_f = 10.4^\circ$ substantially separates the phase space of figure 25a from that of figure 24a, the addition of the pion for the $\theta_f = 45^\circ$ case does not qualitatively make figure 36c and 36a look very different from one another. Many other initial and final state configurations also give similarly shaped phase space distributions at this wide angle, which means it would be difficult to isolate any one mechanism unless it significantly dominated over all the others.

Figure 37 shows the coincidence cross sections at low forward momenta at $\theta_f = 60^o$, which is beyond the kinematic region accessible to free proton-pair scattering as shown in figure 5. The low forward momentum data at $\theta_f = 60^o$ show the same trend as that of $\theta_f = 45^o$. Again, the ratio of the low backward momentum points to the high backward momentum points for each forward momentum is consistent with a constant value; the value here is 2.3 ± 0.3. Because the 60° data are outside the free proton-pair kinematics, a substantial pair center-of-mass Fermi momentum is necessary to populate the kinematic region of the 60° data. Pure phase space predicts that the pair interaction cross section should be down by a factor of 6 from the 45° data because of the low probability of finding the required pair Fermi momenta. The similarity in shape and magnitude of the 60° data to that of the low forward momentum 45° data further discounts the possibility of kinematically identifying the proton-pair contribution to the $\theta_f = 45^o$ data.

If interactions with small numbers of fast nuclear constituents were an important contribution to the backward singles cross section, one would expect to observe quasi-elastic or proton-pair kinematic enhancements in the $\theta_f = 45^o$ data. One would also expect some response of the shape of the low and mid momentum regions of the 10.4^o spectra to changes in the rear momentum. Perhaps one reason why these features are not observed is that only a small amount of the available incident energy is carried away by the observed nucleons in the above-mentioned kinematic regions. If the nuclear

pair interaction, for example, were the first interaction the incident nucleon suffered, the unobserved spectator would go off with a momentum of 2 GeV/c for the kinematics of the 45° data. The unobserved nucleon then has enough kinetic energy to interact with the rest of the carbon nucleus again, perhaps obscuring the proton-pair phase space by adding more particles to the final state. Of course, the pure phase space may also be modified substantially by matrix elements for the elementary interactions, requiring a model calculation to uncover the correct description of the data. It is therefore difficult in the $\theta_f = 45^{o}$ data to confirm or deny the contribution of the proton-pair interaction. The apparently uncorrelated nature of the 45° and the low and mid forward momentum 10.4^{o} data suggests that if interactions with small parts of the nucleus do contribute to the (p,2p) signal, one must detect a large fraction of the available kinetic energy; this is to insure that the observed final state particles participated in the interaction of interest and not in subsequent interactions due to high momentum products left in the nucleus. One must either do more exclusive experiments to account for the incident energy in the observed particles, or stay near the kinematic limit as implied in section 1.

3. Atomic Number Dependence

A small amount of copper running was done at $\theta_f = 10.4^{o}$ spanning front and rear momentum ranges as in the second entry of table 1 on page 12. A parameterization of A^{α} is usually assumed where A is the

atomic number of the nucleus. Using carbon and copper, one finds $\alpha = 1.13 \pm .03$. At $\theta_f = 45^o$ a copper target was used for the backward and forward momentum ranges of the fourth and fifth entries of table 1. For the configuration of the fourth entry, $\alpha = 1.38 \pm .03$ and for the fifth entry $\alpha = 1.26 \pm .04$. In other (p,2p) experiments α has been found to be $0.39 \pm .07$ at 600 MeV [8] and near 1 at 800 MeV [31]. In comparing the various experiments, one must realize that A dependence can change with the choice of final state momentum vectors as well as with incident energy; therefore the A dependence of the different experiments may not be directly comparable.

The usual interpretation of the dependence of nuclear cross sections on A is geometrical. If A is less than 1, one assumes that some part of the nucleus, for example the surface or perimeter, is involved in the collision process. If $\alpha = 1$, each of the nucleons in the nucleus have an equal probability of interacting and a single scattering in anywhere in the nuclear volume is implied. Since combinations of A things taken two at a time goes as $A(A-1)$, $\alpha > 1$ is often associated with striking more than one nucleon in the nucleus. These interpretations are very simple and considerations such as final state interactions modify these descriptions.

CHAPTER 8

Conclusions

Although there is no evidence from this experiment which uniquely identifies the correlated pair interaction, there is at least the suggestion from the analysis of figure 26 in chapter 7 that a one or two nucleon interaction can produce an energetic nucleon in the backward direction. Kinematics alone may not be sufficient to tell if the fast nucleon responsible for the possible peak of figure 26 derives its high momentum from a single other nucleon, as in the nuclear pair picture, or from some larger combination of nucleons. As demonstrated, either a one or two nucleon interaction in the absence of final state interactions could require the existence of a high momentum nuclear constituent, revealing a very small but interesting part of the nuclear wave function. From the mean free path of the measured nucleons, it seems that the reaction products of at least some of the few-body interactions should emerge from the nucleus with negligible final state interactions.

At the time this thesis was completed, there were no models available which described a coincidence cross section for the energy regime covered. However, there is currently an attempt to apply to our data the cascade code of Cugnon,[28] which includes no abnormally high nuclear momenta. Fujita is also in the process of extending the model of Fujita and Hüfner,[29] used to calculate backward singles cross sections, to the calculation of coincidence cross sections for

the kinematics of this experiment.[30] The Fujita and Hüfner model uses a picture like that of figure 7a with final state interactions among the pair members.

One obvious improvement to this experiment would be to improve statistical accuracy. One could then verify whether the high momentum enhancement in figure 26 and the upward trend toward high momenta in figure 28 are statistically significant. As this thesis is in part an historical document, it should be noted that 100 hours were allotted by the Bevatron Program Advisory Committee for completing E444H more satisfactorily. But because of difficulties with accelerator operation during our last run, potential shortages in funds, and other political pressures, the 100 hours of data taking have been postponed--perhaps for just a few months, and perhaps for the more indefinite future.

In addition to statistics, better resolution in the forward arm would help to identify structure in the high forward momentum spectrum. Wire chambers for the front arm are under construction to replace the F1 and F2 hodoscope arrays. These chambers would make the resolution of the front arm comparable with that of the rear arm, but it is not certain whether the chambers will operate with the high fluxes in the front arm.

As stated in chapter 7, more exclusive experiments could help to isolate interactions with small numbers of nucleons at large momentum transfer, and possibly find a correlated pair signal. A more exclusive experiment would help limit the contribution of mechanisms

with phase space configurations overlapping those of the pair interaction. The problem of final state interactions would also be greatly remedied if more of the available incident energy could be detected in the final state particles. Tanihata et. al. [31] have done a more exclusive experiment at 800 MeV incident proton energy. Their experiment detected particles out of the reaction plane as well as protons and deuterons in the plane defined by the proton-pair kinematics. They report that the interaction of the incident protons with pairs of nucleons at their lower energy is an identifiable mechanism showing clear enhancements near proton-pair kinematics.

To summarize, this (p,2p) experiment, done at the highest momentum transfer to the backward particle measured to date, shows that this experimental method has promise for identifying high momentum components in the nucleus near the kinematic limit. This high momentum component could result from the relative motion of correlated pairs or from the motion of a single nucleon relative to the rest of the nucleus. But the results of this experiment give only a suggestion of the existence of the high momentum component; they are certainly in need of better statistics and perhaps better resolution to make a strong contribution to the understanding of the exciting subject of the high momentum component of the nuclear wave function.

APPENDIX A

General Tass Kinematics

Since there is one proton incident and two protons detected in the apparatus, the most general kinematics can be represented as follows:

$$\vec{P}_{inc}+\vec{P}_{fe}=\vec{P}_f+\vec{P}_b+\vec{P}_u$$
$$E_{inc}+E_{fe}=E_f+E_b+E_u \tag{A1}$$

where all symbols are as described in chapter 3, except the target deuteron is now replaced with an arbitrary target of momentum $\vec{P}_{fe}$ and energy E_{fe}. The unobserved four-vector $(E_u,\vec{P}_u)$ does not necessarily have the invariant mass of a nucleon. In practice, we assume that the four-vector $(E_{fe},\vec{P}_{fe})$ or its probability distribution is given as an input to the problem. It is also useful to separate out one of the unobserved objects and assign it a mass m_1. With the definitions

$$\vec{P}_u=\vec{P}_1+\vec{P}_{u-1} \qquad E_u=E_1+E_{u-1} \qquad m_1=(E_1^2-|\vec{P}_1|^2)^{1/2}$$

eq. (A1) can be written as

$$\vec{P}_{inc}+\vec{P}_{fe}-\vec{P}_f-\vec{P}_b-\vec{P}_{u-1}=\vec{P}_1$$
$$E_{inc}+E_{fe}-E_f-E_b-E_{u-1}=E_1 \tag{A2}$$

Given $(E_{u-1},\vec{P}_{u-1})$, usually specified by a phase space distribution, the problem can be solved for all remaining quantities. The following definitions are used:

$$\cos\theta_{a,b} = \cos\theta_a \cos\theta_b + \sin\theta_a \sin\theta_b (\cos(\phi_a - \phi_b))$$

$$\alpha = E_{inc} + E_{fe} - E_b - E_{u-1}$$

$$\beta = P_{inc}^2 + P_{fe}^2 + P_b^2 + P_{u-1}^2 + 2(P_{inc}P_{fe}\cos\theta_{inc,fe} - P_{inc}P_b\cos\theta_{inc,b} - P_{inc}P_{u-1}\cos\theta_{inc,u-1} - P_{fe}P_b\cos\theta_{fe,b} - P_{fe}P_{u-1}\cos\theta_{fe,u-1} + P_{u-1}P_b\cos\theta_{u-1,b} + m_1^2 - m_f^2 - \alpha^2$$

and $\gamma = 2(P_b\cos\theta_{f,b} + P_{u-1}\cos\theta_{u-1,f} - P_{fe}\cos\theta_{fe,f} - P_{inc}\cos\theta_{inc,f})$ with θ and ϕ the polar and azimuthal angles in the coordinate system in chapter 3. Squaring both equations in eq. (A2) and using the relation between m_1 and $(E_1, \vec{P}_1)$ yields

$$-(P_f^2 + m_f^2)^{1/2} = \frac{(\beta + P_f\gamma)}{2\alpha} \tag{A3}$$

Squaring eq. (A3) and using the quadratic formula to solve for P_f one obtains the result:

$$P_f = \frac{\dfrac{-\beta\gamma}{2\alpha^2} \pm \left[\dfrac{\beta^2 + \gamma^2 m_f^2}{\alpha^2} - 4m_f^2\right]^{1/2}}{2\left[\dfrac{\gamma^2}{4\alpha^2} - 1\right]} \tag{A4}$$

If $(E_{fe}, \vec{P}_{fe}) = (m_d, 0)$, $(E_{u-1}, \vec{P}_{u-1}) = (0,0)$, and m_1 = the nucleon mass, the double root solutions of eq. (A4) describe the egg-shaped contours of figure 5.

APPENDIX B

The Analytic Acceptance Calculation

The quantity $T(P,\Omega)$ of chapter 4 can be expressed as $T(\delta,\theta_x,\theta_z)$, where all spectrometer coordinates are as in chapter 4. Consider first a two dimensional system with $T(\delta,\theta_x)$ and a pencil beam source at the target. For a given y position, δ, θ_x, and the x position of a trajectory completely specify a ray through the system. The analytic calculation for a single arm goes as follows: For a given (δ,θ_x) pair, use two x-defining edges of a counter in the system to determine two rays. Trace these two rays back to the target as shown in figure B1a, using the homogeneous field transport of chapter 4 if the counter is behind the magnet. If the two points at the target encompass the beam, then T=1; if the point beam is outside of the region between the points of intersection of the two traced rays with the target, T=0. Figure B1b shows the next step. Instead of the pencil beam, use a Gaussian beam for the target spot. $T_x(\delta,\theta_x)$, the x transmission efficiency, is given by

$$T_x(\delta,\theta_x) = \frac{\int_{x_1}^{x_2} e^{-\frac{x^2}{2\sigma_x^2}}\,dx}{\int_{-\infty}^{\infty} e^{-\frac{x^2}{2\sigma_x^2}}\,dx} \qquad \text{(B1)}$$

where x_1 and x_2 are the target positions for the rays traced from

each of the two counter edges. This calculation must be repeated for each counter, and the most restrictive counter edges determine the acceptance.

The vertical transmission is done in the same way. In the square field model the vertical transmission is not coupled to δ, θ_x, or x. Therefore

$$T_z(\theta_z) = \frac{\int_{z_1}^{z_2} e^{-\frac{z^2}{2\sigma_z^2}} dz}{\int_{-\infty}^{\infty} e^{-\frac{z^2}{2\sigma_z^2}} dz} \tag{B2}$$

where z_1 and z_2 are the z positions on the target traced back from the most vertically restrictive counter edges at θ_z. Note that for an oblong spot $\sigma_x \neq \sigma_z$. For most of our 2.1 GeV running $\sigma_x < \sigma_z$. The total transmission for a given counter plane and beam spot is then given by

$$T(\delta,\theta_x,\theta_z) = T_x(\delta,\theta_x)\ T_z(\theta_z) \tag{B3}$$

APPENDIX C

Schematic Model Calculations

In this appendix, the ingredients of the quasi-elastic and pair interaction models are outlined in the absence of final state interactions (FSI). The quasi-elastic process is first examined to see if the high forward momentum cut backward coincidence spectrum of figure 33 warrants any abnormally high single-nucleon Fermi momentum components. From early work on the analysis of (p,2p) quasi-elastic processes [25] to the Frankel QTBS picture, [5] the quasi-elastic cross section has been written as the product of a phase space factor and a probability amplitude squared.

$$\frac{d\sigma}{(d\Omega dp)_b (d\Omega dp)_f} \propto \frac{P_b^{\,2} P_f^{\,2}}{E_b E_f E_{A-1}} \, |t_{fi}|^2 \, \delta(E_b + E_f + E_{A-1} - E_{inc} - M_A) \qquad \text{(C1)}$$

a where E_{inc} is the incident energy, M_A is the initial nucleus mass, M_{A-1} is the mass of the residual nucleus in the ground state, and E_{A-1} is its energy. The probability amplitude $|t_{fi}|^2$ is separated into two parts:

$$|t_{fi}|^2 \propto |t_{n,n}|^2 \, W(\vec{P}_{fe}) \qquad \text{(C2)}$$

where $|t_{n,n}|^2$ is the nucleon-nucleon interaction probability and is related to the free nucleon-nucleon differential cross section by $|t_{n,n}|^2 \propto s(s-4m^2) \left(\frac{d\sigma}{dt}\right)_{n,n}$, where s and t are the Mandelstam variables and m is the nucleon mass. The nucleon-nucleon interaction is taken to be the same as the proton-proton interaction. $W(\vec{P}_{fe})$ is the

single-particle momentum density given by

$$W(\vec{P}_{fe}) \propto e^{-P_{fe}^2/2\sigma_{fe}^2}$$

where σ_{fe} here is the standard deviation of the single-particle Fermi momentum distribution in the nucleus. As indicated by Jacob and Maris [25] and by Gurvitz [6], the choice of the values of s and t for the nucleon-nucleon interaction is ambiguous since the kinematics of the nucleon-nucleus interaction is different from the kinematics of the free nucleon-nucleon case. Regardless of the choice of the Mandelstam variables, however, the coincidence cross section is dominated by the $W(P_{fe})$ factor of equation C2.

Of the reasonable combinations of final state four-momenta, if one chooses s and t as follows:

$$\begin{aligned} s &= (\underline{P}_{inc} + \underline{P}_{fe})^2 \\ t &= (\underline{P}_{inc} - \underline{P}_{f})^2 \end{aligned} \qquad \text{(C3)}$$

where underlined quantities refer to four-vectors, the $|t_{n,n}|^2$ term gives the strongest contribution at high P_{fe} for the kinematics of the nucleon-nucleus scattering. These choices of s and t may not be unique or even preferred, but they will give a lower limit on the σ_{fe} needed for $W(\vec{P}_{fe})$ to reproduce the shape of the high forward momentum cut in figure 33. If one computes the cross section of equation C1, averaging over E_{A-1} to get rid of the δ function, one needs $\sigma_{fe} \simeq 180$MeV/c to reproduce the shape of the high forward momentum cut of figure 33. This is much larger than the 90 MeV/c obtained from fragmentation data. The large σ_{fe} indicates that in the absence of

FSI, an abnormally large Fermi momentum distribution would be required to explain the backward coincidence spectrum near the quasi-elastic peak.

For the single-scattering correlated pair picture, one begins with the phase space factor of equation 6.6. One then adds a nucleon-nucleon scattering probability for the wavy line of figure 7a and a deuteron relative momentum density for the solid line of figure 7a. With these ingredients, the cross section is

$$\frac{d\sigma}{(d\Omega dp)_b (d\Omega dp)_f} \propto \frac{(P_b P_f)^2}{8E_b E_f} \int \frac{P_{fe}^2}{E_u^*} e^{-P_{fe}^2/2\sigma^2} d\Omega_{fe} \, |D_3| \, |M|^2 \qquad \text{(C4)}$$

where all symbols are as in equation 6.6 except

$$|M|^2 = s(s-4m^2) \left(\frac{d\sigma}{dt}\right)_{n,n} |\Psi(\vec{q})|^2 \qquad \text{(C5)}$$

where s and t are the Mandelstam variables corresponding to the nucleon-nucleon vertex in figure 7a and $\Psi(\vec{q})$ is the momentum space wave function of a free deuteron with internal relative momentum $\vec{q}$. As mentioned in chapter 7, Yukawa and Furui [24] use an equation like C4 for the pair interaction, but they solve the kinematics with the complete nucleus as in eq. 6.3b. They find that the spectator process of figure 7a with parentheses dominates the single-scattering correlated pair interaction. In reference [24] the authors use a phenomenological internal pair wave function with high momentum components introduced by the hard core nucleon-nucleon interaction. As mentioned in chapter 8, Fujita and Hüfner [26] consider the diagram of figure 7a without parentheses, which means that the backward par-

ticle participated in the nucleon-nucleon scattering. Using an equation like C4 above, they find that a point-like interaction for the wave function $\Psi(\vec{q})$ fits backward singles data better than a Reid soft core deuteron wave function.

Thus for the nuclear pair interaction, both models mentioned above need higher momentum components than are found in ordinary deuteron wave functions to fit backward singles data. For the quasi-elastic picture, one also needs abnormally high single-nucleon momentum components to fit the shape of the backward coincidence data cut on what could possibly be a quasi-elastic peak.

References

[1] E. J. Moniz et. al., Phys. Rev. Lett. 26, 445 (1971).

[2] G. Landaud et. al., Nuclear Physics A173, 337 (1971).

[3] J. V. Geaga et. al., Phys. Rev. Lett. 45, 1993 (1980).

[4] J. R. Wu et. al., Phys. Rev. C 19, 698 (1979).

S. Frankel et. al., Phys. Rev. Lett. 36, 642 (1976).

A. M. Baldin, Joint Institute for Nuclear Research, Report JINR-P1-11302 (1978).

Y. D. Bayukov et. al., Phys. Rev. C 20, 764 (1979).

[5] S. Frankel, Phys. Rev. Lett. 38, 1338 (1977).

[6] S. A. Gurvitz, Phys. Rev. Lett. 47, 560 (1981).

[7] A. S. Goldhaber, Phys. Lett. 53B, 306 (1974).

[8] V. I. Komarov et. al., Nuclear Physics A326, 297 (1979).

[9] H. A. Enge, in Focusing of Charged Particles II, edited by A. Septier (Academic Press, New York, 1967), p. 203.

[10] E. Harvey, QDA-MULTI Data Acquisition, Real Time Systems Group, Lawrence Berkeley Laboratory (1981).

[11] D. Nelson, Magnetic Measurements Group Report MT 259, Lawrence Berkeley Laboratory (1977).

[12] C. Dols et. al., Magnetic Measurements Group Report MT 21A, Lawrence Berkeley Laboratory (1961).

[13] L. M. Taff et. al., Fermilab Multi User's Guide (1978).

[14] See for example P. R. Bevington, Data Reduction and Error Analysis for the Physical Sciences (McGraw-Hill, New York, 1969), p. 59.

[15] J. D. Dowell et. al., Il Nuovo Cimento 18, 818 (1960).

[16] B. A. Ryan et. al., Princeton-Penn Accelerator PPAR-11 (1969).

[17] J. V. Geaga et. al., submitted to Phys. Rev. C.

[18] I. Tanihata, private communication regarding 2.1 GeV singles data.

[19] E. Fermi, Progr. Theoret. Phys. 5, 570 (1950).

[20] C. L. Ruiz et. al., Nuclear Instruments and Methods 169, 199 (1980).

[21] See for example M. L. Perl, High Energy Hadron Physics (Wiley, New York, 1974), p. 169.

[22] F. Bieser et. al., Second Summer Study of Relativistic Heavy Ions, Lawrence Berkeley Laboratory (1974).

[23] S. Frankel et. al., Phys. Rev. C 24, 2684 (1981).

[24] T. Yukawa and S. Furui, Phys. Rev. C 20, 2316 (1979).

[25] G. Jacob and Th. A. J. Maris, Reviews of Modern Physics 38, 121 (1966).

[26] R. D. Amado and R. M. Woloshyn, Phys. Lett. 69B, 400 (1977).

[27] V. I. Komarov et. al., Soviet Journal of Nuclear Physics 16, 129 (1973).

[28] J. Cugnon et. al., "Pion Production in Central High Energy Nuclear Collisions," preprint from Universite de Liege, Institut de Physique au Sart Tilman, Batiment B.5, B-4000 LIEGE 1, Belgique (1981).

[29] T. Fujita and J. Hüfner, Nuclear Physics A314, 317 (1979).

[30] T. Fujita, private communication regarding coincidence cross section predictions.

[31] I. Tanihata, private communication regarding 800 MeV (p,2p) and (p,dp) data.

Figures

Fig. 1 Momentum density of protons produced at backward angles. The plot and some of the data are from reference [3]. Other data are from sources mentioned in reference [4] as noted in reference [3].

Fig. 2 Schematic representation of incident proton which will interact with only the pair of nucleons connected by the wavy line. The complete nucleus has A nucleons, and the A-2 nucleons are spectators.

Fig. 3 The single-particle momentum density--dashed line--normalized with peak equal to 1 at momentum = 0. The relative momentum density of pairs--solid line--as derived in equation 2.5, and normalized relative to the single-particle density.

Fig. 4 Planar proton-pair kinematics showing symbols used throughout paper. The subscripts inc, b, f, and u refer to the incident proton, the backward detected proton, the forward detected proton, and the undetected nucleon respectively.

Fig. 5 Plot of solutions for the 2.1 GeV proton-pair kinematics for $\theta_b = 120^\circ$. The contours are of constant backward momentum.

Fig. 6 Proton-pair kinematics for different values of the unobserved mass M. The solid line is the 400 MeV/c contour of figure 5 with M=938 MeV. The dotted and dashed lines are the same contour with M=1078 MeV and M=1232 MeV respectively.

Fig. 7a Possible proton-pair dynamics in a single-scattering picture. The line labeled P_{inc} represents the incident proton. The wavy line represents the nucleon-nucleon interaction and the solid line represents the nuclear pair interaction. The solid line can also be considered as correlating the struck nucleon and the A-1 other spectator nucleons in a pure quasi elastic picture. The outgoing particle going forward is labeled P_1, while the other exiting particles are labeled P_b and P_2 as described at the end of chapter 3.

Fig. 7b Possible proton-pair dynamics in a double scattering picture where there are two fundamental nucleon-nucleon interactions in addition to the nuclear pair interaction.

Fig. 8 Overview of TASS. Dimensions are given in table 2.

Fig. 9 Coordinate system used to calculate momenta and angles of particle trajectories.

Fig. 10 Data acquisition flow chart describing slow logic, fast logic, and computer interfacing.

Fig. 11 Fast logic diagram.

Fig. 12 Slow logic diagram.

Fig. 13 Computer accepted events versus events fed to computer. Dashed line is pulser generated. Solid line generated from photo tube noise.

Fig. 14 Flow chart for data acquisition subroutine.

Fig. 15a Test of homogeneous field model in rear arm. Comparison of wire orbit momenta as measured homogeneous field trajectories versus wire momenta measured by current in wire. δ refers to the fractional deviation from central momentum of the momentum as measured by the wire current. The errors shown are the standard deviation of the distribution of repeated measurements for the same δ.

Fig. 15b Test of homogeneous field model for front arm. Errors shown are as in figure 15a.

Fig. 16a Rear arm resolution in a square field as a function of deviation from central momentum.

Fig. 16b Front arm resolution in a square field as a function of deviation from central momentum.

Fig. 17a Rear arm percent angular acceptance as a function of deviation from central momentum.

Fig. 17b Front arm percent angular acceptance as a function of deviation from central momentum.

Fig. 18 Rear momentum versus raw TDC time-of-flight scatter plot.

Fig. 19 Front momentum versus raw TDC time-of-flight scatter plot.

Fig. 20 Front-rear mass scatter plot.

Fig. 21a Histogram of TDIF as defined in chapter 5 for proton-proton elastic run. Peak corresponds to particles in each arm which originated from the target at the same time.

Fig. 21b Histogram of TDIF for 2.1 GeV (p,2p) run.

Fig. 22 Proton-proton elastic scattering data from this experiment, from Dowell of reference [15], and from Ryan of reference [16].

Fig. 23a Uncorrected 2.1 GeV $p + {}^{12}C \rightarrow p(120^{o}) + X$ spectrum showing

discrepancies at overlapping central momenta.

Fig. 23b 2.1 GeV p + $^{12}C \rightarrow p(120^o) + X$ spectrum with 2.5mm shift of beam chamber to correct for discrepancies of fig. 23a.

Fig. 24a Differential proton-pair phase space versus front momentum for $400 \leq P_b \leq 500$ MeV/c. σ_{fe} = 120 MeV/c.

Fig. 24b Differential proton-pair phase space versus front momentum for $500 \leq P_b \leq 600$ MeV/c. σ_{fe} = 120 MeV/c. Solid lines show σ_{fe} = 5 MeV/c for the same backward momentum cut.

Fig. 24c Proton-pair phase space versus front momentum for $600 \leq P_b \leq 700$ MeV/c.

Fig. 25a Proton-pair phase space versus front momentum for $400 \leq P_b \leq 500$ MeV/c with pion in final state. σ_{fe} = 120 MeV/c.

Fig. 25b Differential proton-pair phase space versus front momentum for $400 \leq P_b \leq 500$ MeV/c with two pions in final state. σ_{fe} = 120 MeV/c.

Fig. 25c Differential proton-triplet (or triton) phase space versus front momentum for $400 \leq P_b \leq 500$ MeV/c with four nucleons in the final state. σ_{fe} for the triplet is 120 MeV/c.

Fig. 26 Plot of the coincidence spectrum for the reaction 2.1 GeV p + $^{12}C \rightarrow p(120^o) + p(10.4^o) + X$ versus front momentum for $400 \leq P_b \leq 550$ MeV/c.

Fig. 27 Response of front arm of TASS to flat spectrum out to p-carbon kinematic limit for P_b = 475 MeV/c, which corresponds to P_f = 2779 MeV/c. The solid line on the right guides the eye through the Monte Carlo response falloff, and the dashed line guides the eye through the falloff of the data.

Fig. 28 Plot of the coincidence spectrum for the reaction 2.1 GeV p + $^{12}C \rightarrow p(120^o) + p(10.4^o) + X$ versus front momentum for $550 \leq P_b \leq 700$ MeV/c.

Fig. 29 Response of front arm of TASS to flat spectrum out to p-carbon kinematic limit for P_b = 625 MeV/c, which corresponds to P_f = 2691 MeV/c. The solid line on the right guides the eye through the Monte Carlo response falloff, and the dashed line guides the eye through the falloff of the data.

Fig. 30 Comparison of 800 MeV Frankel data of reference [23] to proton-pair phase space of chapter 6 with σ_{fe} = 120MeV/c. The reaction is 800 MeV p + $^6Li \rightarrow p(105^o) + p(12.28^o) + X$ for P_b = 350 MeV/c.

Fig. 31 Response of the front arm of TASS to rectangular peak of

height 17 extending from 2738 MeV/c to 2815 MeV/c in front momentum, which corresponds to the p-carbon kinematic limit for the backward momentum range $400 \leq P_b \leq 550$ MeV/c.

Fig. 32 Front arm singles spectrum for the reaction 2.1 GeV p + $^{12}C \rightarrow p(10.4^o)$ + X from reference [18]. Triangles are E444H data normalized to reference [18] between 1600 and 1700 MeV/c.

Fig. 33 Plot of the coincidence spectrum for the reaction 2.1 GeV p + $^{12}C \rightarrow p(120^o) + p(10.4^o)$ + X versus rear momentum for the forward momentum cuts listed.

Fig. 34 Plot of the coincidence spectrum for the reaction 2.1 GeV p + $^{12}C \rightarrow p(120^o) + p(45^o)$ + X versus front momentum for the back momentum cuts listed. Low field and high field refer to different magnetic field settings of the forward arm.

Fig. 35 Singles cross section for the reaction 2.1 GeV p + $^{12}C \rightarrow p(45^o)$ + X interpolated from Tanihata et. al. reference [18].

Fig. 36a,b,c Differential phase space versus front momentum for reactions with $\theta_f = 45^o$. Reactions and backward momentum cuts as noted.

Fig. 37 Coincidence cross sections for low forward momentum and backward momentum cuts as noted. The reaction is 2.1 GeV p + $^{12}C \rightarrow p(120^o) + p(60^o)$ + X

Fig. B1a Illustration of two rays traced from counter plane for a given δ and θ_x combination. The dashed line is a ray which encompasses the pencil beam and therefore has transmission fraction = 1. The solid line misses the pencil beam and therefore has transmission fraction = 0.

Fig. B1b Illustration of ray traced back from counter plane to intercept Gaussian beam at target. Here the transmission factor is between 0 and 1 since the rays encompass part of the finite width Gaussian beam.

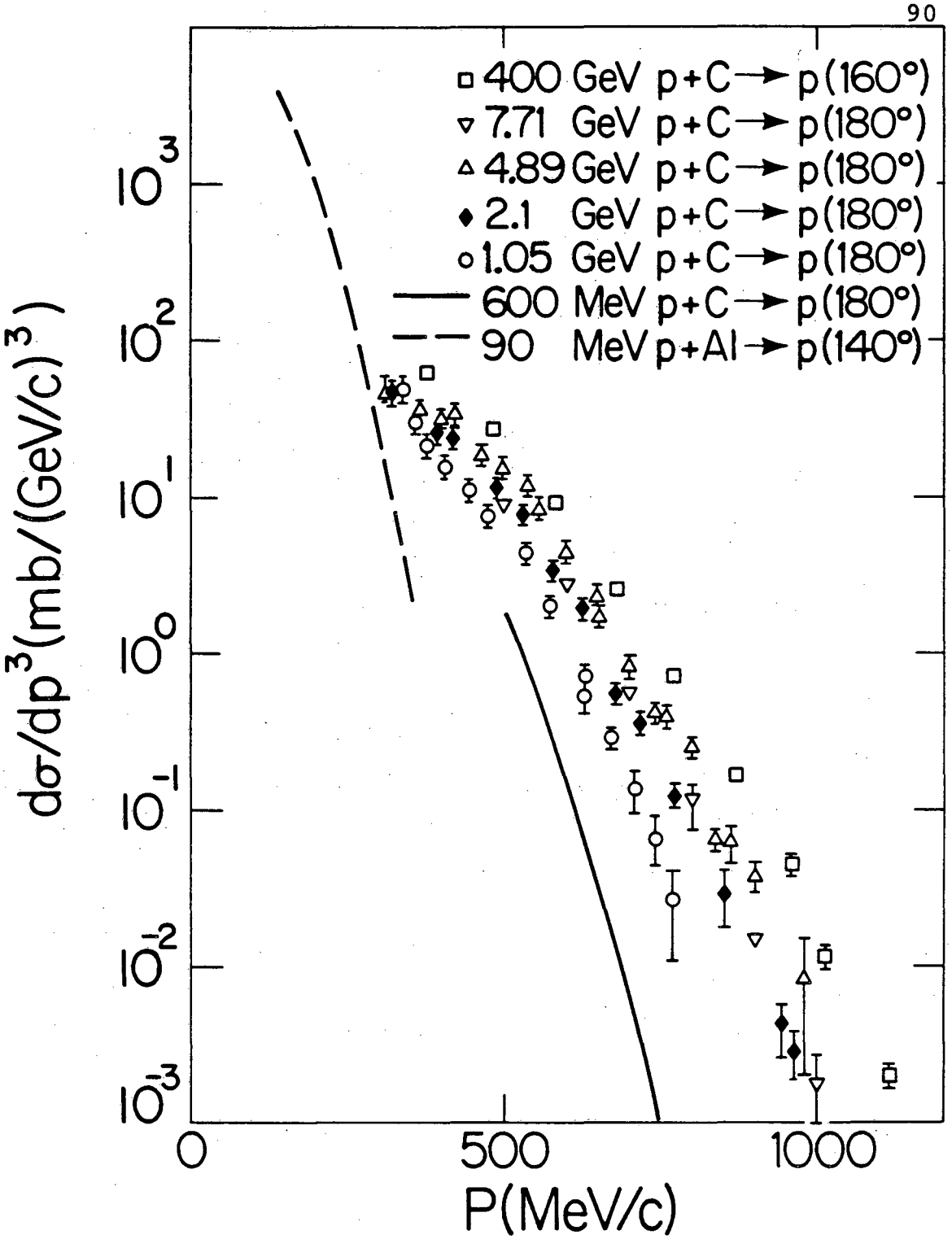

XBL 7912-13375

Fig. 1

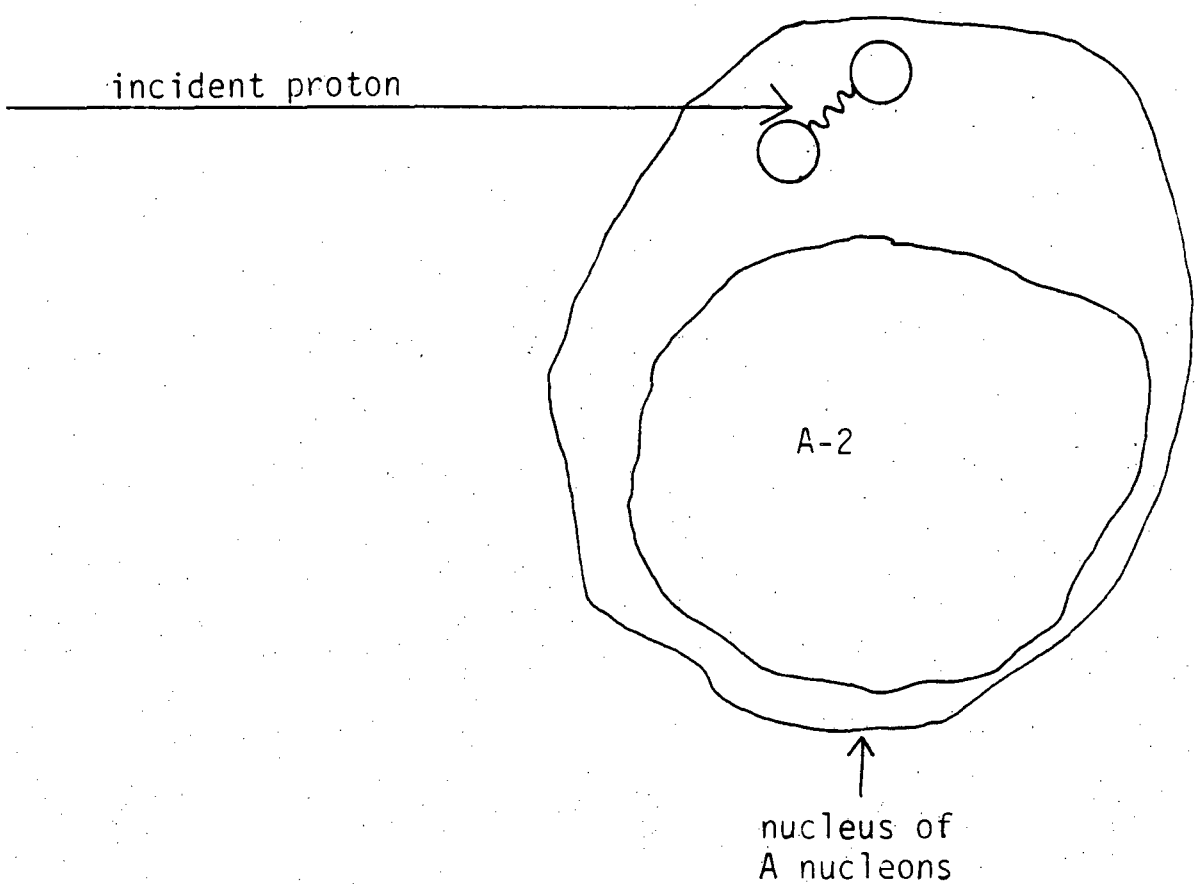

XBL 825-10118

Fig. 2

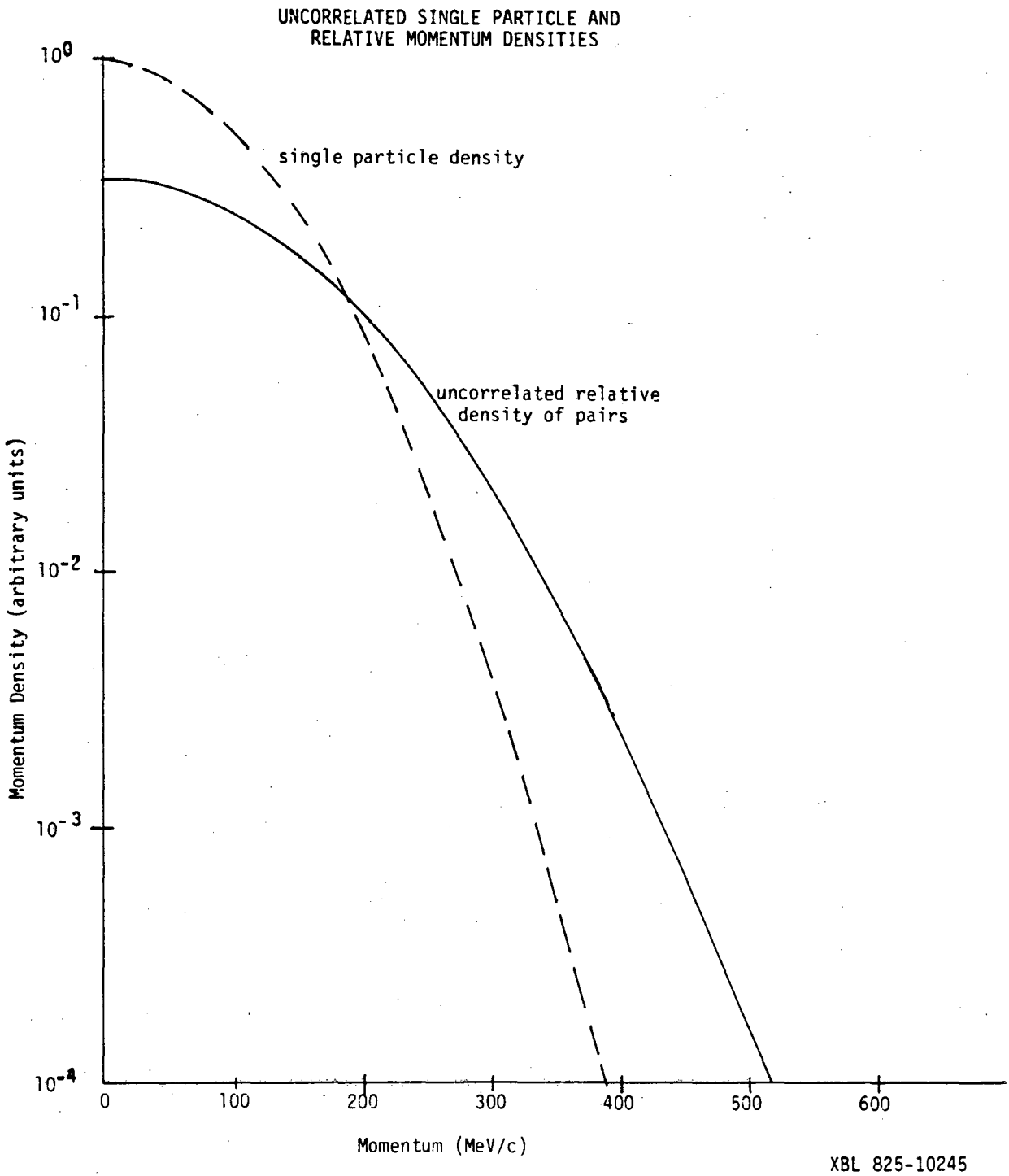
UNCORRELATED SINGLE PARTICLE AND
RELATIVE MOMENTUM DENSITIES
single particle density
uncorrelated relative
density of pairs
Momentum Density (arbitrary units)
10^0
10^{-1}
10^{-2}
10^{-3}
10^{-4}
0
100
200
300
400
500
600
Momentum (MeV/c)
XBL 825-10245

Fig. 3

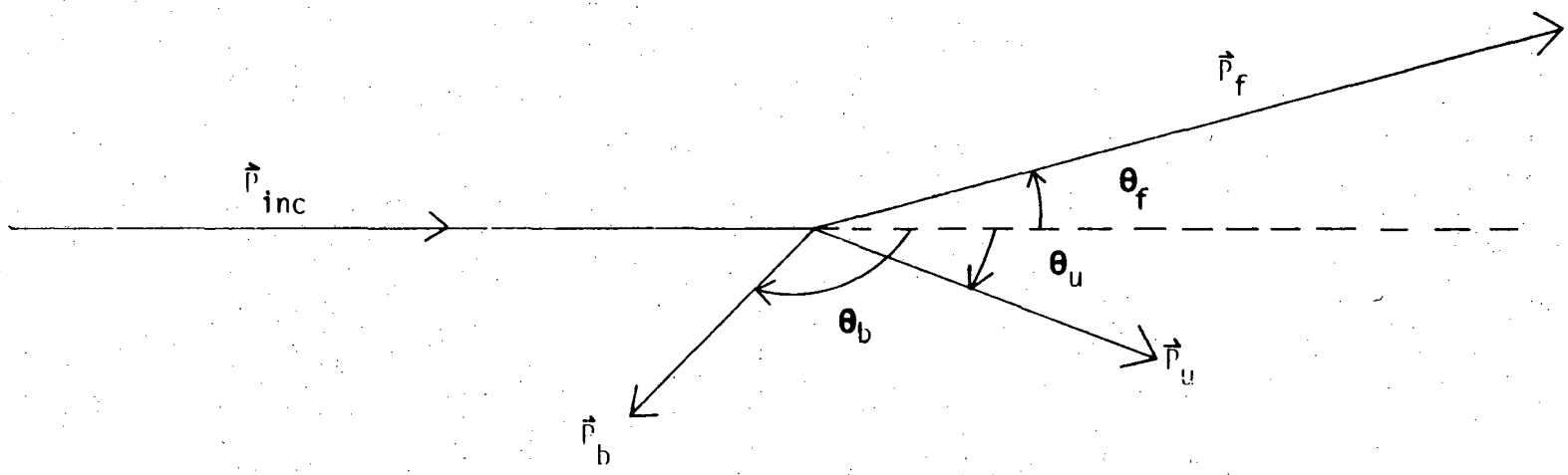

XBL 825-10112

Fig. 4

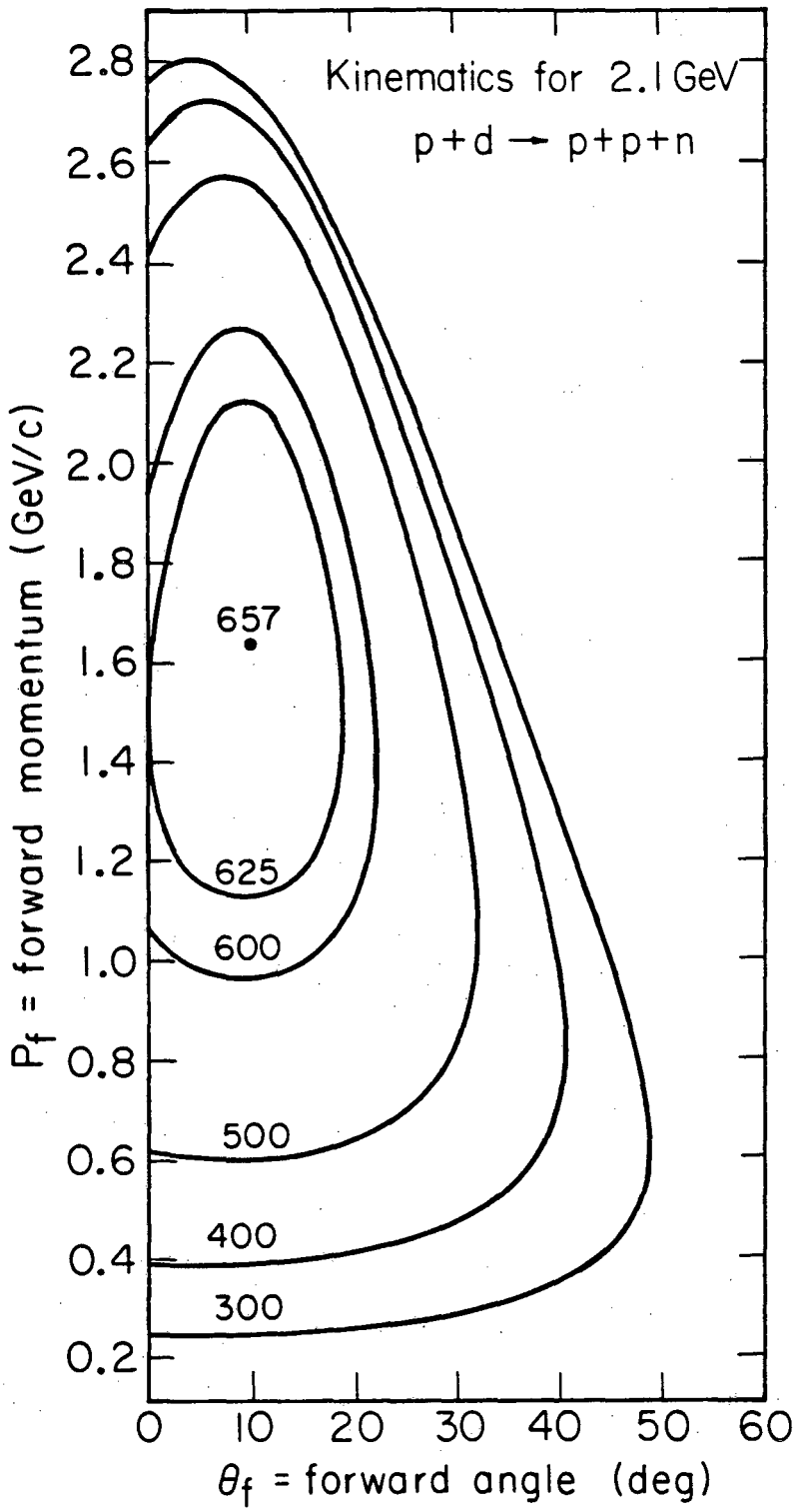

XBL824-3792

Fig. 5

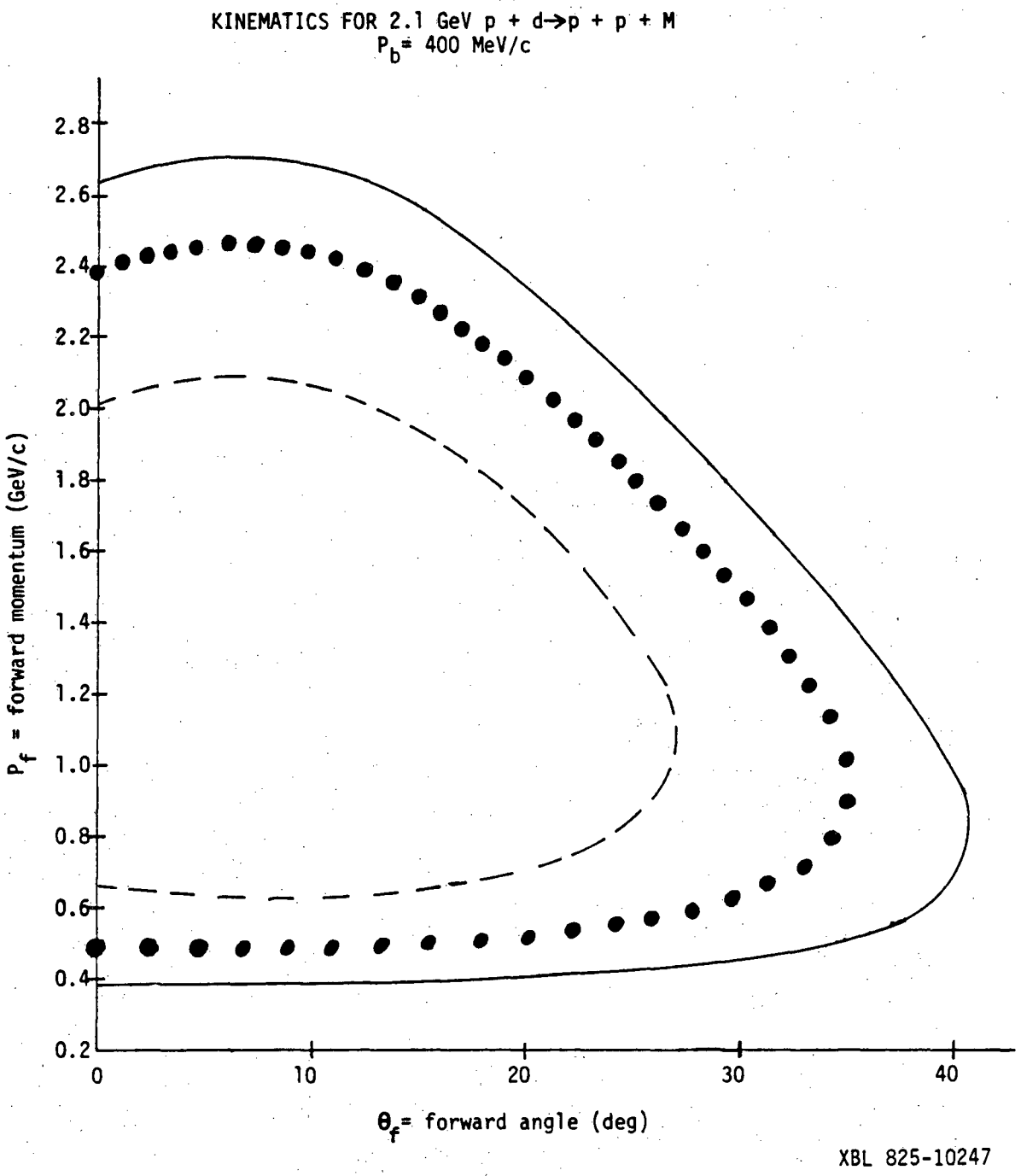
KINEMATICS FOR 2.1 GeV p + d→p + p + M
P_b= 400 MeV/c
2.8
2.6
2.4
2.2
2.0
1.8
1.6
1.4
1.2
1.0
0.8
0.6
0.4
0.2
P_f = forward momentum (GeV/c)
0
10
20
30
40
θ_f= forward angle (deg)
XBL 825-10247

Fig. 6

Possible Dynamics

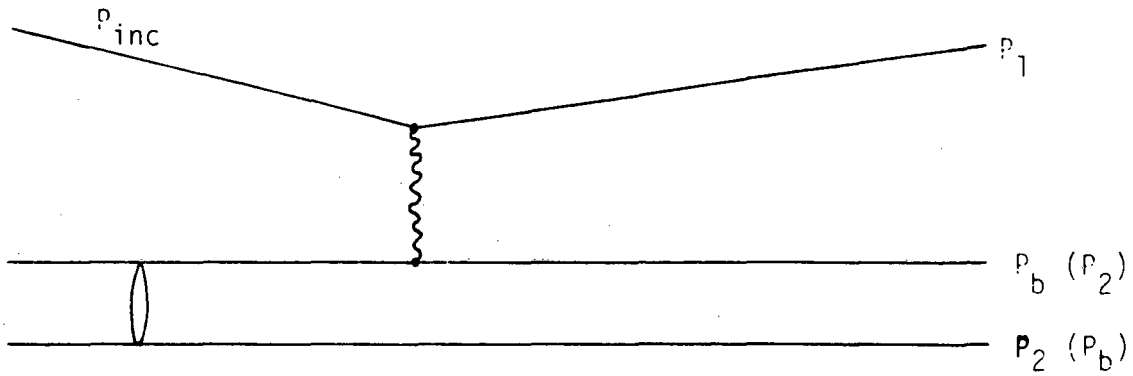

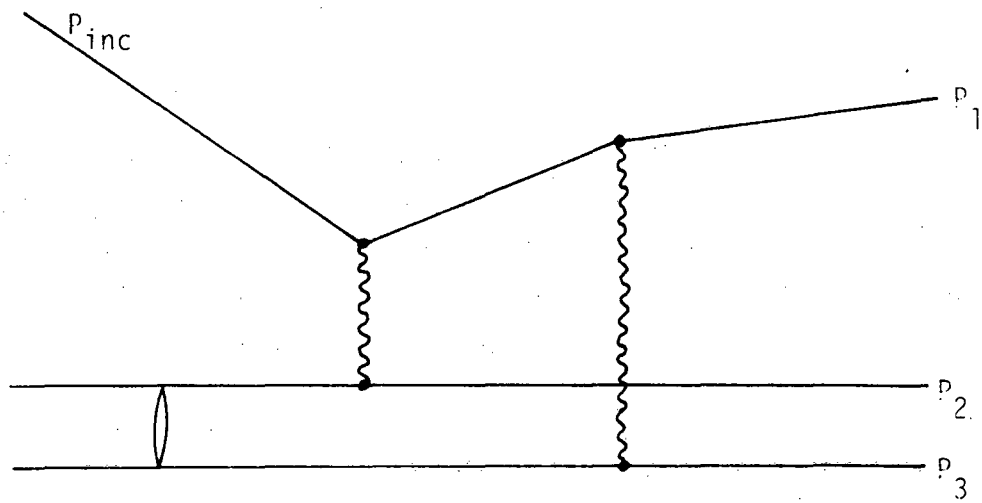

XBL 825-10113

Fig. 7a,b

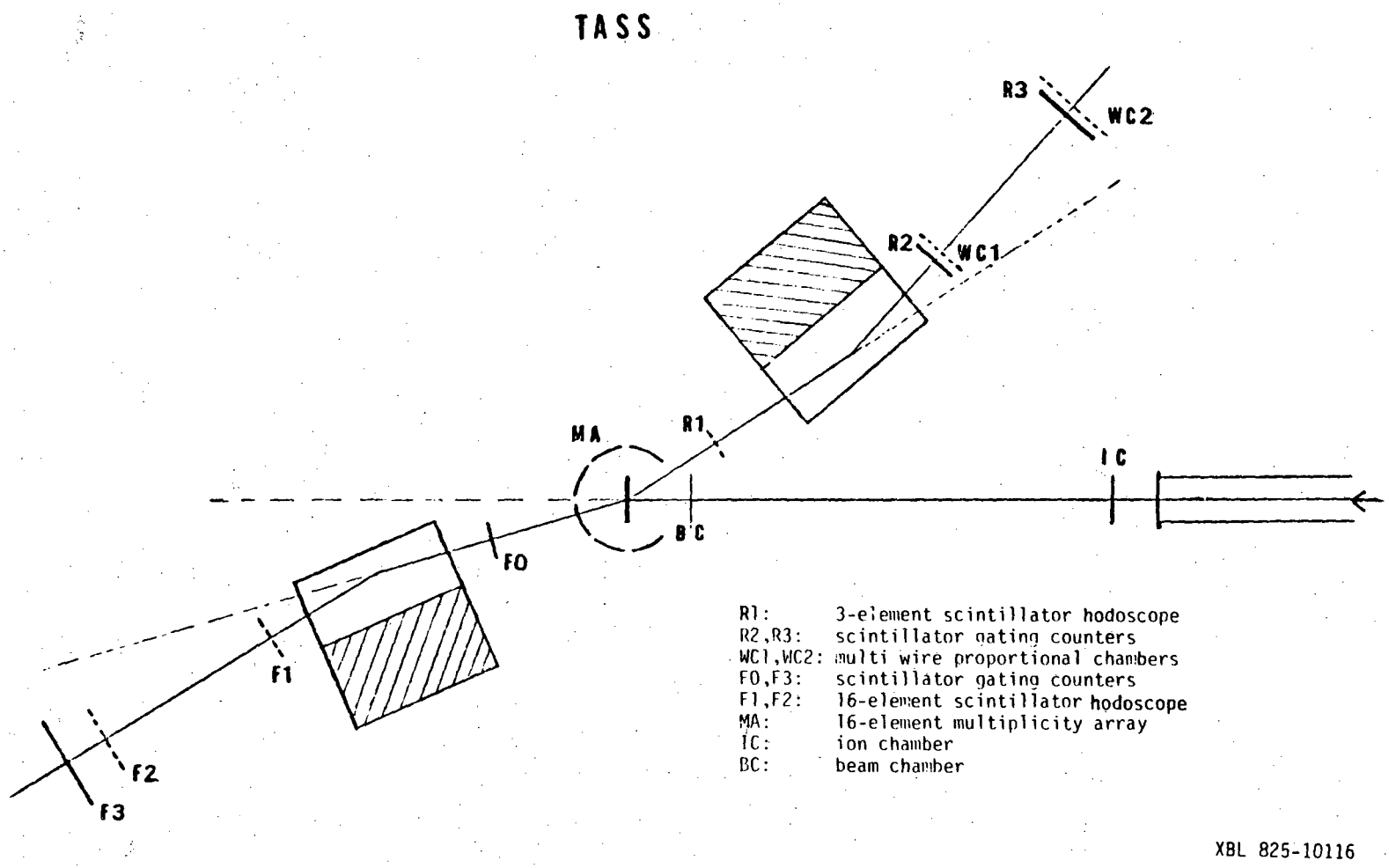

XBL 825-10116

Fig. 8

TASS Coordinate System

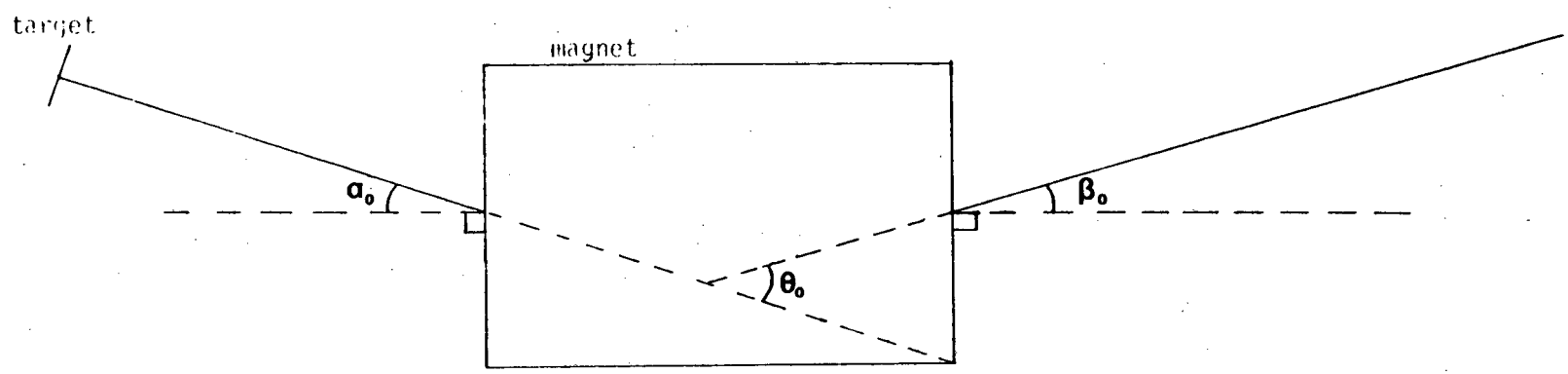

XBL 825-10117

Fig. 9

Data Acquisition Scheme

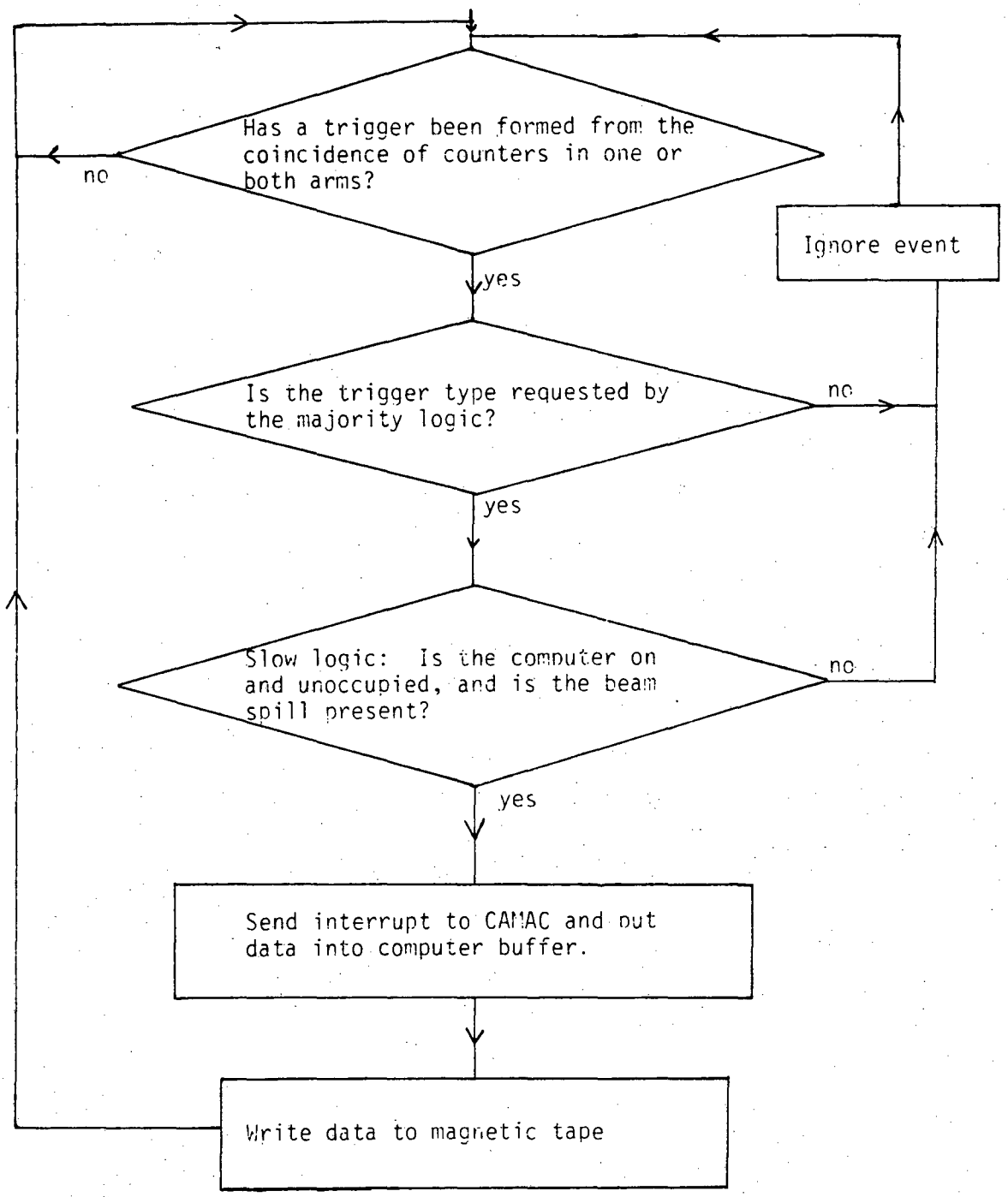

XBL 825-10115

Fig. 10

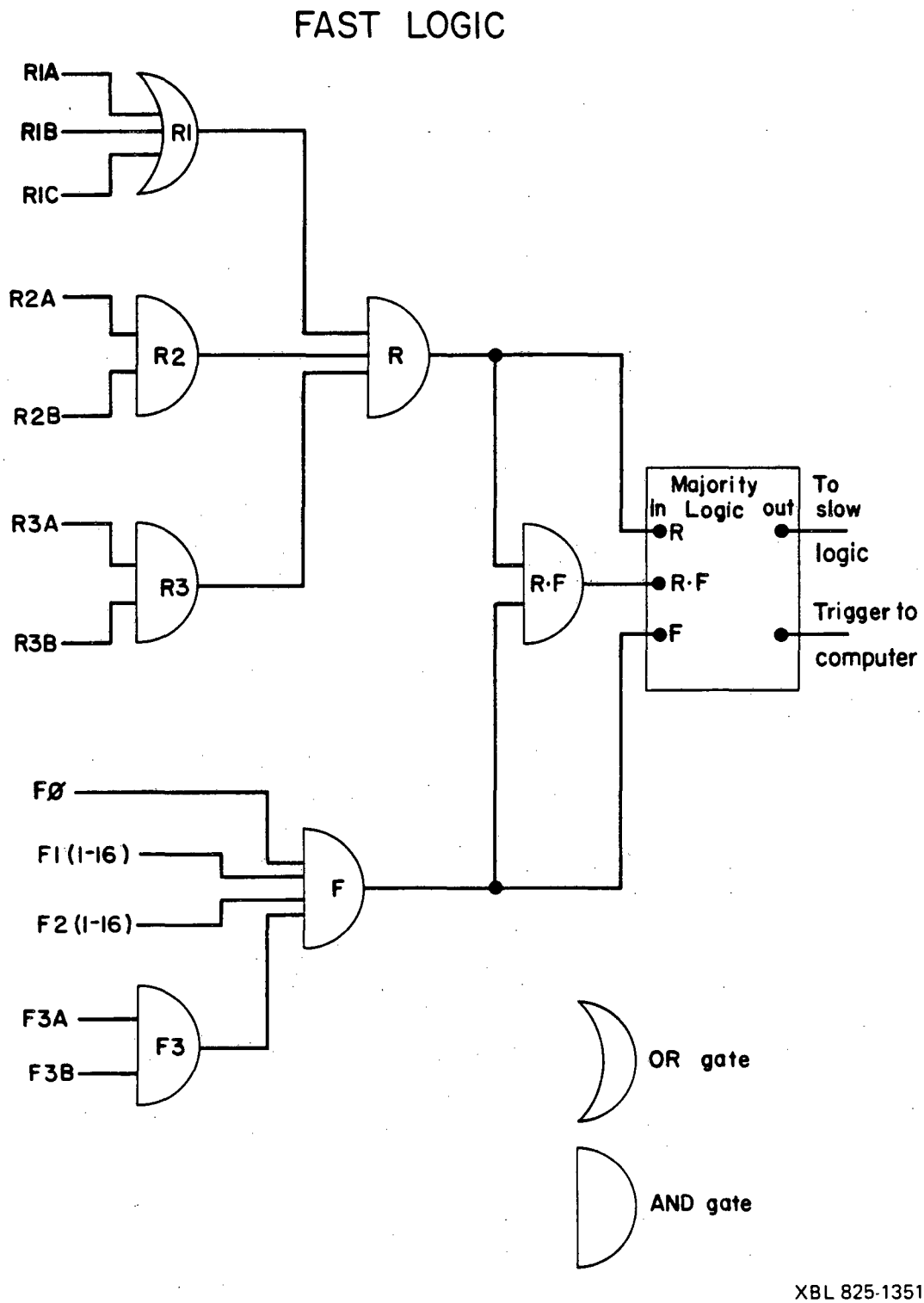
FAST LOGIC
R1A
R1B
R1C
R1
R2A
R2
R2B
R
R3A
R3
R3B
R·F
Majority Logic
In
out
R
R·F
F
To slow logic
Trigger to computer
FØ
F1 (1-16)
F2 (1-16)
F
F3A
F3
F3B
OR gate
AND gate
XBL 825-1351

Fig. 11

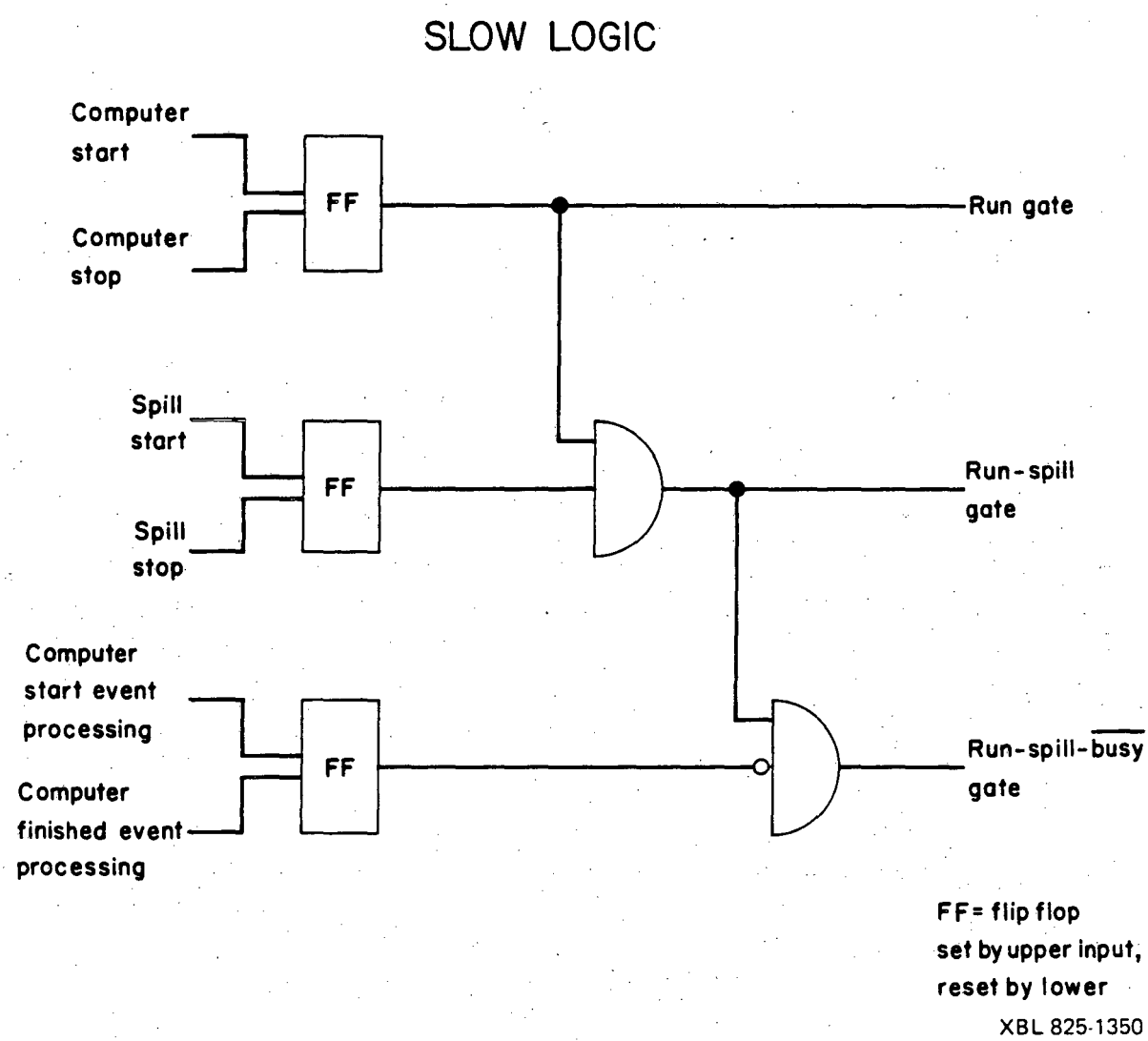
SLOW LOGIC
Computer start
Computer stop
FF
Run gate
Spill start
Spill stop
FF
Run-spill gate
Computer start event processing
Computer finished event processing
FF
Run-spill-busy gate
FF= flip flop set by upper input, reset by lower
XBL 825-1350

Fig. 12

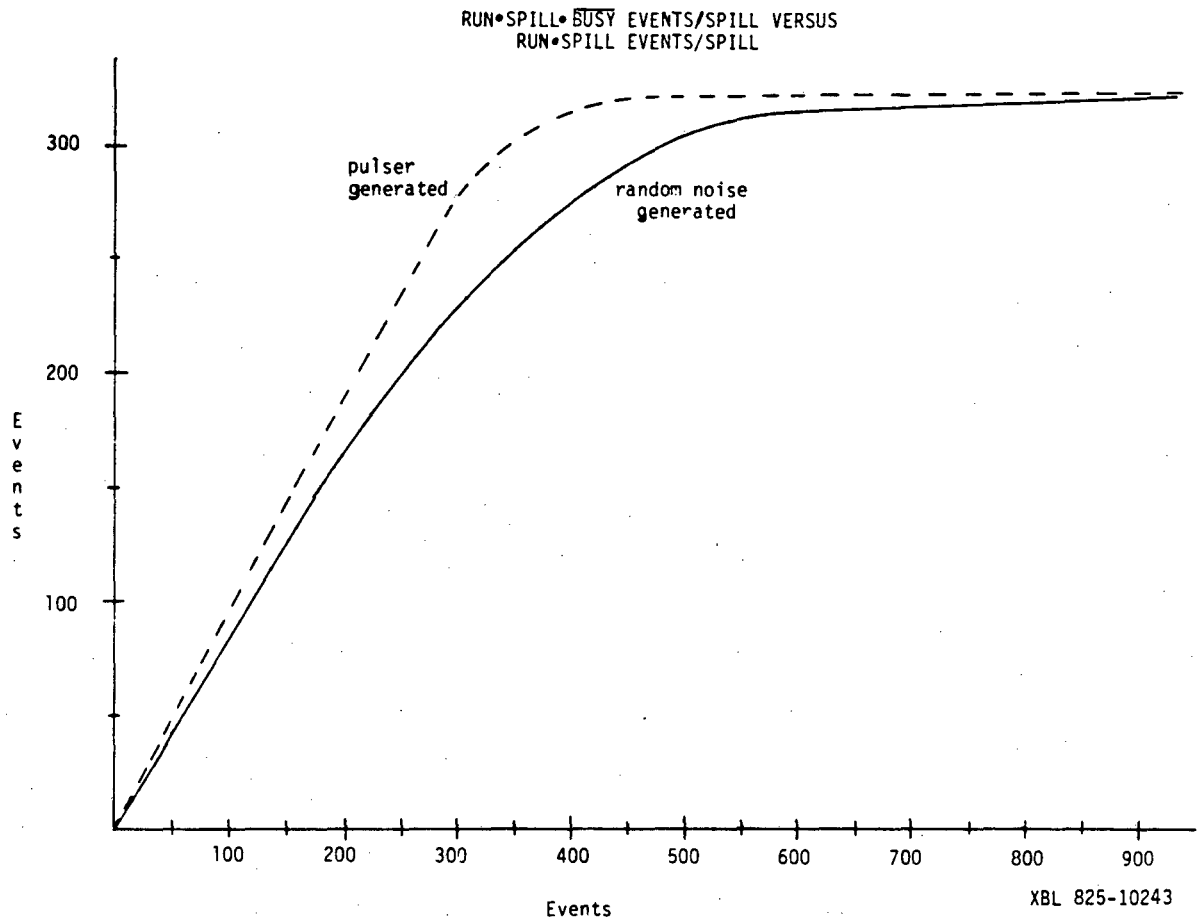
RUN•SPILL•$\overline{\text{BUSY}}$ EVENTS/SPILL VERSUS
RUN•SPILL EVENTS/SPILL
300
200
100
Events
pulser
generated
random noise
generated
100
200
300
400
500
600
700
800
900
Events
XBL 825-10243

Fig. 13

Subroutine E444H.MBD for
Data Acquisition

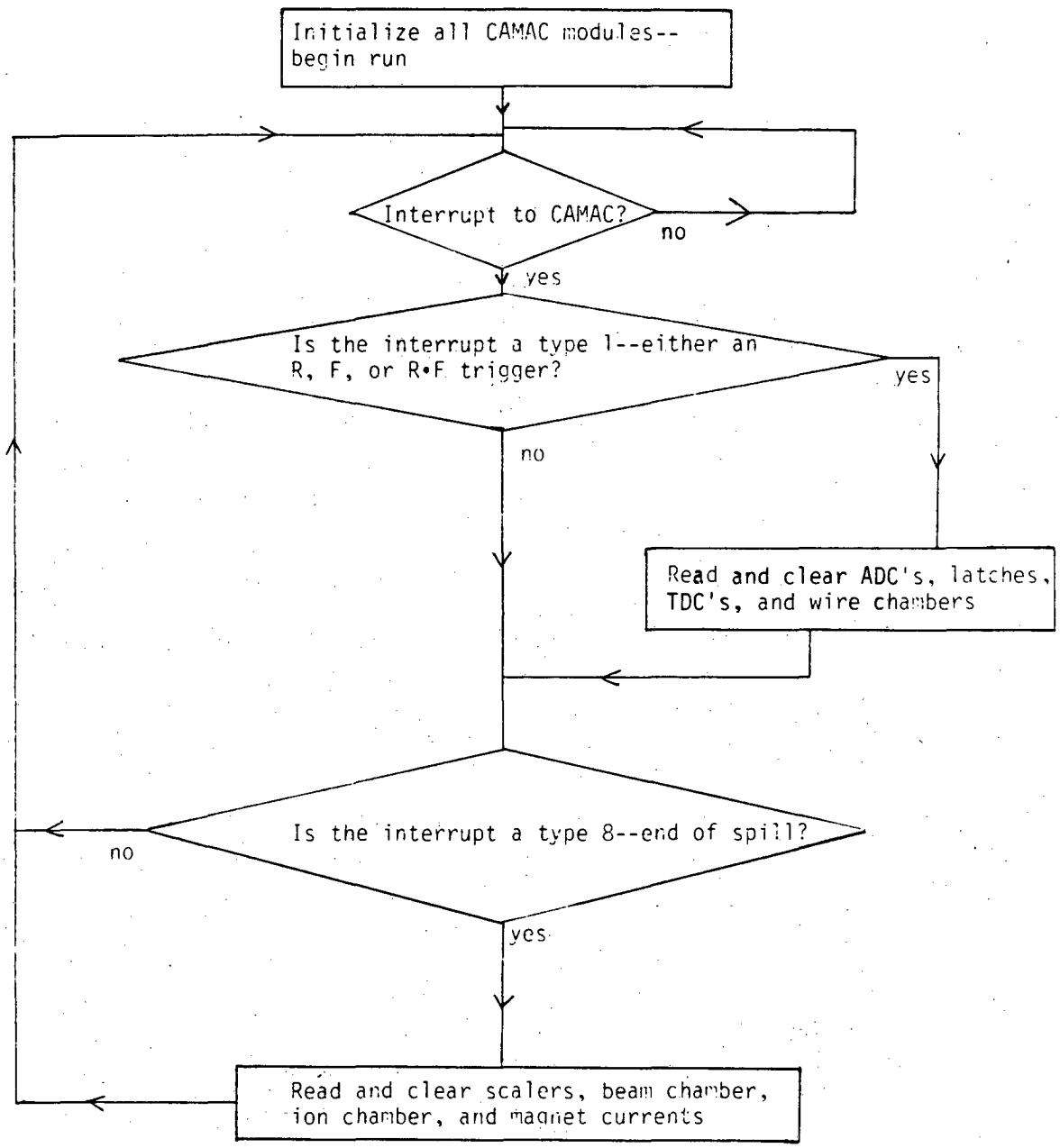

XBL 825-10114

Fig. 14

Percent Deviation of Measured Momentum
From Wire Momentum Versus
Deviation from Central Momentum

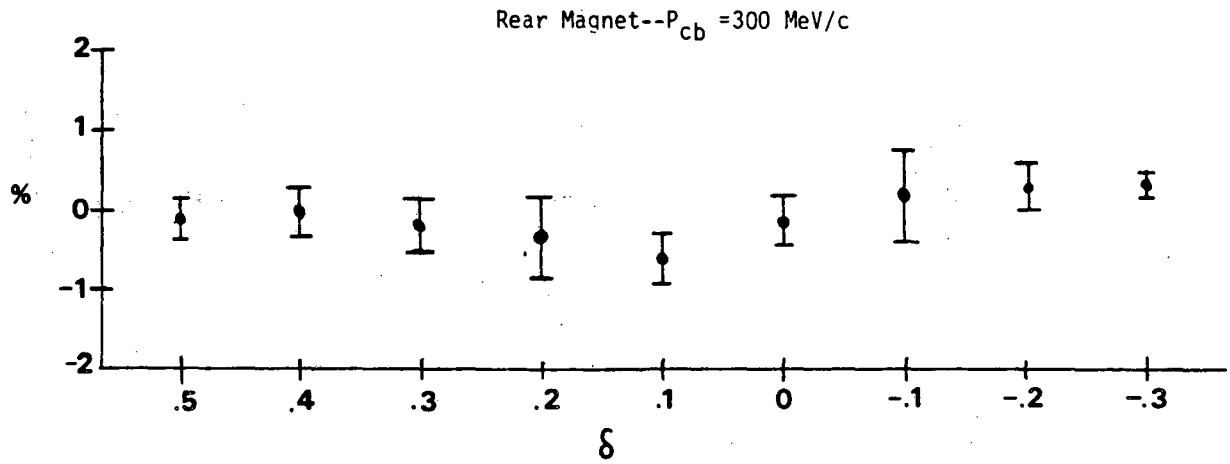

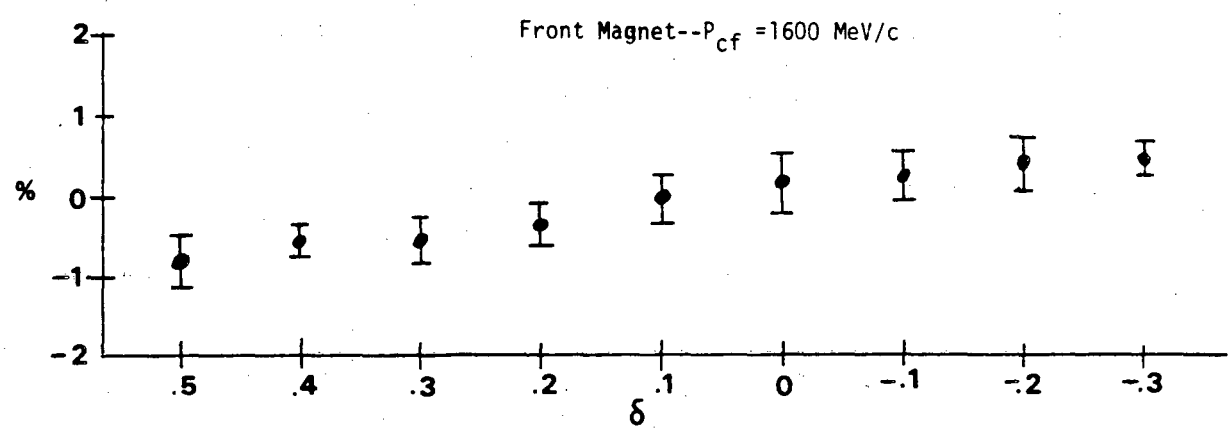

XBL 825-10242

Fig. 15a,b

MOMENTUM RESOLUTION IN A SQUARE FIELD

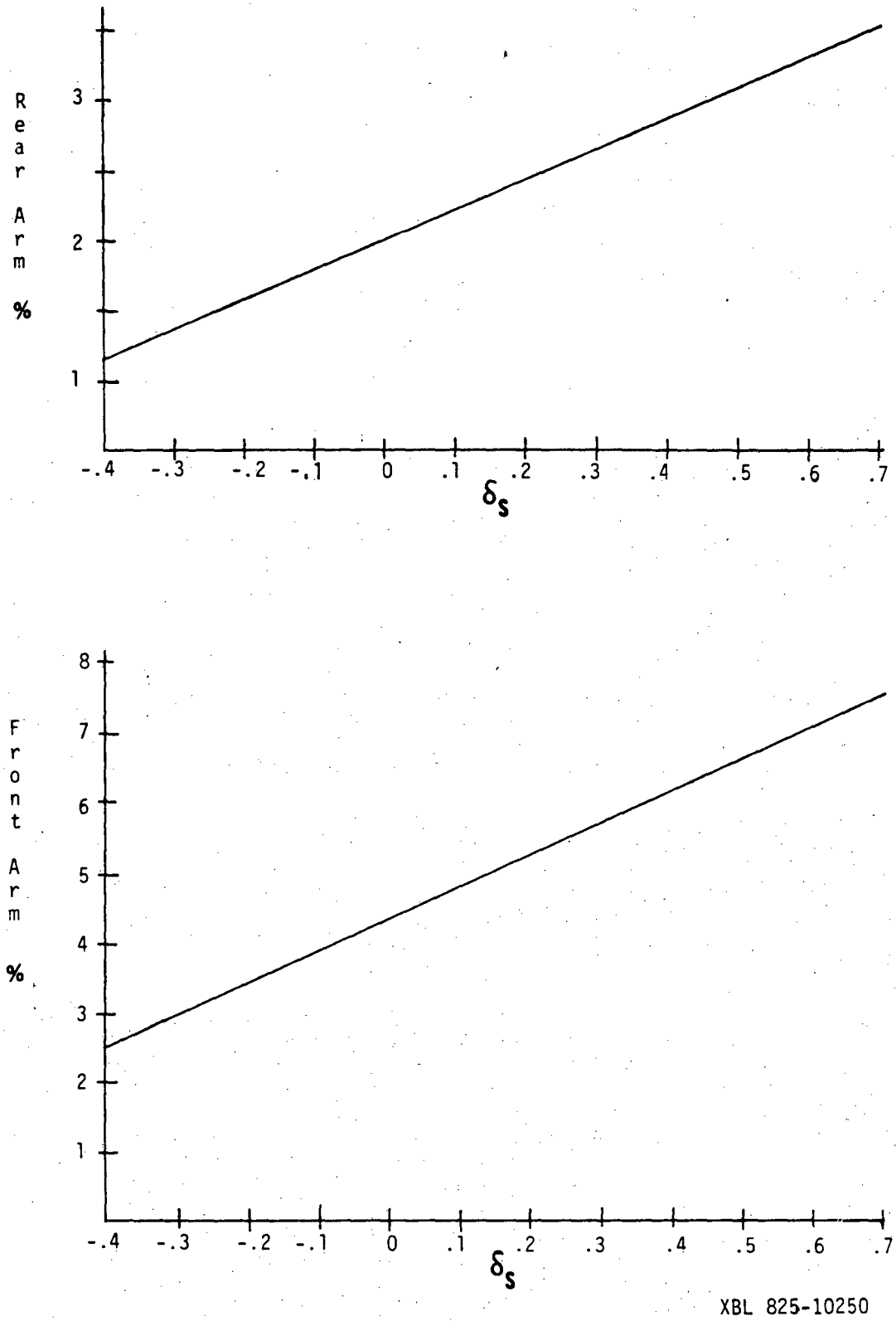

Fig. 16a,b

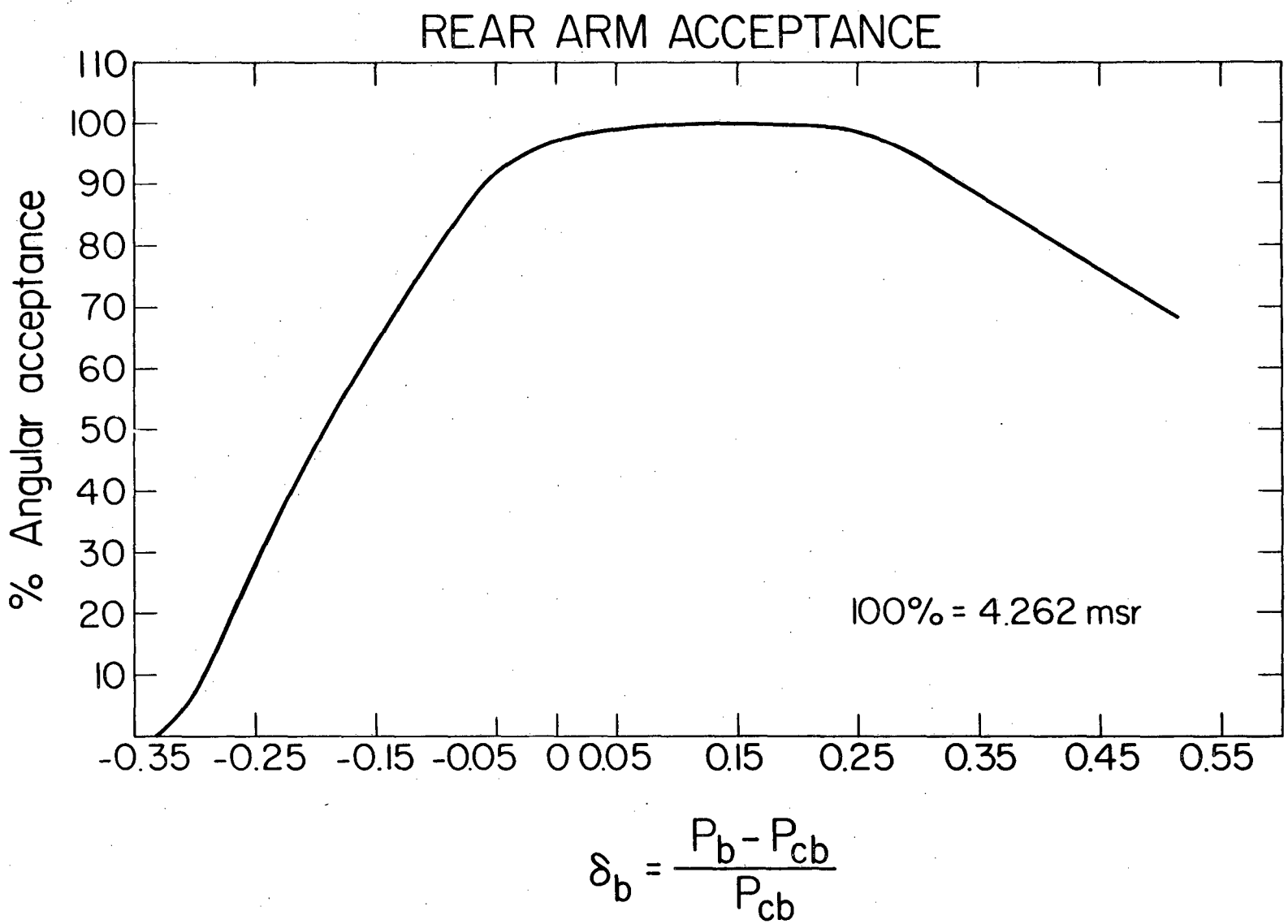

XBL 825-1354

Fig. 17a

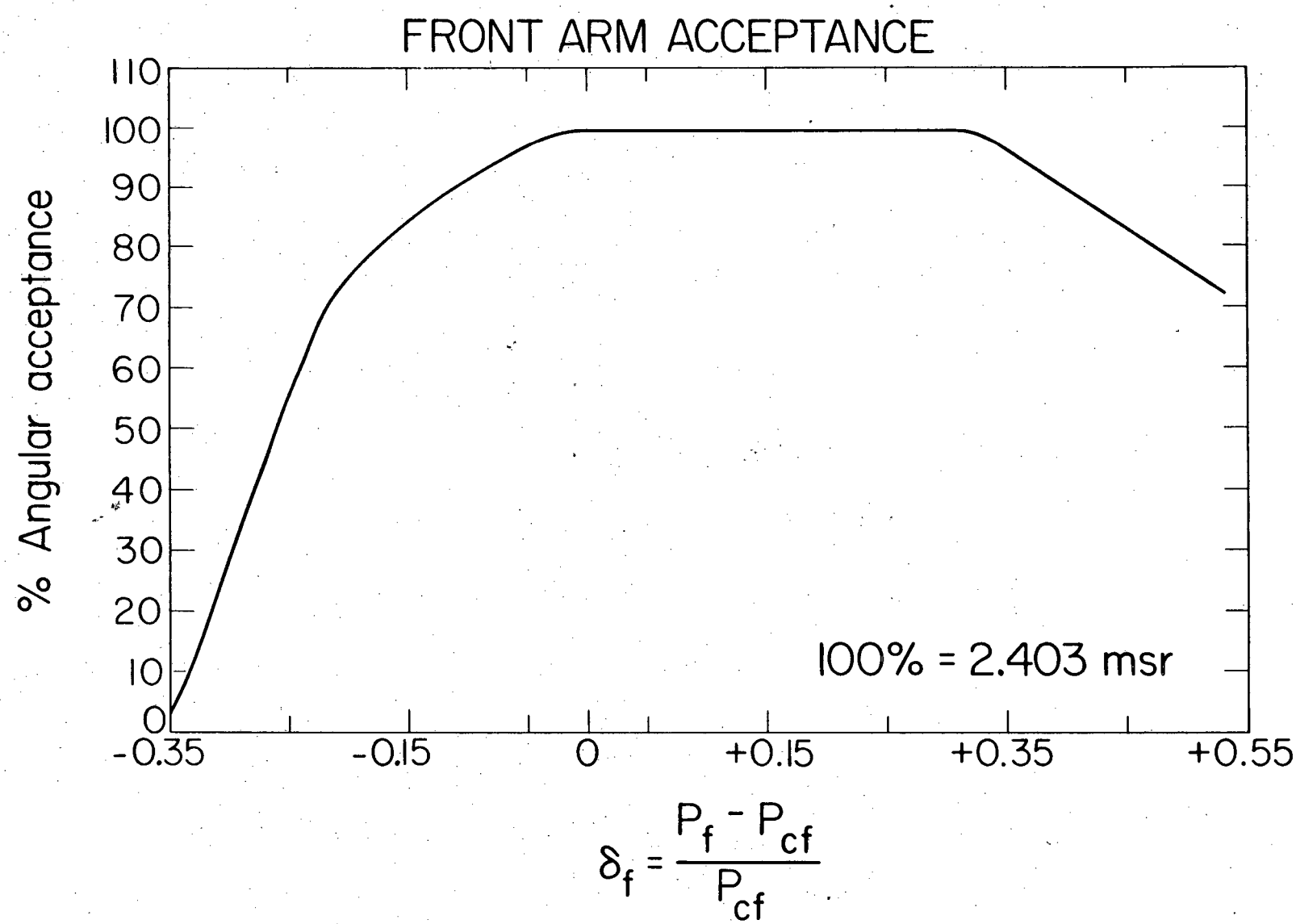
FRONT ARM ACCEPTANCE
% Angular acceptance
110
100
90
80
70
60
50
40
30
20
10
0
-0.35
-0.15
0
+0.15
+0.35
+0.55
100% = 2.403 msr
$\delta_f = \frac{P_f - P_{cf}}{P_{cf}}$
XBL 825-1353

Fig. 17b

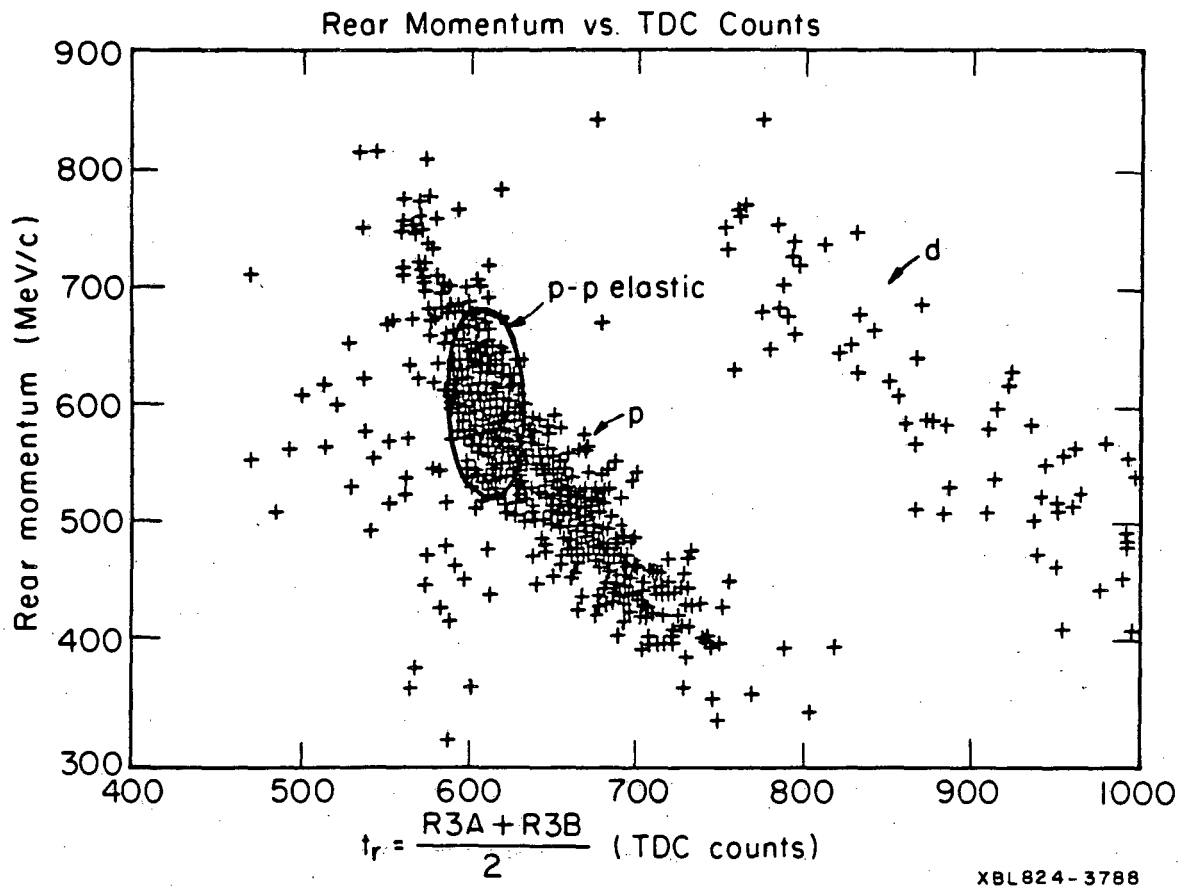
Rear Momentum vs. TDC Counts
Rear momentum (MeV/c)
900
800
700
600
500
400
300
400
500
600
700
800
900
1000
p-p elastic
p
d
$t_r = \frac{R3A + R3B}{2}$ (TDC counts)
XBL824-3788

Fig. 18

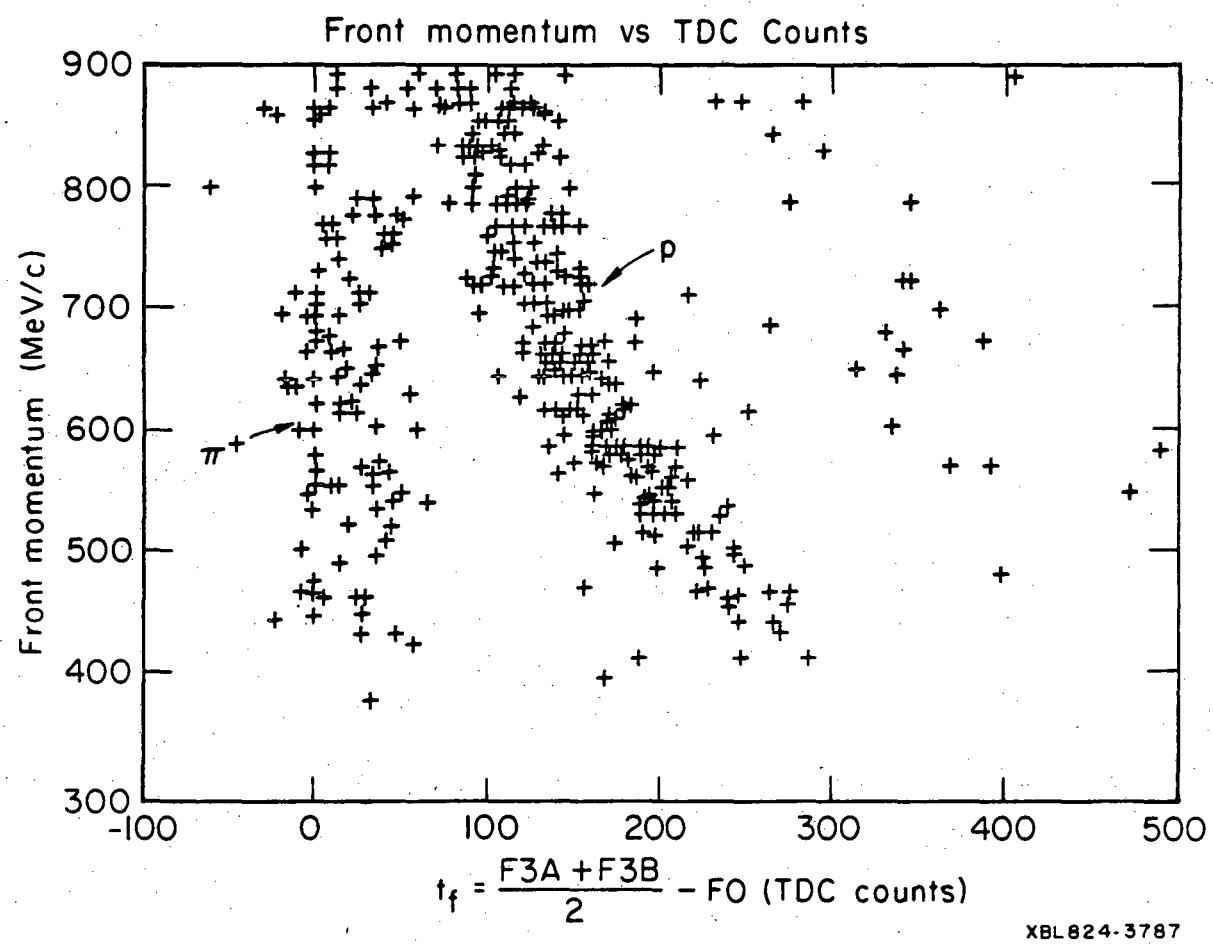
Front momentum vs TDC Counts
Front momentum (MeV/c)
900
800
700
600
500
400
300
-100
0
100
200
300
400
500
p
π+
$t_f = \frac{F3A + F3B}{2} - FO$ (TDC counts)
XBL824-3787

Fig. 19

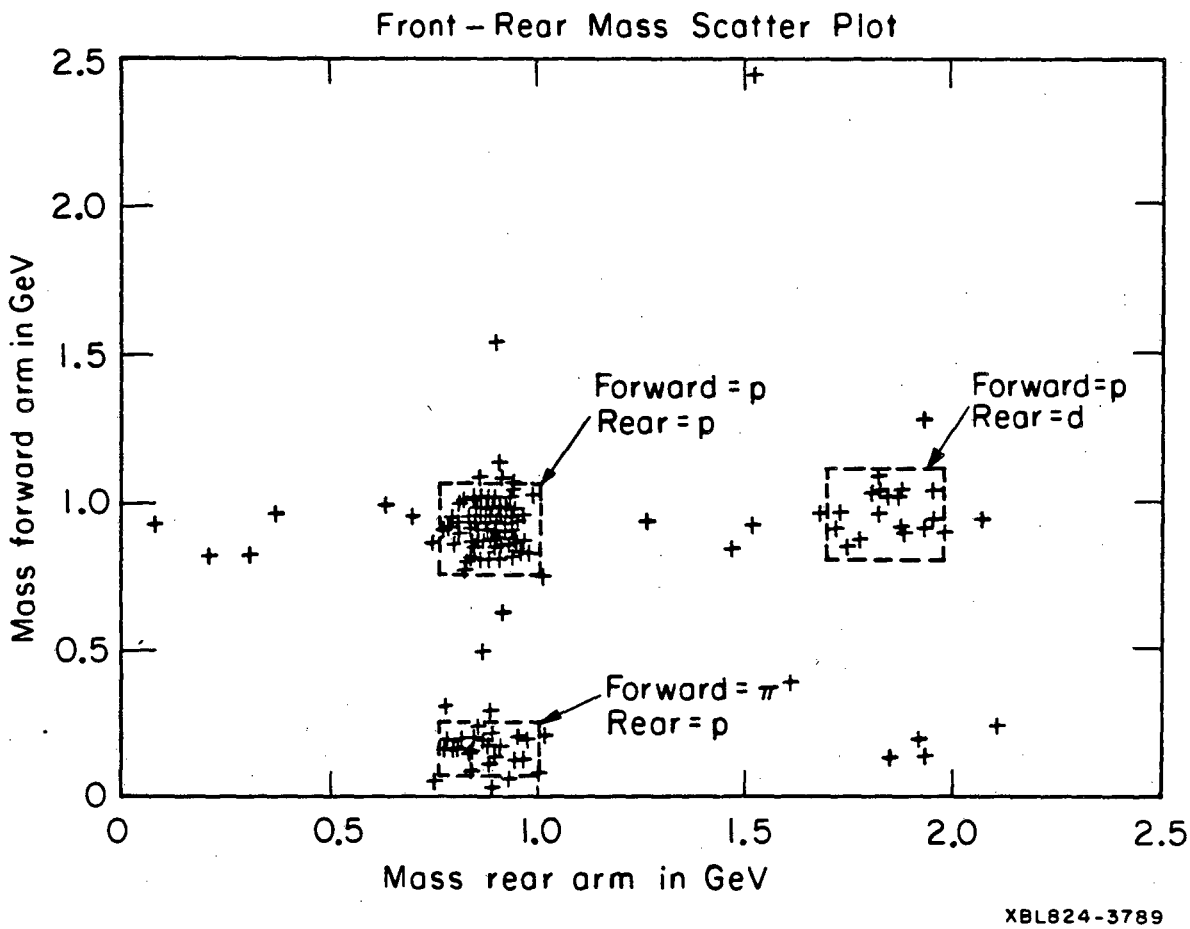
Front – Rear Mass Scatter Plot
Mass forward arm in GeV
Mass rear arm in GeV
2.5
2.0
1.5
1.0
0.5
0
0
0.5
1.0
1.5
2.0
2.5
Forward = p
Rear = p
Forward=p
Rear=d
Forward = π+
Rear = p
XBL824-3789

Fig. 20

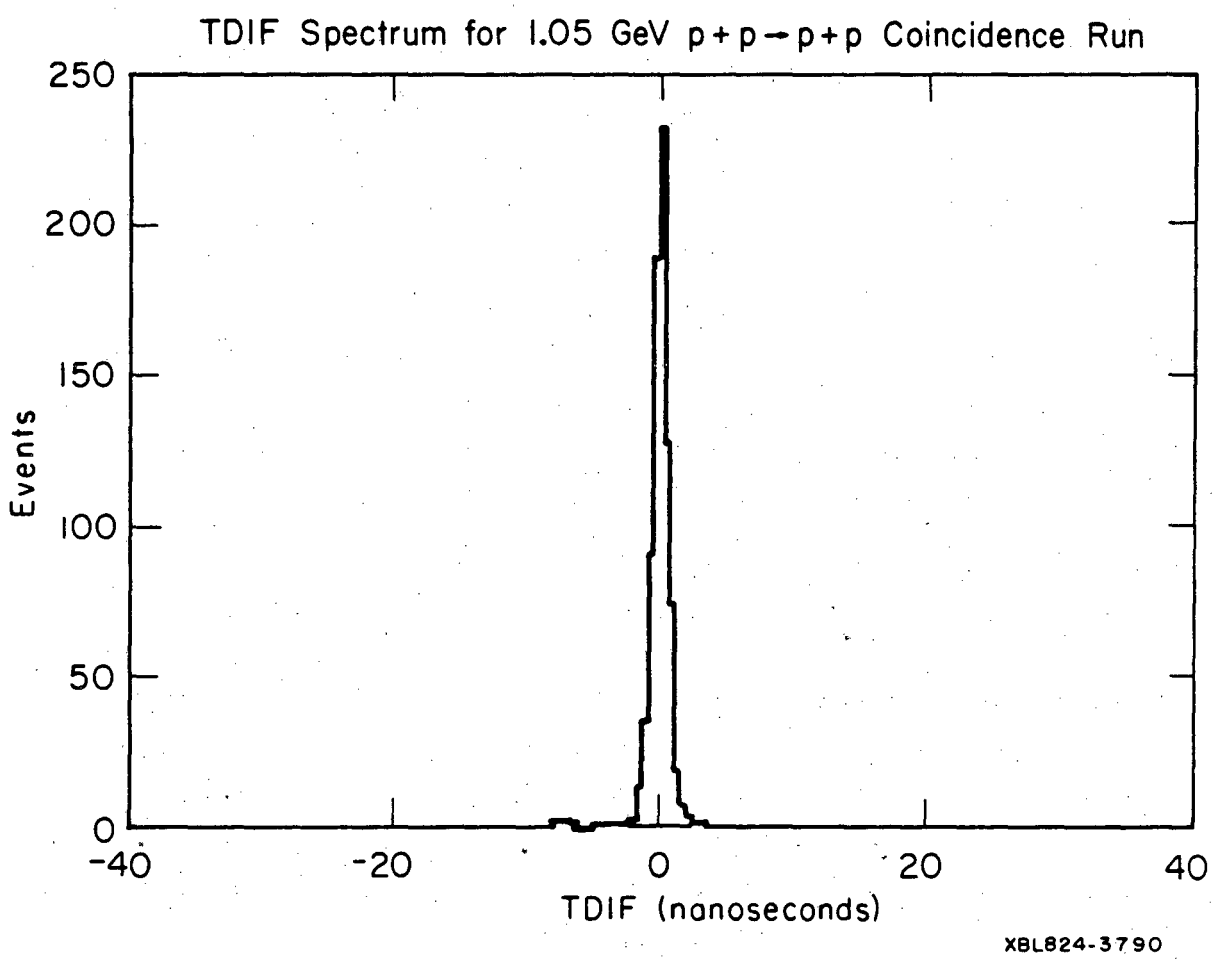
TDIF Spectrum for 1.05 GeV p+p→p+p Coincidence Run
250
200
150
100
50
0
Events
-40
-20
0
20
40
TDIF (nanoseconds)
XBL824-3790

Fig. 21a

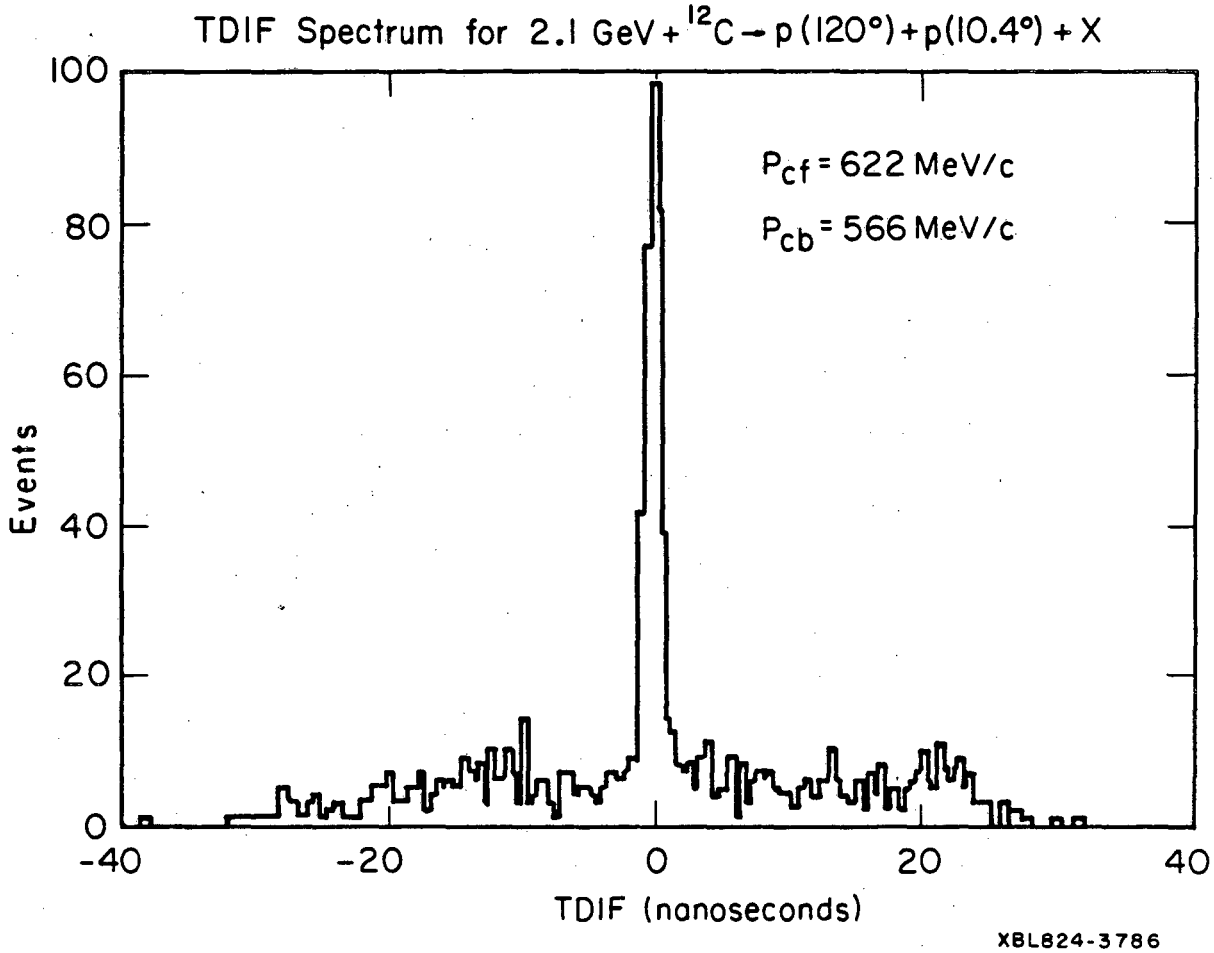
TDIF Spectrum for 2.1 GeV + ^{12}C → p(120°) + p(10.4°) + X
P_{cf} = 622 MeV/c
P_{cb} = 566 MeV/c
Events
100
80
60
40
20
0
-40
-20
0
20
40
TDIF (nanoseconds)
XBL824-3786

Fig. 21b

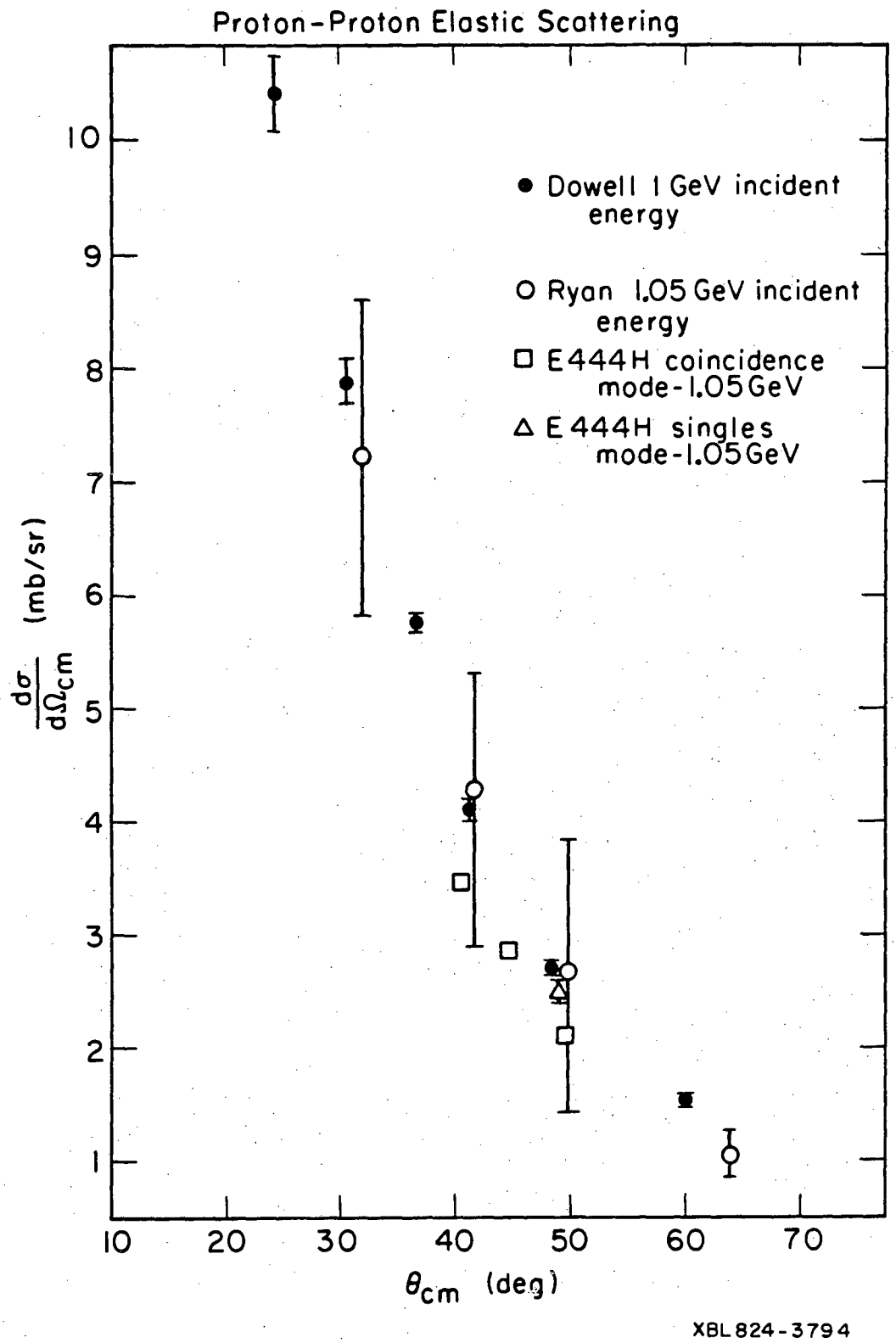
Proton-Proton Elastic Scattering
Dowell 1 GeV incident energy
Ryan 1.05 GeV incident energy
E444H coincidence mode-1.05GeV
E444H singles mode-1.05GeV
$\frac{d\sigma}{d\Omega_{cm}}$ (mb/sr)
θ_{cm} (deg)
XBL824-3794

Fig. 22

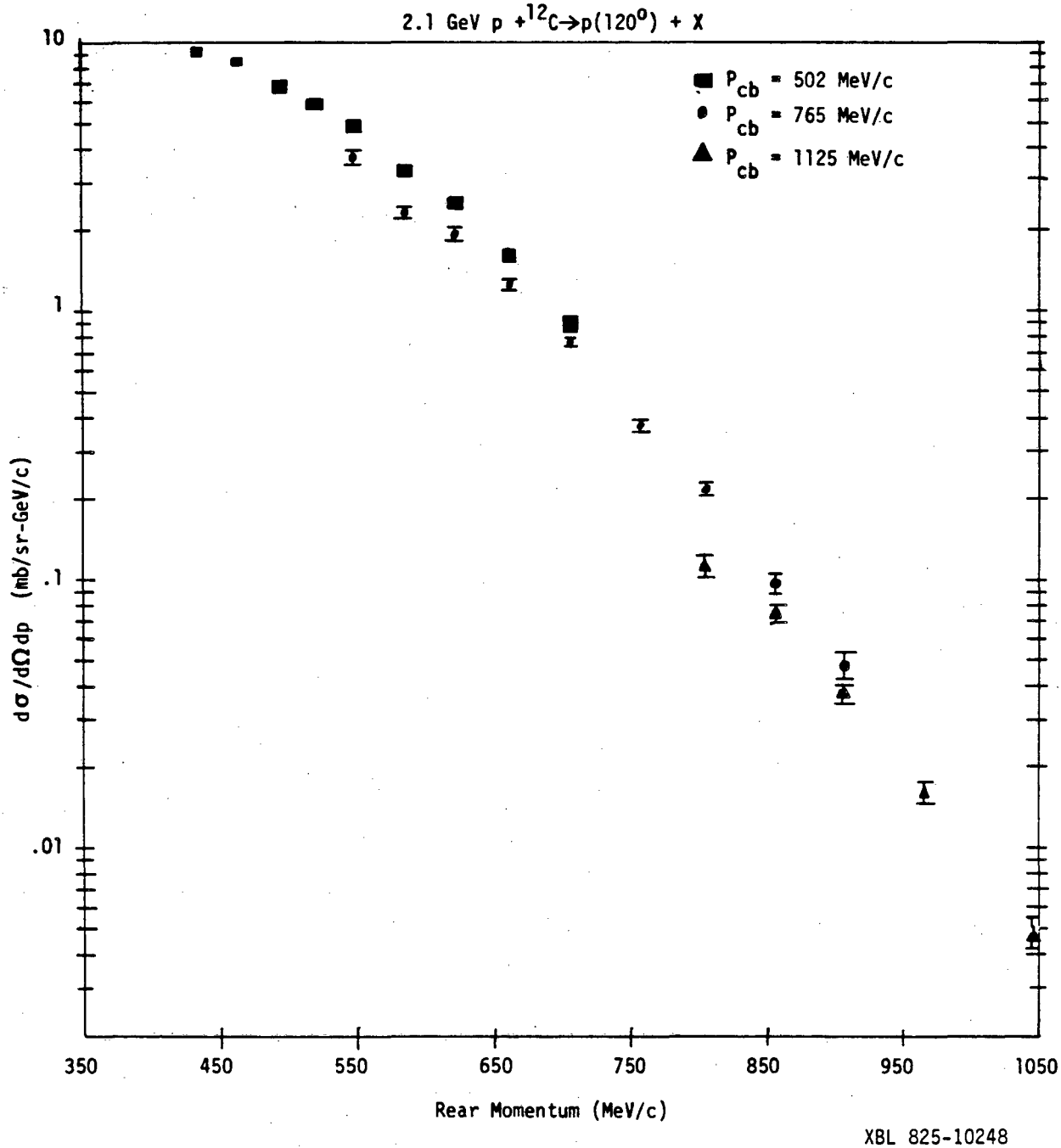
2.1 GeV p +12C→p(120°) + X
Pcb = 502 MeV/c
Pcb = 765 MeV/c
Pcb = 1125 MeV/c
dσ/dΩdp (mb/sr-GeV/c)
10
1
.1
.01
350
450
550
650
750
850
950
1050
Rear Momentum (MeV/c)
XBL 825-10248

Fig. 23a

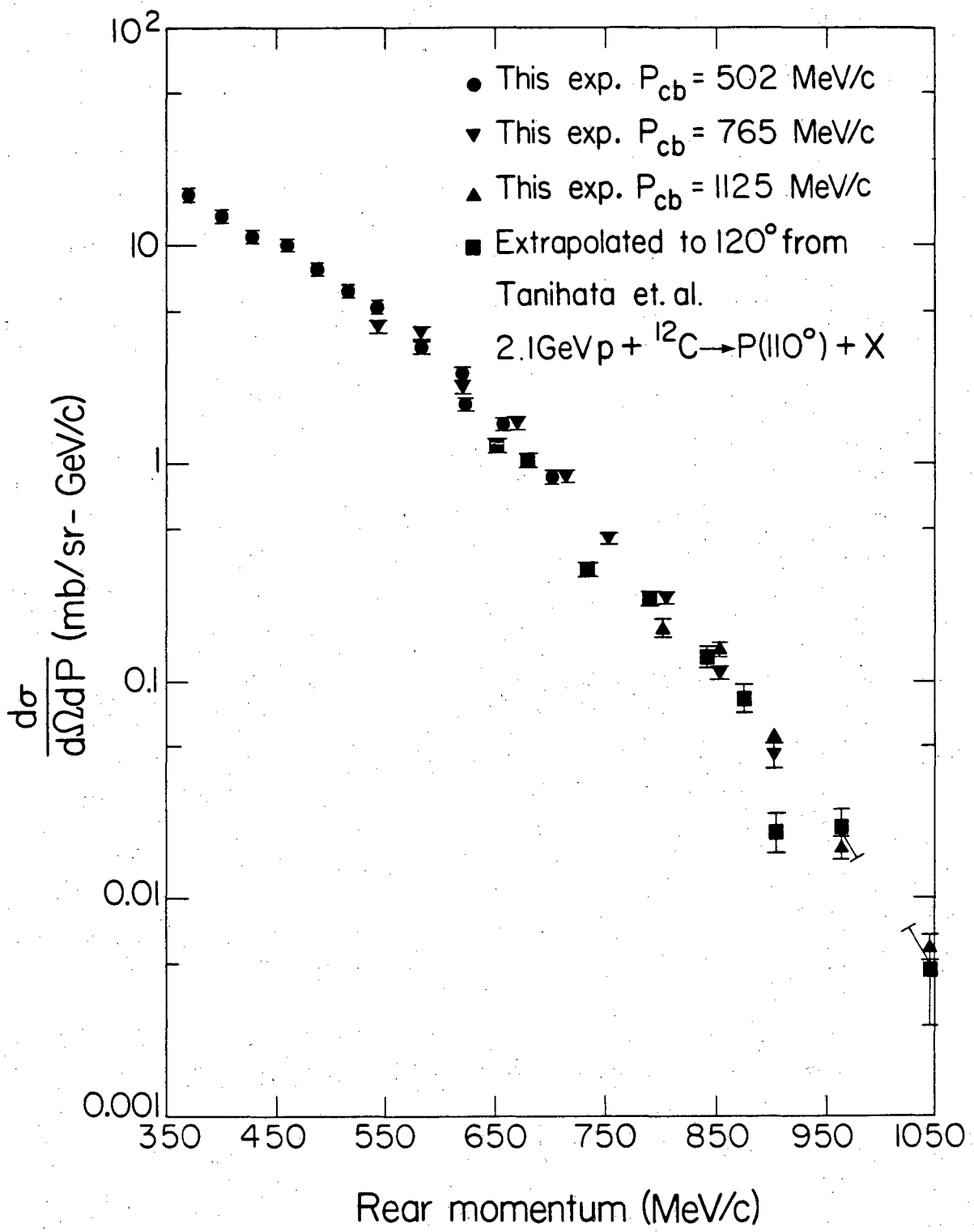

XBL 825-1359

Fig. 23b

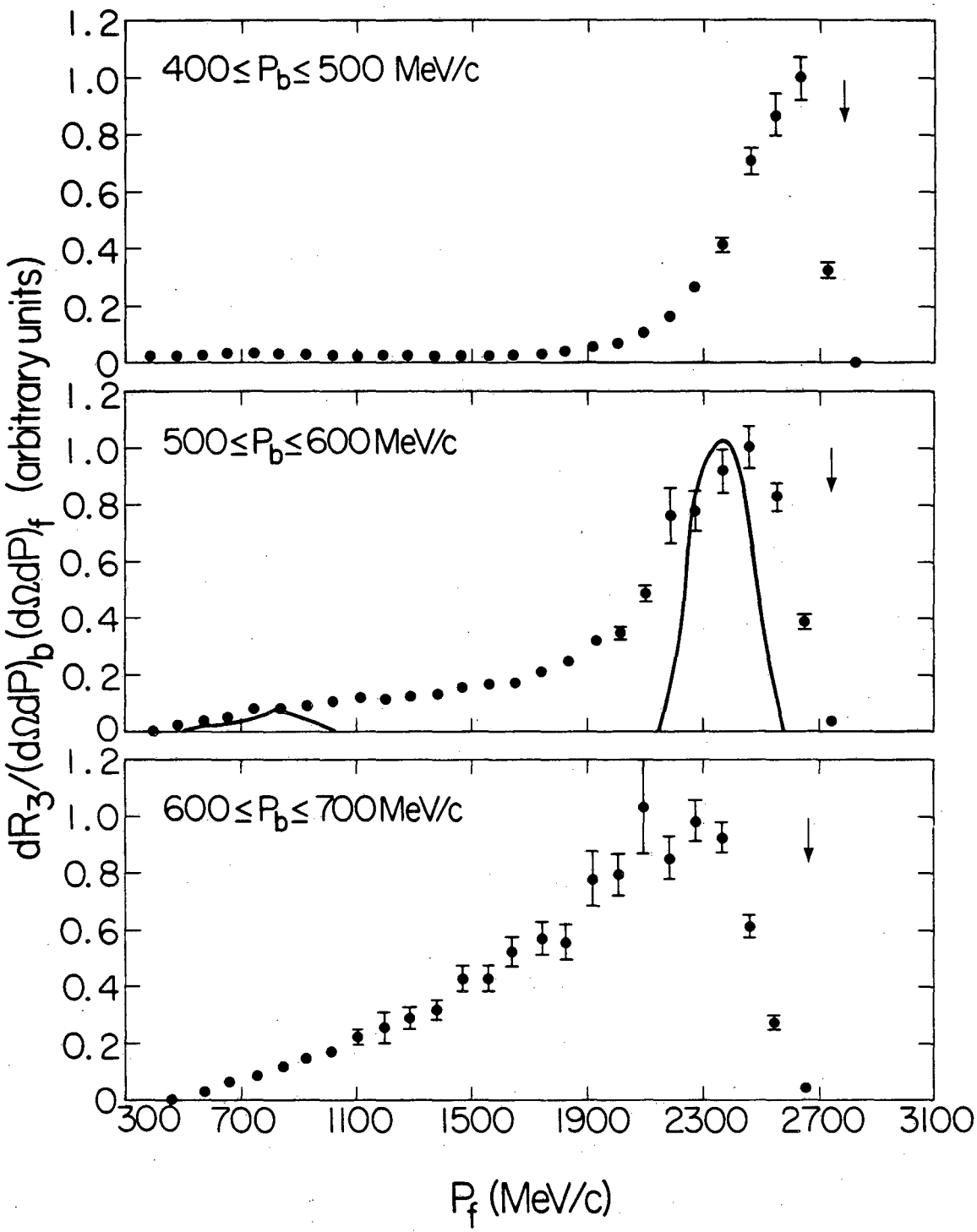

XBL 825-1361

Fig. 24a,b,c

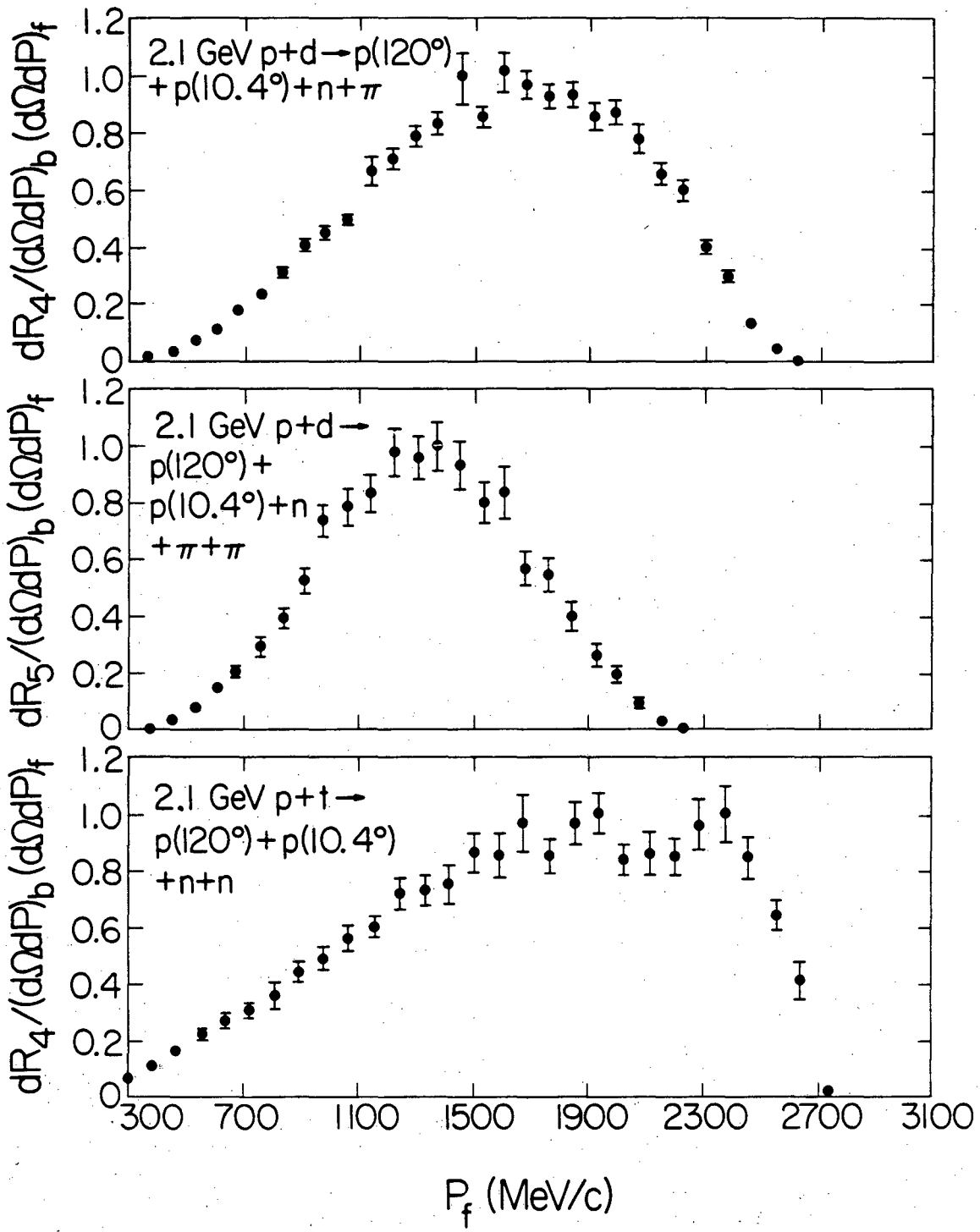

XBL 825-1360

Fig. 25a,b,c

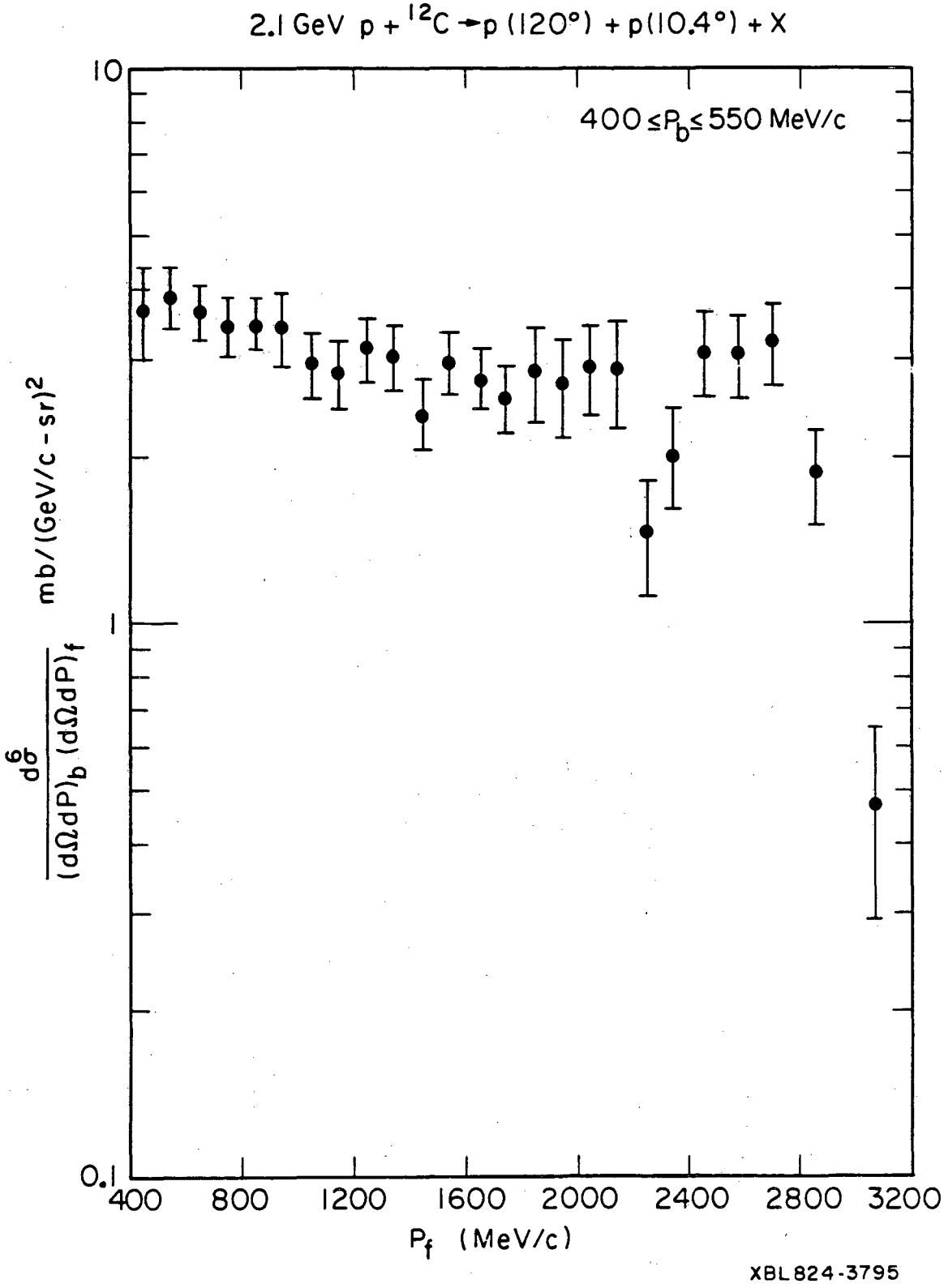
2.1 GeV p + ^{12}C → p (120°) + p(10.4°) + X
400 ≤ P_b ≤ 550 MeV/c
10
1
0.1
400
800
1200
1600
2000
2400
2800
3200
P_f (MeV/c)
$\frac{d^6\sigma}{(d\Omega dP)_b (d\Omega dP)_f}$ mb/(GeV/c - sr)^2
XBL824-3795

Fig. 26

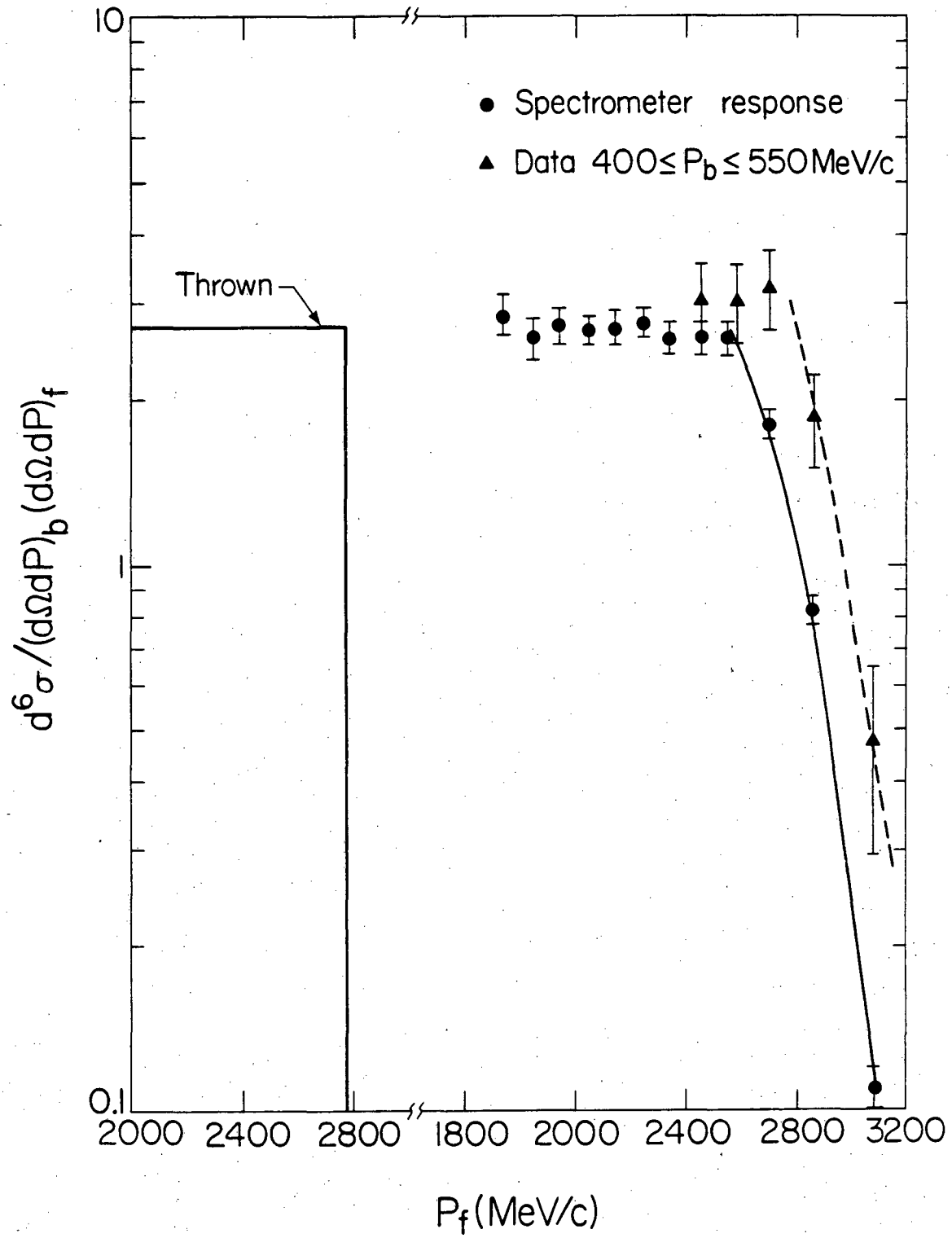

XBL 825-1356

Fig. 27

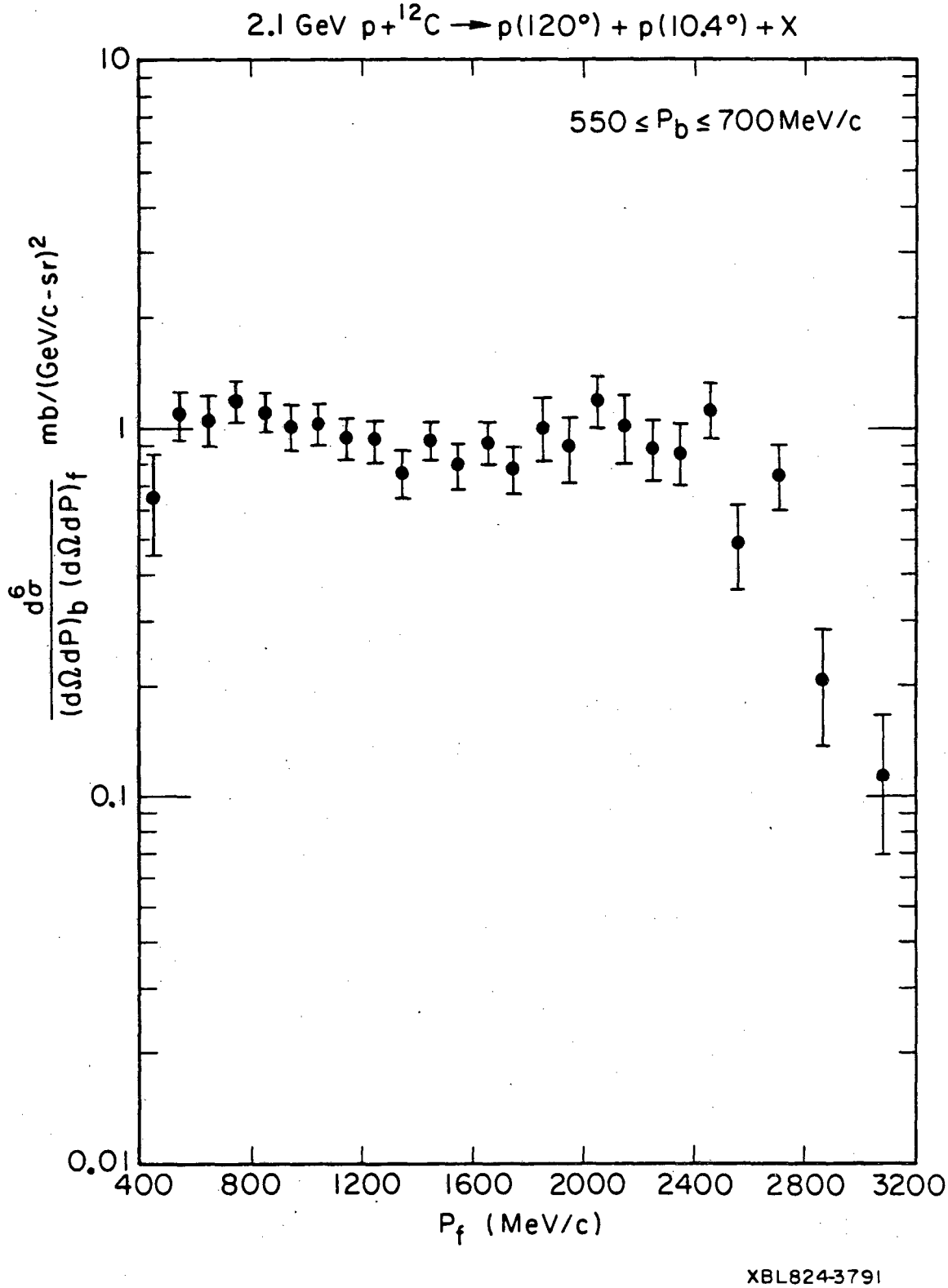
2.1 GeV p+^{12}C → p(120°) + p(10.4°) + X
550 ≤ P_b ≤ 700 MeV/c
$\frac{d^6\sigma}{(d\Omega dP)_b (d\Omega dP)_f}$ mb/(GeV/c-sr)^2
10
1
0.1
0.01
400
800
1200
1600
2000
2400
2800
3200
P_f (MeV/c)
XBL824-3791

Fig. 28

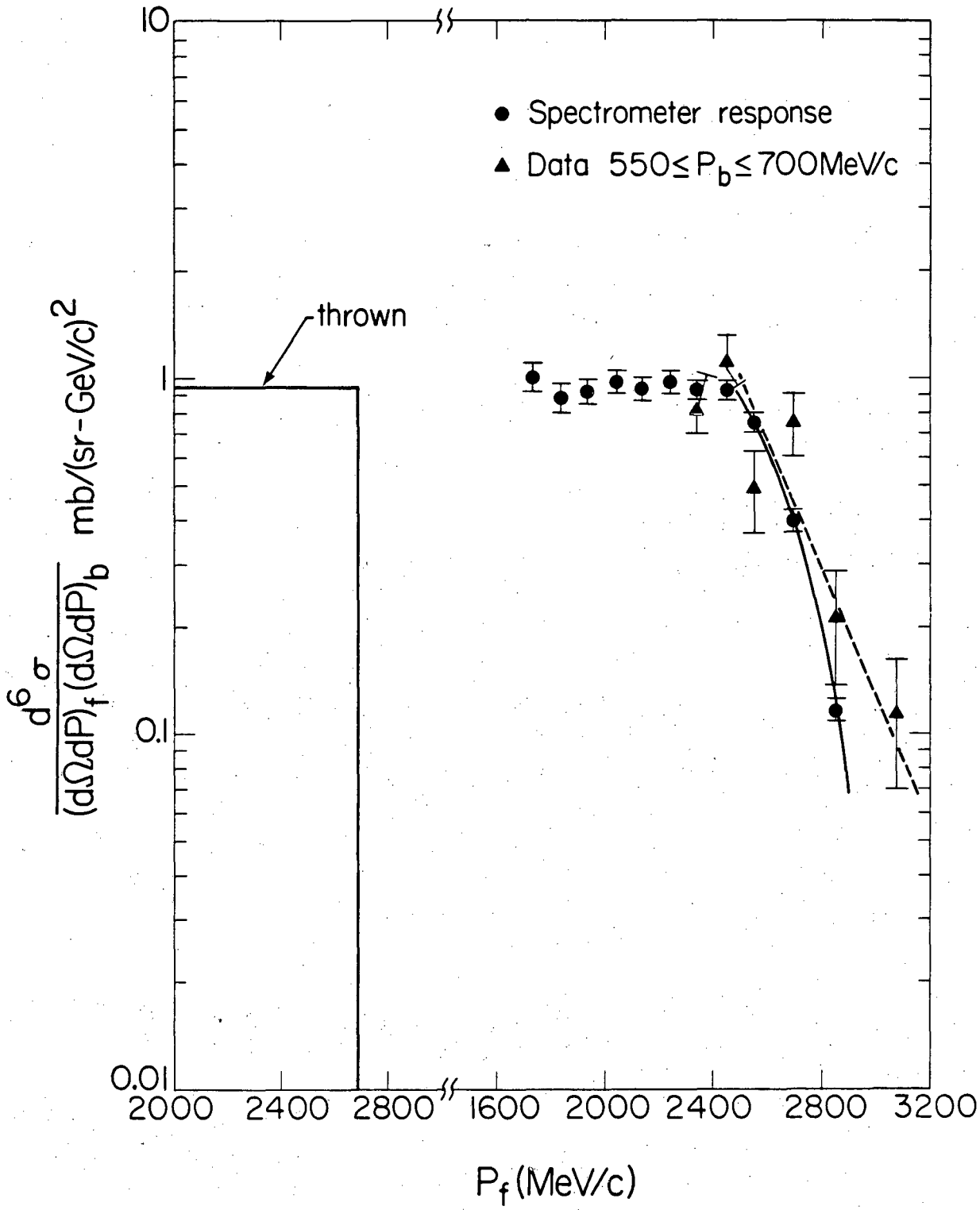

XBL 825-1355

Fig. 29

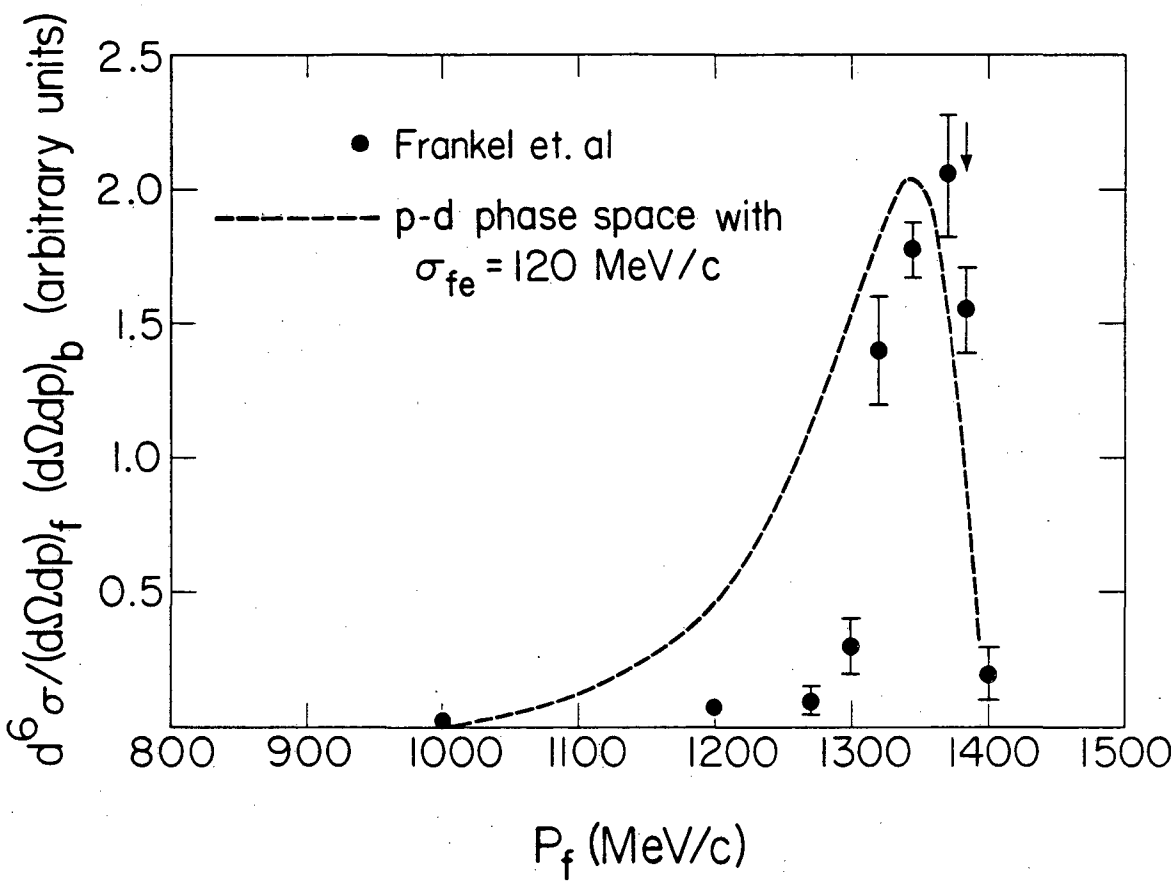

XBL 825-1352

Fig. 30

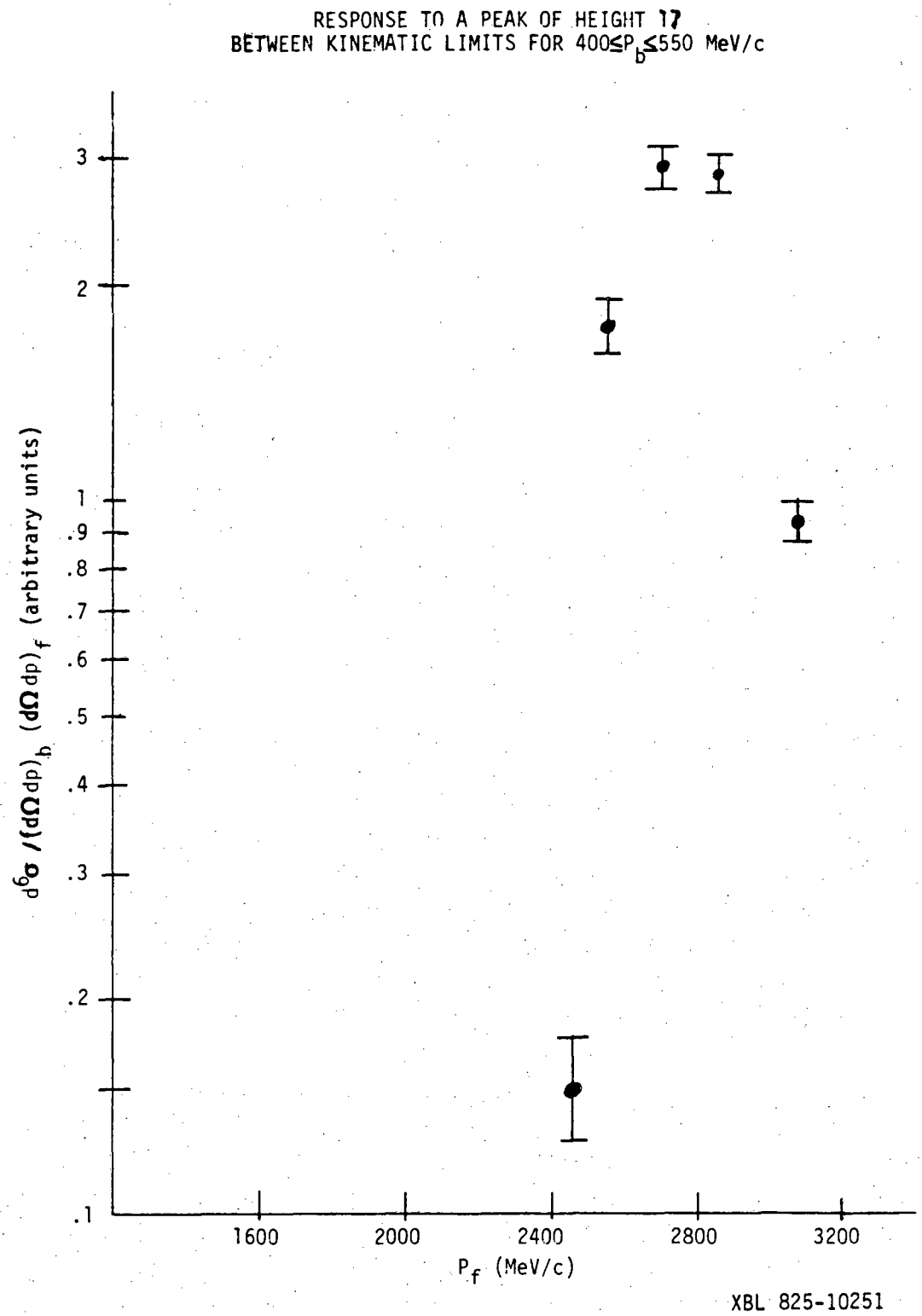
RESPONSE TO A PEAK OF HEIGHT 17
BETWEEN KINEMATIC LIMITS FOR 400≤P_b≤550 MeV/c
d^6σ /(dΩ dp)_b (dΩ dp)_f (arbitrary units)
3
2
1
.9
.8
.7
.6
.5
.4
.3
.2
.1
1600
2000
2400
2800
3200
P_f (MeV/c)
XBL 825-10251

Fig. 31

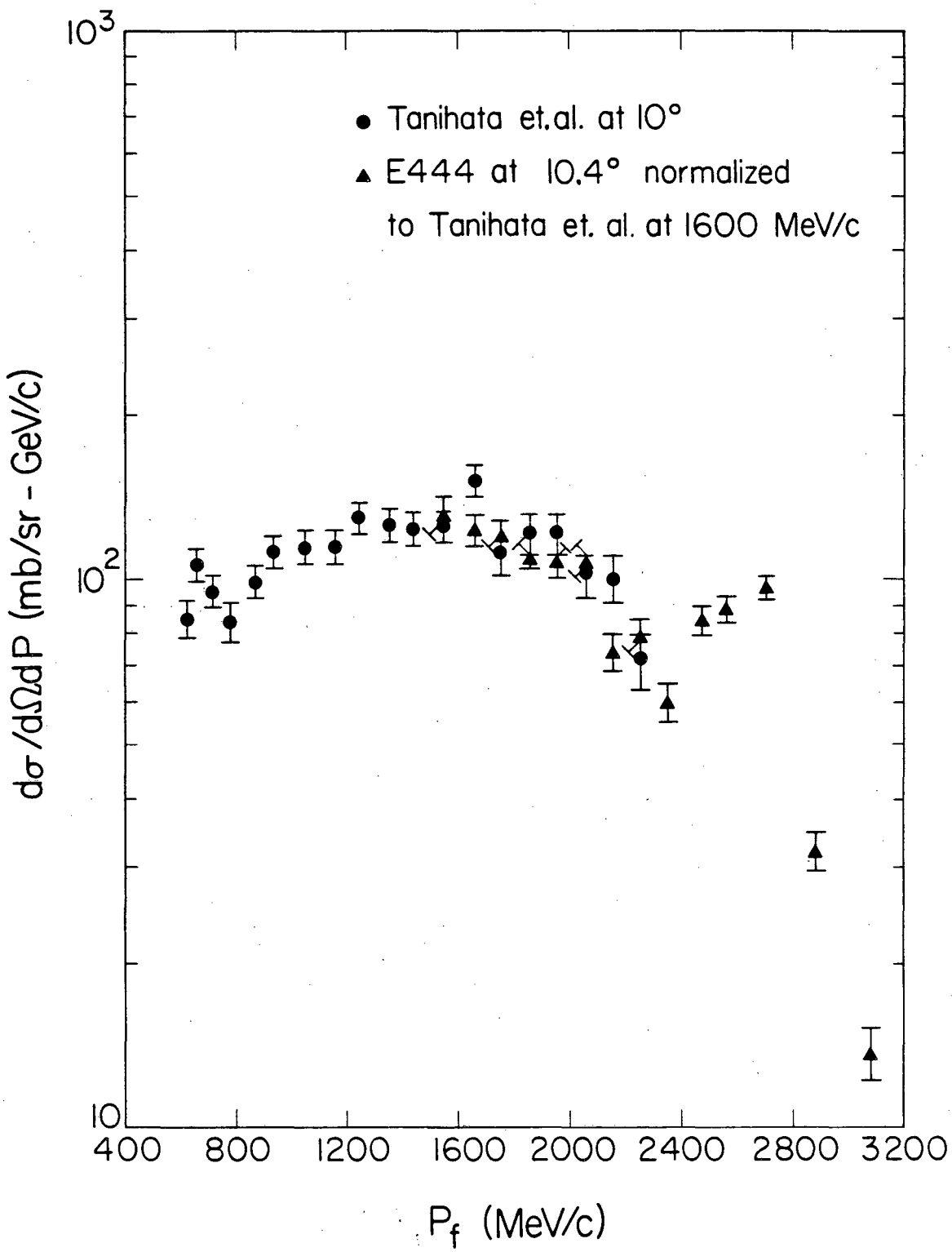

XBL 825-1358

Fig. 32

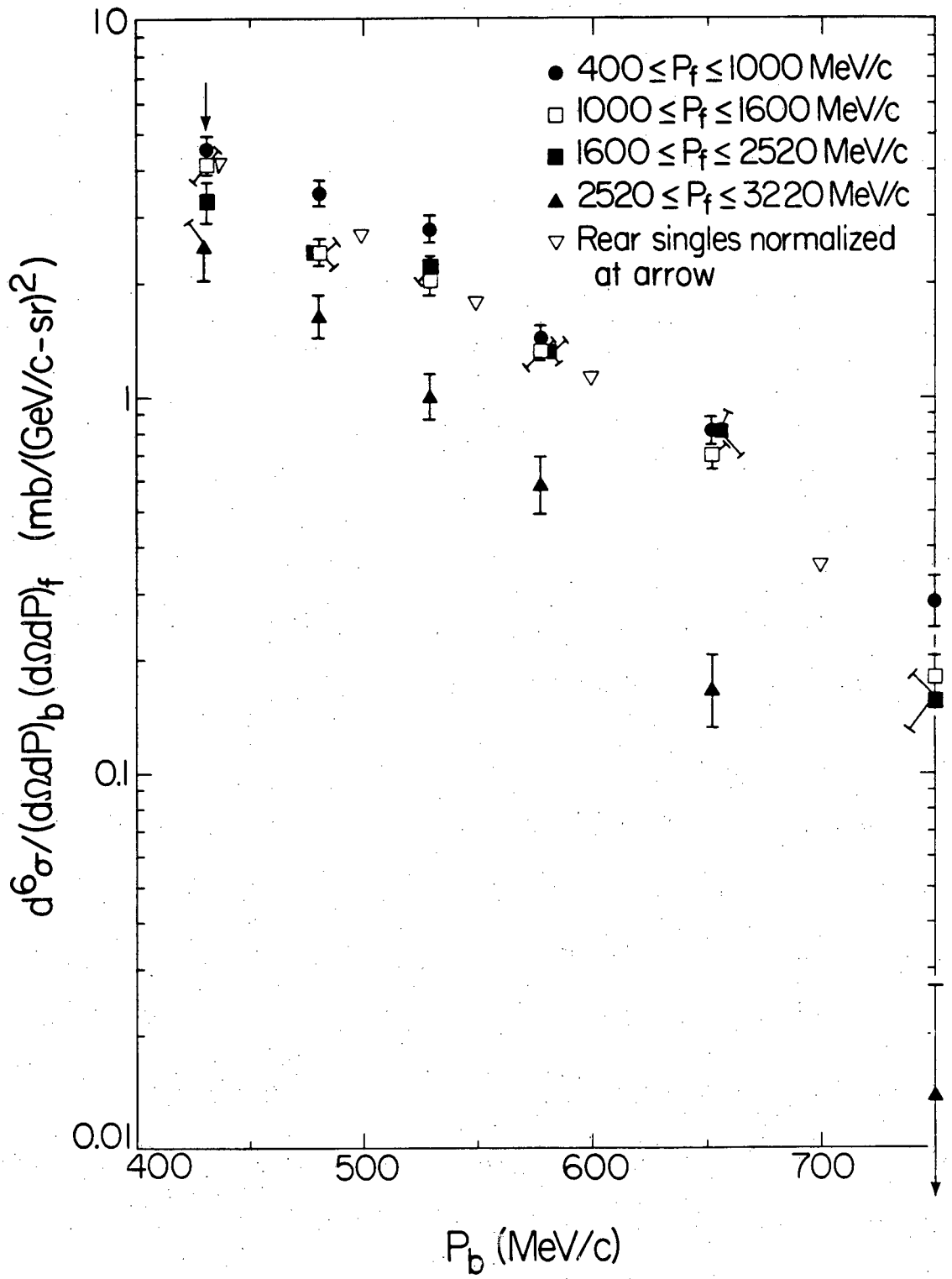

XBL 825-1357

Fig. 33

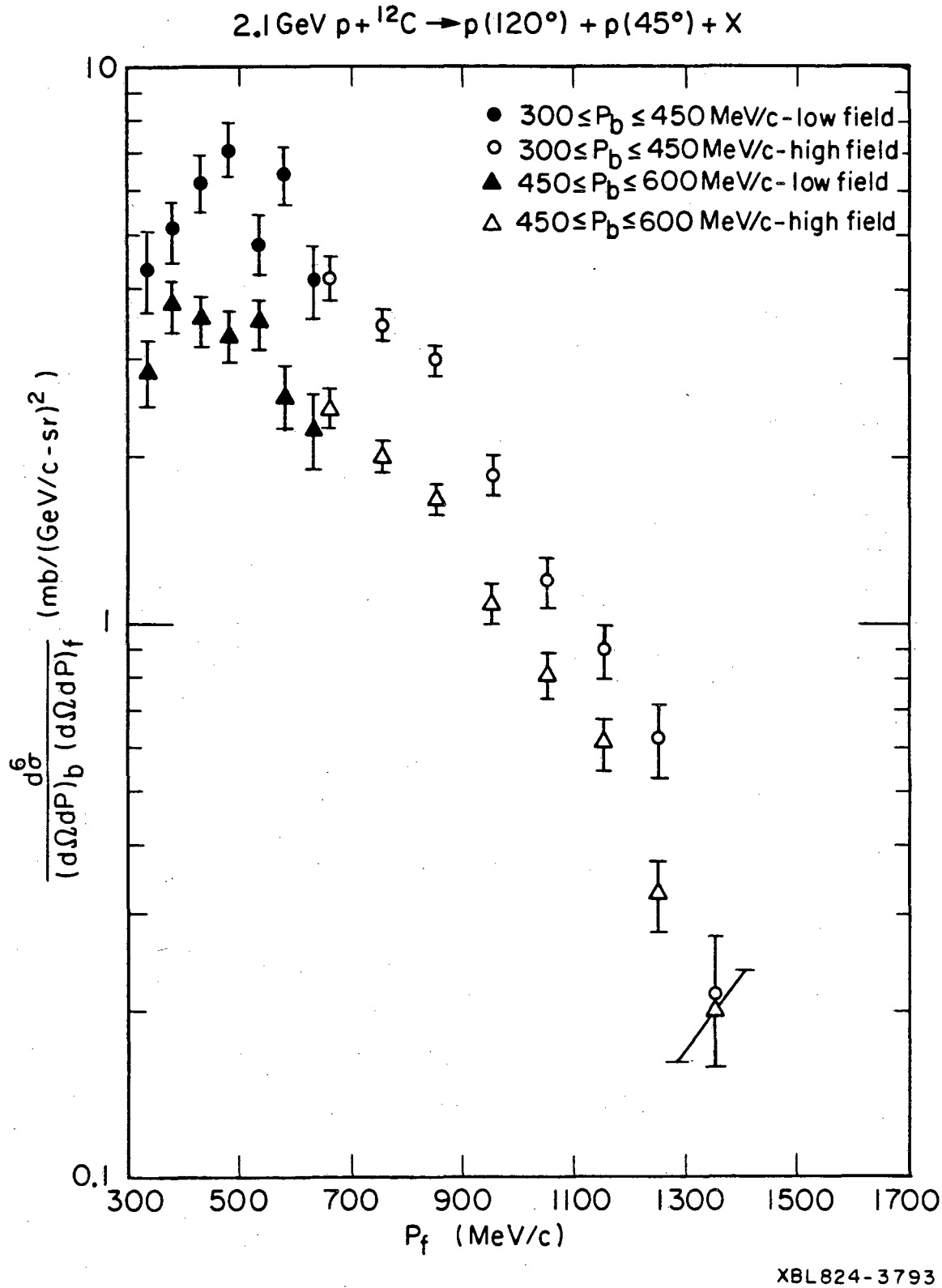
2.1 GeV p + ^{12}C → p(120°) + p(45°) + X
● 300 ≤ P_b ≤ 450 MeV/c - low field
○ 300 ≤ P_b ≤ 450 MeV/c - high field
▲ 450 ≤ P_b ≤ 600 MeV/c - low field
△ 450 ≤ P_b ≤ 600 MeV/c - high field
$\frac{d^6\sigma}{(d\Omega dP)_b\,(d\Omega dP)_f}$ (mb/(GeV/c-sr)^2)
10
1
0.1
300
500
700
900
1100
1300
1500
1700
P_f (MeV/c)
XBL824-3793

Fig. 34

2.1 GeV p + $^{12}C \rightarrow p(45^{o})$ + X

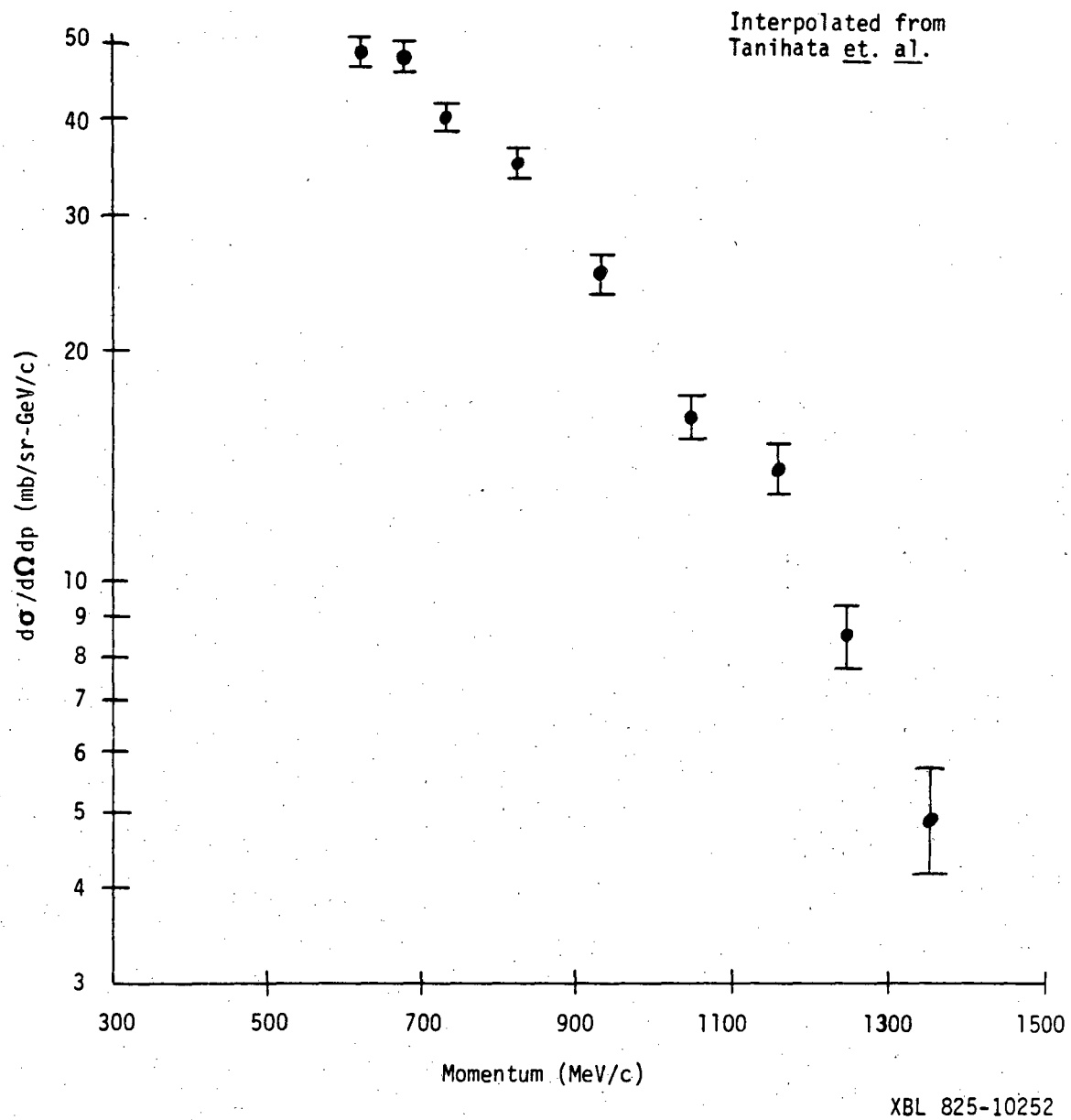

Fig. 35

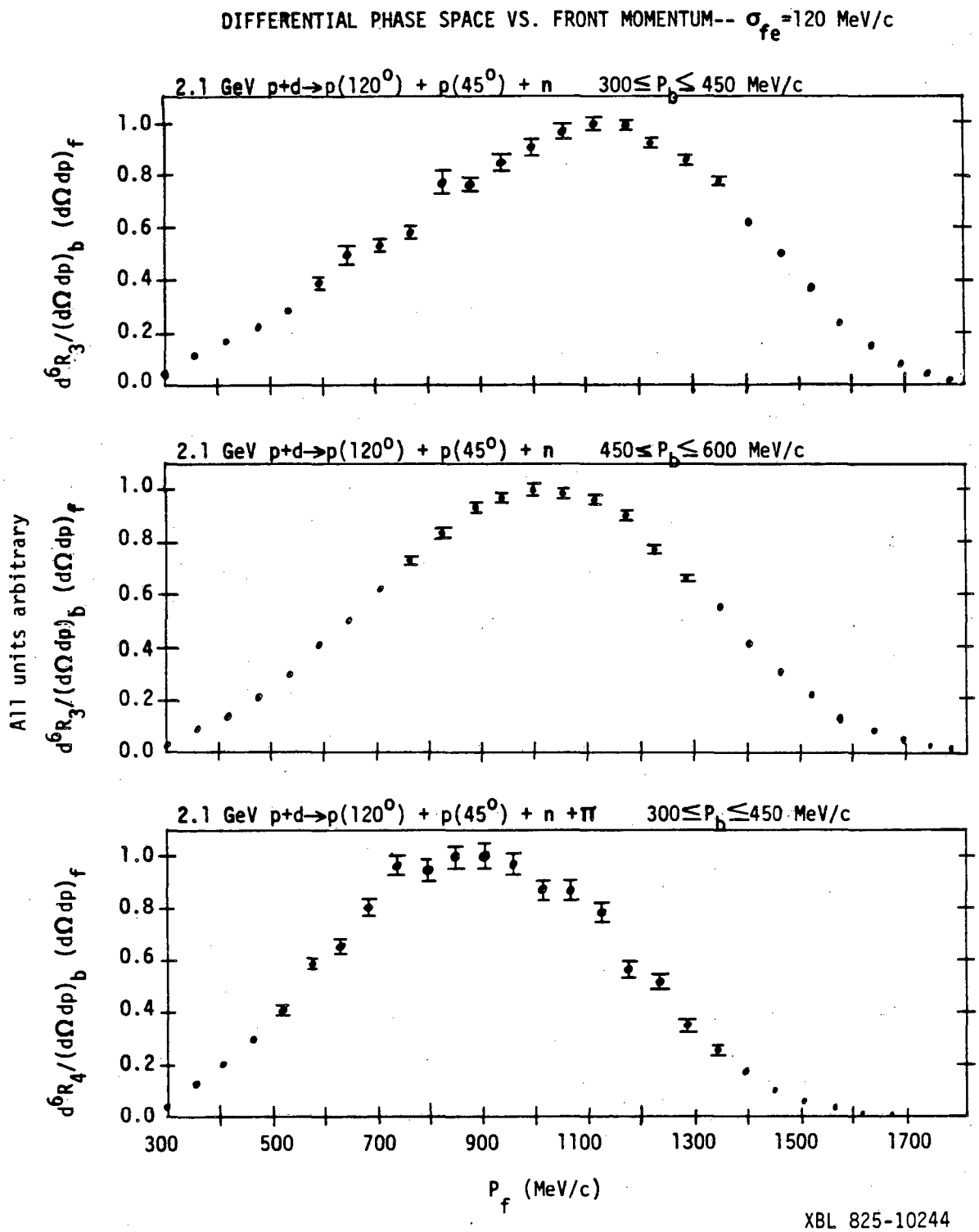
DIFFERENTIAL PHASE SPACE VS. FRONT MOMENTUM-- σ_{fe}=120 MeV/c
2.1 GeV p+d→p(120°) + p(45°) + n 300≤ P_b≤ 450 MeV/c
2.1 GeV p+d→p(120°) + p(45°) + n 450≤ P_b≤ 600 MeV/c
2.1 GeV p+d→p(120°) + p(45°) + n +π 300≤P_b≤450 MeV/c
All units arbitrary
$d^6R_3/(d\Omega\, dp)_b\ (d\Omega\, dp)_f$
$d^6R_4/(d\Omega\, dp)_b\ (d\Omega\, dp)_f$
0.0
0.2
0.4
0.6
0.8
1.0
300
500
700
900
1100
1300
1500
1700
P_f (MeV/c)
XBL 825-10244

Fig. 36a,b,c

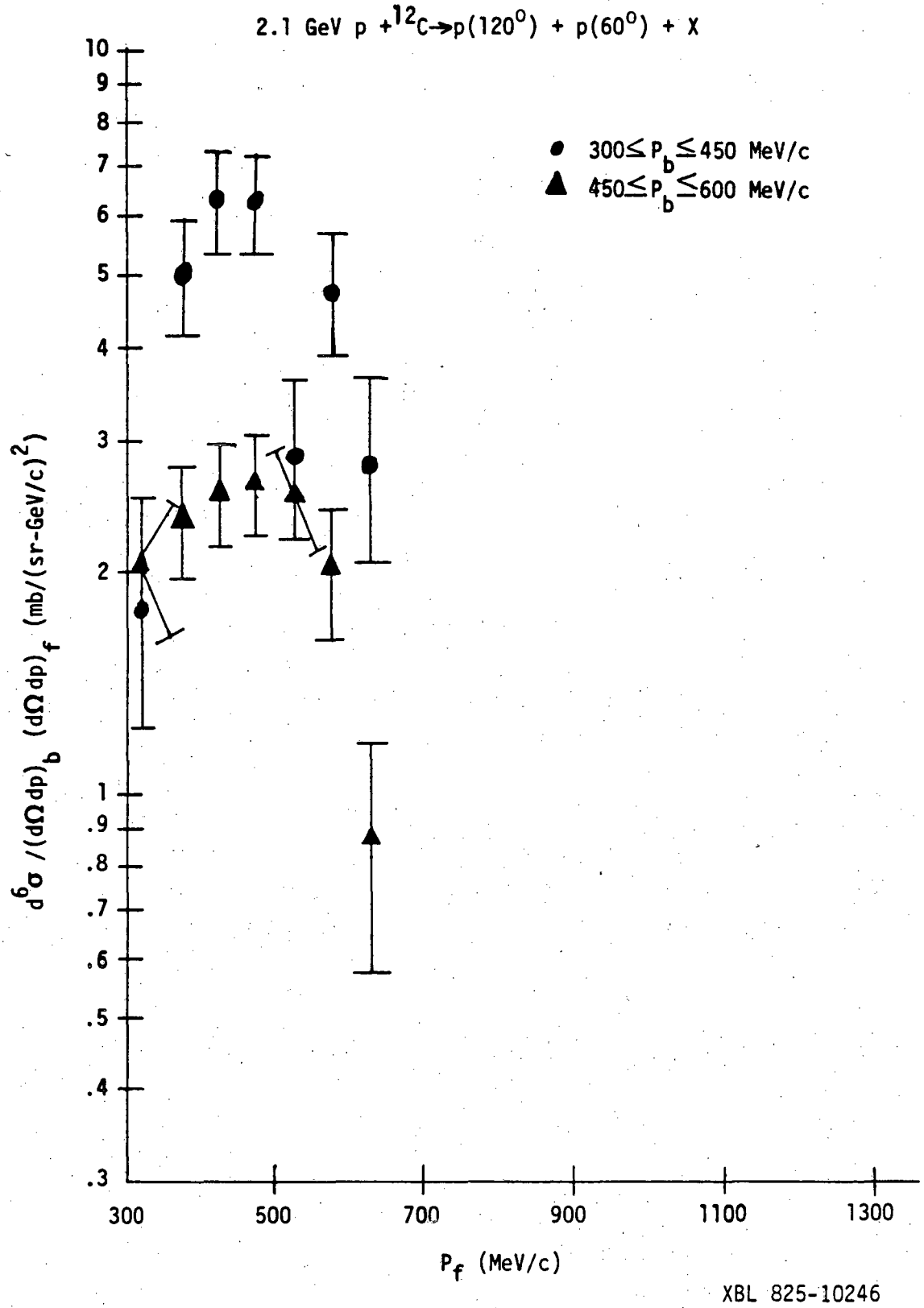
2.1 GeV p + ^{12}C → p(120°) + p(60°) + X
300 ≤ P_b ≤ 450 MeV/c
450 ≤ P_b ≤ 600 MeV/c
$d^6\sigma/(d\Omega dp)_b (d\Omega dp)_f$ (mb/(sr-GeV/c)^2)
10
9
8
7
6
5
4
3
2
1
.9
.8
.7
.6
.5
.4
.3
300
500
700
900
1100
1300
P_f (MeV/c)
XBL 825-10246

Fig. 37

TRANSMISSION FACTORS FOR PENCIL AND GAUSSIAN BEAM PROFILES

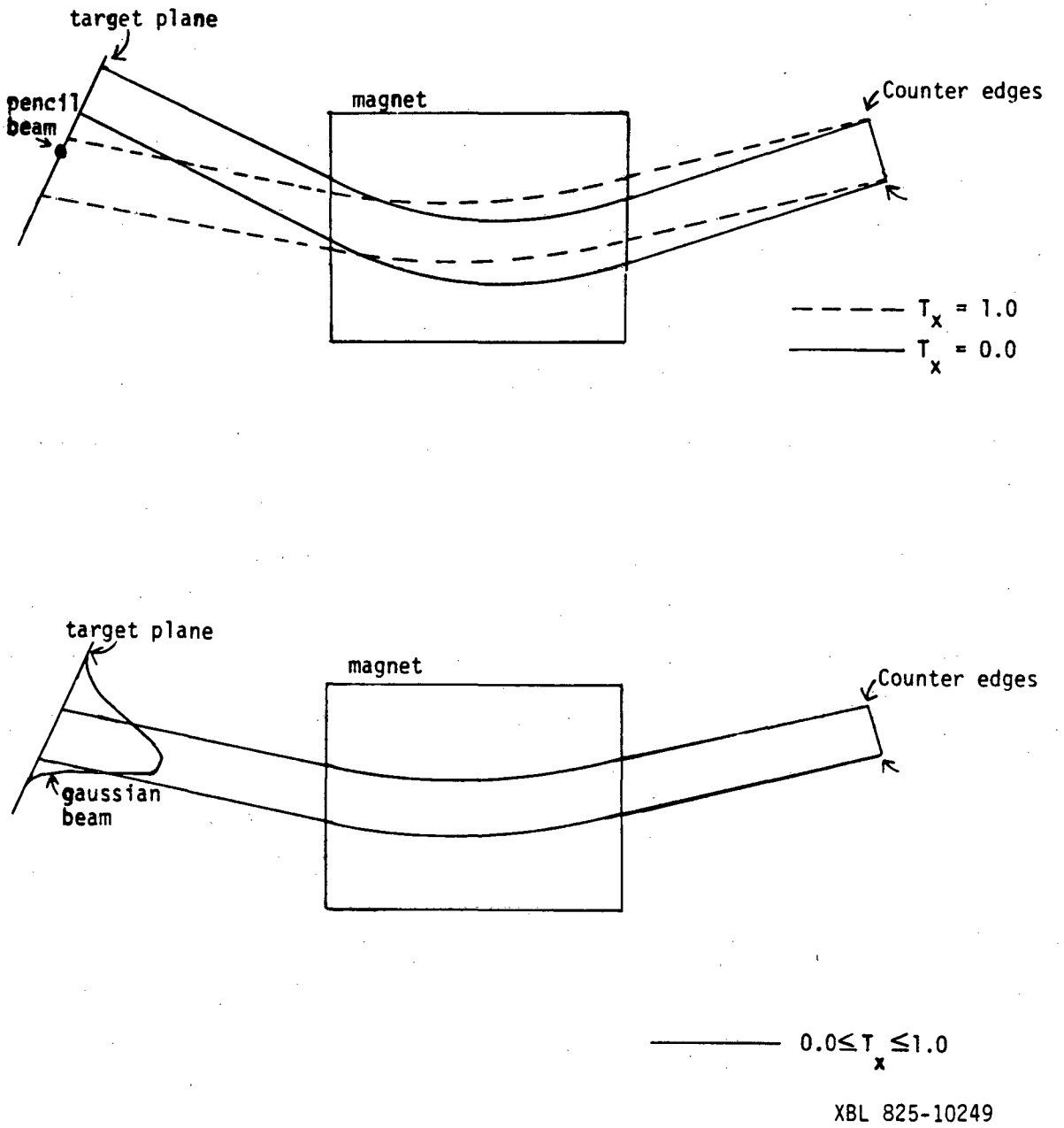

Fig. B1a,b

This report was done with support from the Department of Energy. Any conclusions or opinions expressed in this report represent solely those of the author(s) and not necessarily those of The Regents of the University of California, the Lawrence Berkeley Laboratory or the Department of Energy.

Reference to a company or product name does not imply approval or recommendation of the product by the University of California or the U.S. Department of Energy to the exclusion of others that may be suitable.

TECHNICAL INFORMATION DEPARTMENT
LAWRENCE BERKELEY LABORATORY
UNIVERSITY OF CALIFORNIA
BERKELEY, CALIFORNIA 94720